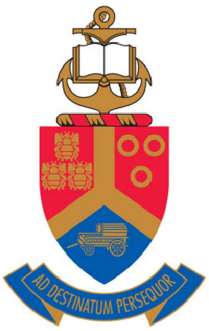

UNIVERSITEIT VAN PRETORIA
UNIVERSITY OF PRETORIA
YUNIBESITHI YA PRETORIA

Denkleiers • Leading Minds • Dikgopolo tša Dihlalefi

OPTICAL VORTEX DETECTION AND STRONGLY SCINTILLATED BEAM CORRECTION USING VORTEX DIPOLE ANNIHILATION

by

Mingzhou Chen

Submitted in partial fulfilment of the requirements for the degree

Philosophiae Doctor (Computer Engineering)

in the

Faculty of Engineering, Built Environment and Information Technology

UNIVERSITY OF PRETORIA

April 2008

Optical Vortex Detection and Strongly Scintillated Beam Correction Using Vortex Dipole Annihilation

by

Mingzhou Chen

Promotor: **Prof. Filippus S. Roux**

Co-promotor: **Prof. Jan C. Olivier**

Department: **Electrical, Electronic and Computer Engineering**

Faculty of Engineering, Built Environment and Information Technology

Degree: **PhD (Computer Engineering)**

Summary

This thesis focuses on two topics about optical vortices in strongly scintillated beams. One is optical vortex detection with a conventional Shack-Hartmann wavefront sensor. The other is the correction of strongly scintillated beams through forced vortex dipole annihilation.

Based on vortex detection with a line integral over the phase gradient around a vortex, circulation is implemented over the outputs of a Shack-Hartmann wavefront sensor to detect optical vortices. The output of the wavefront sensor is computed with an area integration to obtain an analytical expression for vortex circulation. The vortex locations and topological charges can be determined from the peaks of the circulation. In these investigations, it is shown that this circulation value for a vortex is not $\pm 2\pi$ as is obtained from a line integral, but a smaller value depending on the relative positions and its morphologies of the vortex in the wavefront sensor subaperture. Since the outputs of a Shack-Hartmann wavefront sensor computed with area integrations approximate the outputs computed from the bright spots centroid shifts in a real Shack-Hartmann wavefront sensor, the vortex circulation values may be much closer to the results of physical experiments. At the same time, the influence of the morphology as the vortex is detected with a Shack-Hartmann wavefront sensor is also investigated.

In a strongly scintillated beam, there are generally numerous optical vortices. They are in general created and annihilated as vortex dipoles. Due to the cancellation effects in the circulations, the influence of a vortex dipole on the Shack-Hartmann vortex detection is also investigated in this thesis. Investigations are carried out in a Gaussian beam for simplicity. Although the morphology of a vortex changes when the vortex is close to the annihilation point, it is shown that the vortex morphology evolution during beam propagation does not have a significant impact on Shack-Hartmann vortex detection. When two oppositely charged vortices approach each other, the vortex circulation peaks may cancel each other out. This cancellation effect is especially strong when the separation distance in a vortex dipole is smaller than twice the size of the Shack-Hartmann wavefront sensor subaperture. Therefore a small separation distance makes Shack-Hartmann vortex detection more difficult. Statistical results obtained from numerical simulations for Shack-Hartmann vortex detection in strongly scintillated beams show good agreement with the investigations in a Gaussian beam.

For the correction of strongly scintillated beams, the continuous phase fluctuations can be corrected with a conventional adaptive optics (AO) system by removing the least-squares reconstructed phase. This leaves behind the solenoidal phase distortions caused by optical vortices. The only way to correct the strongly scintillated beams with numerous optical vortices is to get rid of these optical vortices by forcing them to annihilate in oppositely charged pairs. Since vortices are annihilated in pairs, the global background phase prior to dipole annihilation is investigated. This background phase shows the potential of forcing a vortex dipole to annihilate. However, the extraction of this background phase before dipole annihilation may introduce errors due to the finite resolutions. Therefore, the background phase after dipole annihilation is taken into consideration. Since the phase changes gradually during beam propagation, the background phase after dipole annihilation is assumed to retain the power of forcing a vortex dipole to annihilate. Therefore, a background phase can be created based on the locations of any vortex dipole, and in turn use it to remove vortex dipoles. Numerical simulations show that the background phase after dipole annihilation can efficiently accelerate the annihilation of a vortex dipole. Even if two oppositely charged vortices will move apart from each other and never annihilate each other during beam propagation, this background phase can force them to annihilate.

Based on the concept of accelerating the annihilation of a vortex dipole through continuous background phase modulation, a beam correction system is proposed. It consists of a few conventional AO systems using dipole annihilation and least-squares (DALS) phase correction. The least-squares phase correction scheme is also used to remove the

continuous phase fluctuations. We find that the removal of the least-squares reconstructed phase in a strongly scintillated beam may cause some vortex dipoles with short separation distance to annihilate by themselves after a short distance of free-space propagation. However, it does not have an impact on the dipoles with large separation distances. An algorithm is proposed to identify the vortex dipoles according to the vortex locations. A background phase is created based on these dipoles, and is in turn used to force these dipoles to annihilate. In the beam correction system, the least-squares reconstructed phase together with this background phase is used to get rid of optical vortices and remove the continuous phase fluctuations in a strongly scintillated beam. Numerical simulations show that the number of optical vortices are reduced significantly after a few steps of DALS phase corrections. Several statistical results and curves are obtained and compared with least-squares phase correction, which indicate that the system's performance is improved significantly.

Keywords: Adaptive optics (AO), atmospheric turbulence, scintillation, Gaussian beam, beam propagation, Shack-Hartmann wavefront sensor, optical vortex, dipole annihilation, phase conjugation, background phase, deformable mirror.

For my beloved wife and daughter

Acknowledgement

Studying abroad is in itself a challenge. The opportunity to develop research skills and at the same time to get immersed in a completely different culture is fascinating. This opportunity was enhanced by doing research at the University of Pretoria (UP) in South Africa. The people and the atmosphere here made my study bearable and sometimes even enjoyable.

First and foremost, I would like to express my deep gratitude to my supervisor, Prof. Filippus S. Roux, for suggesting this PhD topic in the first place, and for his invaluable support and help throughout the three years of the study. He taught me a great deal, from enhancing my English writing skills to thinking over the results of experiments, and a lot of things in between. His ideas and points of view have been a constant source of inspiration to me. I have benefitted from my weekly meeting with him. Some of the ideas developed in this work are the results of our long discussions. I'm also grateful to my co-supervisor, Prof. Jan C. Olivier, for his patience, encouragement, guidance and last but not least, financial support. This work would also not have been possible without a UP postgraduate bursary.

My grateful acknowledgments go to the UP department of Electrical, Electronic and Computer Engineering (EEC). I always experienced the support of this department in all my endeavors. The department's assistance, financial and computing resources gave me welcome security and peace of mind to concentrate on my study. I would like to thank all the staff at the department of EEC who had to put up with me all these years: Hannetjie van Aswegen, Heleen Gous, Cornel Freislich, Maryna Bekker, Mari Ferreira, and especially Hans Grobler, who helped me a lot in using the departmental computing resources in my simulations. Thanks to all of them.

Many other friends contributed to making my life as a PhD student a memorable time: Xiyin Liang, Donghui Wei, Yin Li, Guojun Ma, Xiangtao Zhuan, Dongdong Jiang and many others gave me the opportunity to enjoy life here during these years. I am also very

grateful to Barbara Bradley for proofreading this thesis.

Most importantly, I'd like to thank my parents for their constant support and confidence in my decisions. Where would I be without them?

Final words of thanks go to my beloved wife, Nan, for her invaluable constant support, love and tenderness in most of these three years, and my daughter, Zimeng. I can now acknowledge that this thesis would never have been finished without them.

Contents

Chapter 1

Introduction

1.1 Literature review and motivations

Our earth is completely covered by a thick layer of atmosphere, which provides plants with rain and us with oxygen to breathe. This layer of atmosphere is warmed by sunlight during the daytime and gradually cools down during the night, which causes large scale motions in the air. These eventually become turbulent and result in inhomogeneous thermal gradients, humidity fluctuations and wind shear. As a result, the atmosphere exhibits an inhomogeneous index of refraction. This would warp the wavefront of any beam propagating through it. After an optical wave propagates through the turbulent atmosphere, it will form a speckled image in an imaging system, even if the optical system is intrinsically perfect and without any aberration [1]. Such image defects are known to originate from atmospheric turbulence [2].

To improve the imaging performance of an airborne optical system, Babcock [3] put forth atmospheric turbulence compensation by mechanical means, which is at present referred to as adaptive optics (AO) [4]. The conventional AO system has been widely used in astronomical applications. It can improve the image qualities of ground-based telescopes in astronomical applications when atmospheric turbulence is weak. Recently, an AO system is also used to investigate the aberration dynamics of the human eye by measuring the deviations of the retinal spot [5, 6].

In a laser projection system [7], such as a laser communication system or a laser weapon system, the laser beam needs to propagate over a long horizontal distance through the atmosphere near the ground, where atmospheric turbulence is very strong. The phase

aberrations in one region may be converted into amplitude fluctuations, which are referred to as scintillation, and then both phase and amplitude will corrupt the wavefront in the system aperture [8]. The energy density or the signal-to-noise ratio of these systems will be reduced a great deal owing to the turbulence-induced scintillation. An AO system is an approach to improve the performance of such an optical system by partially compensating for turbulent effects [9-13]. However, in these practical applications, optical vortices can appear spontaneously after a beam has propagated in a strong turbulent atmosphere over a long distance. The development of optical vortices in the propagation of a distorted wave function was analytically discussed by Fried *et al.* [14]. In the system receiver aperture, the optical wave becomes a speckle field due to the presence of optical vortices, which can severely degrade the system's performance. By measuring and reconstructing the wavefront in the receiver aperture, an AO system can use phase conjugation in an attempt to remove the scintillation to improve the system's performance [4]. However, the presence of a large number of optical vortices in the receiver aperture is detrimental to the applied problem in this kind of AO system, because a field with optical vortices cannot be conjugated by means of a deformable mirror [15]. Wavefront distortion correction will be in error in the vicinity of an optical vortex core. Hence, the appearance of optical vortices can significantly affect the effectiveness of phase conjugation in a conventional AO system [16]. At the same time, only the phase information is used in the scintillated beam correction with a conventional AO system. The fidelity of the phase conjugation is reduced due to the loss of the amplitude information. The connection between the amplitude fluctuations and the limits of phase-only correction was investigated with different statistical models [17]. Experiments were carried out to show a significant performance degradation in wavefront correction with a conventional AO system that employed a continuous surface deformable mirror and a Shack-Hartmann wavefront sensor when scintillation is increased [18].

The Shack-Hartmann wavefront sensor is one kind of widely used wavefront sensor. It measures the shape of an optical wavefront that was distorted after propagating through a turbulent atmosphere. Although there are measurement errors in the Shack-Hartmann wavefront sensor in practical implementation, the reasonable simplicity makes it ideal for use in an AO system, which is to correct the wavefront distortions in such a scintillated beam. Various techniques [19–24] are used to compute the shape of the wavefront from the raw data received as output from a Shack-Hartmann wavefront sensor. However, in strongly scintillated beams these techniques tend to fail [25] due to the presence of optical vortices in the propagating scintillated beam. The failure of these techniques is to some extent a result of the apparent insensitivity of the Shack-Hartmann wavefront sensor to the phase function of an optical vortex. The solenoidal part of the phase distortions

as a contribution of optical vortices in a scintillated beam is then referred to as hidden phase [26]. Initial least-squares phase reconstruction methods [19–22] that were used in AO systems were based on a model for the phase slopes that makes the assumption that the phase function is continuous. The existence of optical vortices violates this assumption. Therefore, these methods can only be applied where the phase distortions are not large enough to generate optical vortices.

Various authors [27–30] considered the separation of the phase gradient function into a continuous (curl-free) part and a solenoidal or rotational part. The former can be used in the conventional AO system to correct the continuous part of the phase distortions. The latter is generally treated as a noise term, which is discarded. Since it represents the contribution of the optical vortices, the solenoidal part of the phase distortions cannot be removed in the same way that the continuous part of the phase distortions is removed. Neither does it simply go away after the continuous part has been corrected [26, 31].

Fried has developed an algorithm for phase reconstruction from wavefront sensor data when optical vortices are present [32]. The reconstructed phase contains the part of the distorted wavefront associated with the optical vortices, as well as the continuous phase part that can be captured by an ordinary least-squares phase reconstructor. Similarly, Roggemann *et al.* implemented a so-called branch-point reconstructor, i.e. Goldstein's algorithm [33], to reconstruct the vortex-bearing wavefront [34]. It was found that this branch-point reconstructor significantly improves the performance over least-squares reconstructors on a laser beam projection, especially when scintillation is moderate to strong. However, in the first step of this reconstructor, he assumed that wave-front sensor can ideally measure the phase differences. Optical vortices in the scintillated beams are detected by a closed line integral over these phase differences, which is a significant impediment in practice owing to the sampling and noise in real wavefront sensors. Without the need to find the locations of optical vortices specifically, another algorithm was developed by Roggemann, which directly estimates the optimal set of weights for wavefront reconstruction basis function by jointly processing the entire wavefront sensor image, a pupil intensity image and a conventional image [35].

Compared with the conventional AO system using phase conjugation without considering amplitude information, optical field conjugation which corrects both amplitude fluctuations and phase distortions for scintillated beams seems to be more efficient to improve the performance of an optical system [36]. A two-deformable-mirror concept for correcting strong scintillation effects were proposed by Roggemann *et al.* [37]. In this system, one deformable mirror is used to adjust the amplitude of the wave in the pupil

while a second deformable mirror is used to correct the phase of the outgoing wave. Subsequently, Barchers *et al.* developed the parallel generalized projection algorithm (PGPA) to improve this two-deformable-mirror correction approach, by introducing constraints to minimize the number of optical vortices in the control signals for the deformable mirrors [38]. Unfortunately, a typical deformable mirror with a continuous surface cannot realize the phase profile of an optical vortex . Therefore, the presence of optical vortices is still an impediment in the performance of this kind of AO.

Optical vortices are ubiquitous in nature. They had already attracted a great deal of interest in the literature before Fried pointed out the problems caused by optical vortices in AO systems [26]. In the landmark 1974 paper of Nye and Berry [39], it was shown that there are imperfections in the wave trains, which were first known as wavefront screw dislocations. In laser physics, these screw dislocations are referred to as optical vortices because of their vortex-like phase profile [40]. Two different parameterizations were proposed to depict the structure surrounding an optical vortex (noncanonical vortex) [41, 42]. Berry has theoretically investigated the distribution, i.e. the density and the fluxes, of optical vortices in Gaussian random wave fields [43]. Early experiments and numerical simulations of optical vortices in random wave fields were done by Baranova *et al.* [44] and Freund *et al.* [45]. Subsequently, Berry and Dennis provided theoretical analysis on the statistical characteristics of optical vortices in isotropic random waves in more detail [46]. These statistical local structure properties of optical vortices in random wave fields were verified by the first direct experiment conducted by Wang *et al.* [47]. Voitsekhovich derived an empirical optical vortices density formula in various conditions of turbulence, ranging from weak ones to very strong ones [48]. The densities of phase critical points (dislocations, extrema and saddles) in planar isotropic random waves were calculated analytically by Dennis [49]. It was pointed out by Roux that the net topological charge densities of optical vortices in an area cannot exceed the circumference of that area divided by the wavelength [50].

At the same time, Freund and Shvartsman investigated the topology of random Gaussian distributions of optical vortices and found extensive anticorrelations between numerous near-neighbor vortex parameters [45, 41]. Four simple topological rules were derived in a random Gaussian wave field [51]. Freund also proved the sign principle, which states that there is a high probability of the nearest neighboring optical vortices having opposite topological charges [52]. It was proven earlier by Zel'dovich that an optical vortex with a high-order topological charge is not stable in a speckle field [53]. A single high-order charged optical vortex can decay explosively into a large number of generic single-charged vortices under the influence of small perturbations [54]. Therefore, only single-charged

optical vortices are stable and can survive in random optical fields, including scintillated beams.

Optical vortices can be generated in some controlled ways, by reflecting a plane wave from a spiral phase step [55, 56], by three plane wave interferences [57] or by using computer-generated holograms [58, 59]. In a beam propagating in an inhomogeneous medium, optical vortices are randomly created and annihilated in pairs [60]. Experiments have been done by Heckenberg to study the creation and annihilation of the optical vortex pairs [61].

In the singular beams created by computer-generated hologram or by mode converter, optical vortices can be detected by interference with a coherent reference beam, split beam technique, a mode converter or optical Fourier transform recognition [62]. By using interferometry, Baranova *et al.* have experimentally identified the optical vortices for their charges in random laser speckle fields [44]. However, the positions of the vortices were not well determined.

At the time of writing this thesis, it is still very difficult to detect optical vortices in strongly scintillated beams with a Shack-Hartmann wavefront sensor. The detection of optical vortices is significantly influenced by the averaging effect of the Shack-Hartmann wavefront sensor subapertures. This averaging effect has not received much attention to date. Herrmann mentioned a model error due to the averaging phase gradients, but did not give a detailed analysis [63]. Aksenov calculated the average wavefront slopes with a regularization procedure that produces continuous infinitely differentiable functions, which is not true when there are optical vortices in the phase function [29]. Bigot *et al.* provided a theory of vortex detection from wavefront sensor measurements with a so-called branch point potential [64]; however, it is only suitable for vortex visualization.

In recent years, the dynamical behavior of optical vortices in linear and nonlinear medium have received a great deal of attention in the literature. Indebetouw analytically investigated the free-space propagation of a pair of optical vortices nested in a Gaussian beam [65]. He found that optical vortices with the same topological charges simply expand or contract with the host beam and rotate rigidly during beam propagation. In contrast, optical vortices with opposite charges move towards each other and annihilate in pairs. The behavior of a same-charged vortex pair has been experimentally observed in free-space beam propagation [66, 67]. Mamaev's investigation about a pair of oppositely charged optical vortices in anisotropic nonlinear medium shows that a symmetric attractive potential is created by incoherent coupling between these two vortices [68]. Subsequently, Roux found that a canonically launched vortex dipole has the possibility

of annihilations and revivals under different conditions in a Gaussian beam [69].

Optical vortices in a beam display complicated dynamical behavior, which includes moving towards each other, rotating around each other, or annihilating each other on the transverse beam plane, perpendicular to the propagation direction. Vortex trajectories are three-dimensional lines defined in an appropriate space, which represent the vortex dynamical behavior during beam propagation [70]. In a three-dimensional space, these vortex lines are closed loops. The tangent points between these closed loops and the transverse beam plane represent the points where two oppositely charged vortices are created or annihilated [71]. Some specific rules for the optical vortex trajectories were suggested by Freund [72]. He also provided the concept of a critical points bundle, which is formed by the trajectories of vortices, phase extrema and saddles. These bundle geometries show that there are only two scenarios for the creation or annihilation of a vortex dipole [73]. One scenario is that the vortex dipole is created or annihilated together with a pair of saddle points. The other one is that a pair of phase maximum and minimum collide and annihilate each other to create a vortex dipole, or in a reverse process. During the vortex propagation, it was also found that the vortex morphology does not remain unchanged [74–76] .

A "vortex as a particle" model has been proposed by Staliunas to interpret qualitatively the motion of one vortex on the transverse beam plane in the laser beam [77]. In this model, it is shown that the vortex starts to move if the spatial symmetry of the background field in the vicinity of the vortex core is broken when the background field is perturbed by amplitude and phase. The laws of optical vortex motion have correspondences in hydrodynamical vortex theory, i.e. the optical vortex moves in the direction of the phase gradient of the background field, and transverses to the amplitude gradient of the background field. However, Staliunas has not developed a more precise model of two vortices' mutual interaction. Roux proposed a preliminary model to interpret the motion of two vortices based on the assumption of a single vortex moving in the direction of the phase gradient of the background field [78]. The amplitude of background field is supposed to be uniform in his model. This model is successful in interpreting the rotation of a vortex pair with the same charges and the lateral drift of a vortex pair with opposite charges. However, it seems that this model is not able to interpret the reason for the annihilation of two oppositely charged vortices. Subsequently, based on the "vortex as a particle" model, Rozas *et al.* investigated the dynamical behavior of optical vortices in Gaussian beams and nonlinear medium analytically and experimentally [79, 80]. The linear motions of one vortex and the rotational movements of two same-charged vortices were observed. Schwarz *et al.* investigated the evolution of an off-axis optical vortex in a

J_0 Bessel beam [81]. Subsequently, Flossmann *et al.* investigated the propagation dynamics of optical vortices in a Laguerre-Gaussian beam [82,83]. They found that new vortices are created in pairs during the propagation of the beam with an initial off-axis vortex. The motion of the vortices can also be explained by the gradient of the background beam.

These two main causes, the phase gradient and the amplitude gradient of the background field, are external spatial parameters, which influence the motion of an optical vortex. Some other studies have tried to control the vortex motion by adjusting the vortex intrinsic or extrinsic parameters. Molina-Terriza *et al.* proposed a method of controlling the trajectory of a single vortex by adjusting the anisotropy of an input optical vortex [84]. Similarly, Kim *et al.* investigated the control of the rotational rate of a same-charged vortex pair in the linear and nonlinear medium [85]. The results show the rotation rate of optical vortices is proportional to the vortex anisotropy. By properly choosing the topological charge, the separation distance between optical vortices, Neshev *et al.* proposed a possible way to control the motion of the optical vortices nested in a background beam [86].

1.2 Goals and objectives

From the above, it seems to be difficult to correct the strongly scintillated beams by a traditional AO system. In this thesis, an appropriate optical system will be implemented for strong scintillations, using traditional AO systems. This system can correct the beam by effectively removing optical vortices and phase distortions from the wavefront. The corrected beam has a planar phase profile. Therefore, it can form an image with high qualities on the imaging sensor.

To obtain this goal, optical vortices in the strongly scintillated beam need to be detected for their locations and topological charges. Due to its simplicity, a Shack-Hartmann wavefront sensor, which is widely used in AO systems, is proposed for the detection of optical vortices. After the locations of vortices are obtained, these vortices need to be forced to annihilate in pairs. Thus, the solenoidal phase part can be converted into continuous phase parts which can be easily removed by a traditional AO system.

1.3 Contributions

This thesis covers two main topics: (1) Optical vortex detection with a Shack-Hartmann wavefront sensor and (2) strongly scintillated beam correction through forced vortex dipole annihilation.

In this thesis, optical vortex detection is achieved with a common optical device, a Shack-Hartmann wavefront sensor. The effect of the averaging process on an optical vortex is analytically investigated, by performing the actual integration of the phase gradient function of such an optical vortex over the area of a subaperture. The output of a Shack-Hartmann wavefront sensor is in the form of a sampled vector field that approximately represents the phase gradient function of the scintillated beam. A curl operation, which is referred to as circulation here, is carried out on this sampled vector field in terms of finite differences. It is found that the Shack-Hartmann wavefront sensor is not completely insensitive to an optical vortex. When an optical vortex is present in the wave field, the circulation of the output of the Shack-Hartmann wavefront sensor gives a peak value. This peak value is smaller than $\pm 2\pi$ as is obtained from a line integral over the phase gradient [26]. The effect of the morphology and relative position of the optical vortex on this detection process is also investigated. Based on single vortex detection, the influence of two oppositely charged vortices, a vortex dipole, on the vortex detection with a Shack-Hartmann wavefront sensor is investigated. It is found that the circulation peak of a vortex drops rapidly when another oppositely charged vortex approaches it. However, the vortex morphology does not influence the Shack-Hartmann vortex detection significantly in a vortex dipole.

Another contribution of the author is to propose a new strong scintillation correction scheme with conventional AO systems. In this beam correction scheme, a background phase function and a least-squares reconstructed phase function are used in each AO system to force the vortex dipoles to annihilate with a short distance of free-space beam propagation. From the dynamical behavior of a vortex dipole in the propagating beam, the background phase function before a dipole annihilation seems to have the potential to accelerate dipole annihilation. Due to the gradual changes in the phase functions along the direction of beam propagation, the background phase function before a dipole annihilation can be approximated by the background phase function after dipole annihilation. Therefore, it can be assumed that the latter background phase function retains the power of forcing a vortex dipole to annihilate. It is also a continuous phase function that can in principle be approximated by deformable mirrors. A procedure is proposed to create such a background phase function that can force a vortex dipole to annihilate after a

short distance of free-space propagation. At the same time, it is also found that the least-squares reconstructed phase not only removes the continuous phase fluctuations in a distorted beam, but also changes the dynamical behavior of optical vortices embedded in the beam. After the removal of the least-squares reconstructed continuous phase, some vortex dipoles with short separation distances begin to annihilate after a short distance of free-space propagation. Therefore, both the least-squares phase function and the background phase function created according to vortex dipoles are used to correct the strongly scintillated beams. After a few steps of beam corrections, most of the optical vortices disappear as a result of annihilating each other. Then, it is found that the phase of the corrected beam becomes smooth and flat and can therefore form a high quality image on the imaging sensor, which means that the optical system's performance is improved significantly.

Parts of this thesis have been published in or submitted to the following journals or conferences:

[1] Mingzhou Chen, Filippus S. Roux, and Jan C. Olivier, "Detection of phase singularities with a Shack-Hartmann wavefront sensor," *Journal of the Optical Society of America A: Optics, Image Science, and Vision*, vol. 24, no. 7, pp. 1994–2002, July 2007.

[2] Mingzhou Chen, Filippus S. Roux, "Dipole influence on Shack-Hartmann vortex detection in scintillated beams," *Journal of the Optical Society of America A: Optics, Image Science, and Vision*, vol. 25, no. 5, pp. 1084–1090, May 2008.

[3] Mingzhou Chen and Filippus S. Roux, "Accelerating the annihilation of an optical vortex dipole in a Gaussian beam," *Journal of the Optical Society of America A: Optics, Image Science, and Vision*, vol. 25, no. 6, pp. 1279–1286, June 2008.

[4] Mingzhou Chen and Filippus S. Roux, "Strongly scintillated beam correction through forced dipole annihilation," *Optics Express*, 2008. (submitted).

[5] Mingzhou Chen and Filippus S. Roux, "Removal of optical vortices from strongly scintillated beams," in 4^{th} *International Conference Singular Optics (Optical Vortices): Fundamentals and Applications (SO"2008)*, 15–20 September 2008, Alushta, Ukraine. (accepted)

1.4 Outline of thesis

The chapters in this thesis are organized as follows: Beam propagation in the atmosphere, beam correction by an AO system and optical vortex with its properties are described in Chapter 2. In Chapter 3 the detection of an optical vortex by a Shack-Hartmann wavefront sensor is discussed. The influence of a vortex dipole on Shack-Hartmann vortex detection is discussed in Chapter 4. After investigating the background phase behind a vortex dipole annihilation, this background phase is applied to accelerate the other dipole in a Gaussian beam to annihilate in Chapter 5. New algorithms are proposed in Chapter 6 to remove the optical vortices in strongly scintillated beams so as to use conventional AO systems to correct the phase distortions more efficiently. Finally, a summary of this thesis is presented and some suggestions for further study are provided in Chapter 7. In Appendix A, an algorithm is provided to separate the continuous phase slopes and the rotational phase slopes. Statistical properties of vortex morphologies in random wave fields are deduced in Appendix B. The morphologies of a canonically launched vortex dipole in a Gaussian beam and the statistical results of the morphologies of vortex dipoles in scintillated beams are provided in Appendix C.

Chapter 2

Beam propagation, beam correction and optical vortices

2.1 Introduction

In this chapter, the background knowledge that will be used in this thesis will be reviewed. A layered model for beam propagation through a turbulent atmosphere is described in Section 2.2. Random phase screen techniques are frequently used in numerical simulations of turbulent atmosphere. Several parameters are introduced to quantify the turbulent strength. In Section 2.3, the correction scheme of an AO system is introduced. The principles of two main components in an AO system, the Shack-Hartmann wavefront sensor and the deformable mirror, are introduced in Subsection 2.3.2 and 2.3.3 respectively. Then the procedure of reconstructing the continuous phase with a least-squares method from the wavefront measurements is introduced in Subsection 2.3.4. The phase and intensity profiles of an optical vortex are presented in Subsection 2.4.1. The trajectories and morphologies of optical vortices in a Gaussian beam are also described in Subsection 2.4.2. The phase function of a scintillated beam represented by the sum of the continuous phase function and the solenoidal phase function of optical vortices is defined in Subsection 2.4.3.

2.2 Beam propagation in a turbulent atmosphere

Beam propagation through a continuous random medium is the limiting case of propagation through a discrete series of random phase screens separated by a free-space distance. To approximate the continuous medium, the phase fluctuations resulting from each screen must be small. The process of decomposing the medium into several independent weak phase screens is equivalent to the Markov approximation, which is usually used in the analytical approaches to problems of this kind.

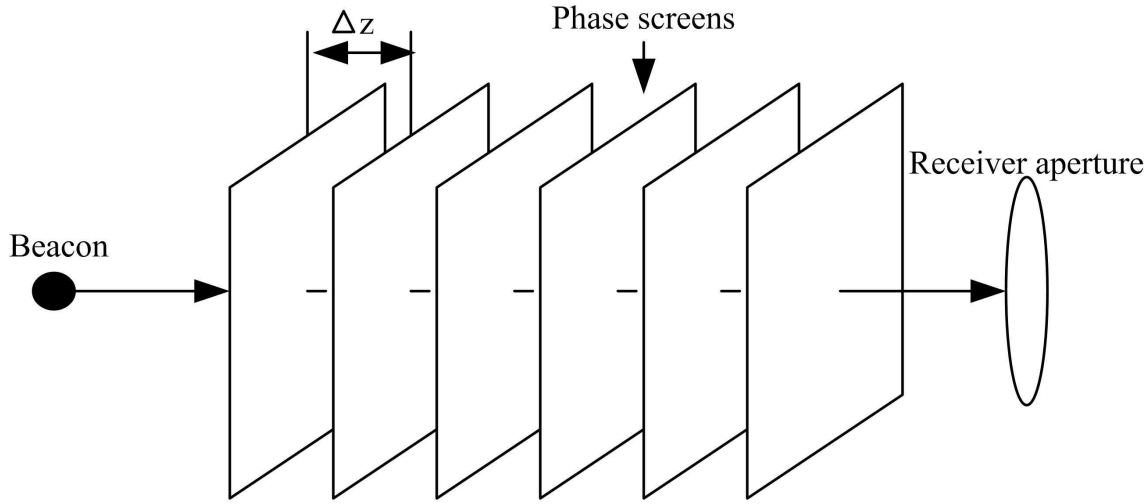

Figure 2.1: A layered model of beam propagation through a turbulent medium. The beam propagates through a number of phase screens before it reaches the receiver aperture. Each phase screen represents a turbulent atmosphere layer with a thickness of Δz. Between each two phase screens, the beam propagates in the free space.

A layered model, as shown in Fig. 2.1, is often used in the numerical simulations of beam propagation through a turbulent atmosphere [2,87,88]. In this model, the extended turbulent atmosphere is divided into slabs with a thickness of Δz. Each slab is represented by an independent thin weak phase screen, which characterizes the statistical properties of the turbulence in that slab. Each phase screen introduces an independent random phase fluctuation to the incident wave when the beam passes through it from the left at z, expressed as

$$f(x, y, z^+) = f(x, y, z^-) \exp\left(i\theta_n(x, y)\right), \tag{2.1}$$

where $\theta_n(x, y)$ is the phase fluctuations in the n-th random phase screen, $f(x, y, z^-)$ is the incident wave just before the phase screen and $f(x, y, z^+)$ is the wave field just after the phase screen. There are no changes in the amplitude when the beam passes through this

thin phase screen. The beam then propagates in the free space for a distance of Δz until it reaches the next random phase screen. This free-space propagation of a phase-distorted wavefront between two phase screens gives rise to amplitude variations in the wave field. This procedure is repeated until the beam passes through all of the phase screens and finally reaches the system receiver aperture. The simulations with this layered model will produce valid estimates, especially when a medium is generally difficult to deal with analytically.

In the physical atmosphere, the motion of turbulent air gives rise to randomly distributed eddies, each having a characteristic temperature. As a result, the index of refraction of atmosphere is random because it is very sensitive to the temperature of the atmosphere. Many realistic formulations have been developed to model the spectrum of the index of refraction fluctuations [2,8,87,89]. A von Kármán spectrum is widely used as it is consistent with the physical observation. It can be expressed approximately as

$$\Phi_n(k, \Delta z) = \frac{0.033 C_n^2(\Delta z)}{[k^2 + (2\pi/L_0)^2]^{11/6}}, \tag{2.2}$$

where k is the wave number; L_0 is the outer scale of the turbulence and it is independent of the thickness of atmosphere layer Δz; C_n^2 is the structure constant of the index of refractive fluctuations with the units of $\mathrm{m}^{-2/3}$, which characterizes the strength of atmospheric turbulence in the layer. The notation $C_n^2(\Delta z)$ is used to indicate the dependence of the turbulence strength in an atmosphere layer upon the layer thickness Δz. In numerical simulations, the turbulence strength is set to be constant in all atmosphere layers for computational convenience. Therefore, Φ_n is only a function of the wave vector in these cases.

The fluctuations of the index of refraction in the layer of turbulent atmosphere modulate the phase of the beam when it passes through this layer. As a result, phase fluctuations arise in the wavefront. In the layered model, the phase of the beam is modulated as in Eq. (2.1) by the phase fluctuations in each phase screen. The statistics of the phase fluctuations are characterized by a two-dimensional spectrum of phase fluctuations $\Phi_\theta(k, \Delta z)$, which is a function of k and the thickness of atmosphere layer Δz. Here, the subscription θ denotes the phase function. This spectrum $\Phi_\theta(k, \Delta z)$ is related to $\Phi_n(k, \Delta z)$ under the Markov approximation, given by

$$\Phi_\theta(k, \Delta z) = 2\pi k^2 \Delta z \Phi_n(k, \Delta z). \tag{2.3}$$

In the layered model of beam propagation in a turbulent atmosphere, each random phase screen possesses the desired statistics defined by a two-dimensional spectrum of

phase fluctuations, $\Phi_\theta(k, \Delta z)$. The generation of phase screens can be performed by a well-known method of filtering the white Gaussian noise with $\Phi_\theta(k, \Delta z)$ [90], given by

$$\theta_1 + i\theta_2 = \mathcal{F}^{-1}\left\{[a(k) + ib(k)]\left[\Phi_\theta(k, \Delta z)\right]^{1/2}\right\}, \tag{2.4}$$

where $\mathcal{F}^{-1}\{\cdot\}$ denotes the inverse Fourier transform, $[a(k) + ib(k)]$ are pseudo-random complex variables generated in the frequency domain, with a Gaussian distribution function and plane power spectra (Gaussian white noise). Here, $a(k)$ and $b(k)$ are uncorrelated random variables. With Eq. (2.3), a final expression for the generation of phase screens can be,

$$\theta_1 + i\theta_2 = (2\pi k^2 \Delta z)^{1/2} \mathcal{F}^{-1}\left\{[a(k) + ib(k)]\left[\Phi_n(k, \Delta z)\right]^{1/2}\right\}. \tag{2.5}$$

The inverse Fourier transform procedure in Eq. (2.5) can be carried out by the fast Fourier transform (FFT) algorithm [91]. From this inverse Fourier transform procedure, two random phase screens can be obtained. Either the real or imaginary part of the result computed in this manner may be chosen as a random phase screen. However, large numerical effects may arise near the edges of the resulting random field owing to the inherent periodicity of the FFT. To avoid these errors, a random phase screen may be created in a $2N \times 2N$ array while only the central $N \times N$ section is used in the numerical simulations.

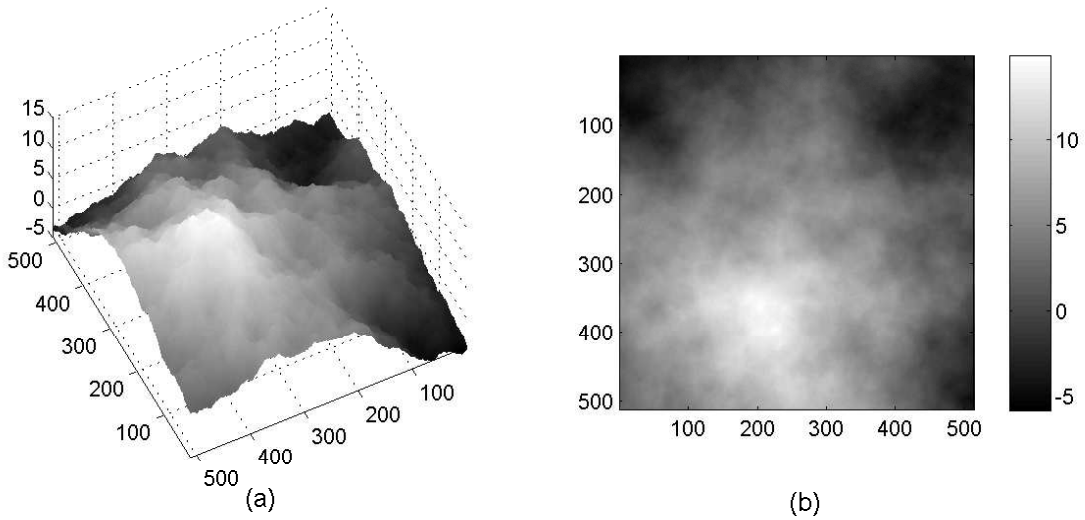

Figure 2.2: The surface plot (a) and the gray scale image (b) of a random phase screen, created with a von Kármán spectrum to simulate a turbulent atmosphere layer with a thickness of 1 km. The strength of turbulence is controlled by $C_n^2 = 4 \times 10^{-17}\ m^{-2/3}$. The outer scale of turbulence is $L_0 = 100$ m.

With this random phase screen technique and the layered model, the strength of the atmospheric turbulence can be controlled in the numerical simulations for beam prop-

agation by applying different values of the structure constant of the index of refractive fluctuations. Fig. 2.2 shows an example of the central 512×512 section of a random phase screen created in a 1024×1024 array with the FFT. It possesses a von Kármán spectrum to simulate a turbulent atmosphere layer with a thickness of 1 km. The turbulence strength of this atmosphere layer is characterized by $C_n^2 = 4 \times 10^{-17}$ m$^{-2/3}$. The wavefront will be modulated by such a random phase screen when the wave passes through it as in Eq. (2.1). A further propagation will cause amplitude fluctuations in the wave field due to the distorted wavefront.

The beam may become strongly scintillated after it passes through all of the random phase screens in a layered model which simulates a long distance or a strongly turbulent optical path. The strength of scintillation in the optical path is usually characterized by the variance of the logarithm of the ratio of the actual amplitude at a point to the amplitude of the field resulting from free-space propagation of the same source, that is, the log amplitude variance σ_χ^2 [7, 37], which can be estimated from the intensity in a system aperture, given by

$$\sigma_\chi^2 = \frac{1}{4}\ln(\sigma_I^2 + 1), \tag{2.6}$$

where I is the intensity of the field at a point in the system aperture, and σ_I^2 can be estimated from

$$\sigma_I^2 = \frac{E\{I^2\} - (E\{I\})^2}{(E\{I\})^2}, \tag{2.7}$$

where $E\{I\}$ and $E\{I^2\}$ are the first and second moments of the intensity respectively.

When σ_χ^2 is smaller than 0.3, it is possible to calculate σ_χ^2 for a case of beam propagation through random phase screens by the Rytov approximation, as a so-called Rytov variance $\sigma_{\chi,R}^2$ [4, 92]. The Rytov variance $\sigma_{\chi,R}^2$ can be computed for the plane wave propagation through an optical path with a constant C_n^2, given by

$$\sigma_{\chi,R}^2 = 0.307 k^{7/6} L^{11/6} C_n^2, \tag{2.8}$$

and similarly for the spherical wave as

$$\sigma_{\chi,R}^2 = 0.124 k^{7/6} L^{11/6} C_n^2, \tag{2.9}$$

where L is the propagation distance and $k = 2\pi/\lambda$ is the wave number.

Another crucial quantity is the Fried parameter (or Fried's coherence length) [93], r_0, which is the single most important parameter [4] describing the quality of the wave that has propagated through the turbulent atmosphere. This parameter incorporates the turbulence strength C_n^2, the wavelength λ and the propagation distance L, which can be

expressed for the plane wave as [2, 4]

$$r_0 = 0.185 \left(\frac{\lambda^2}{C_n^2 L} \right)^{3/5}, \tag{2.10}$$

and for the spherical wave as

$$r_0 = 0.331 \left(\frac{\lambda^2}{C_n^2 L} \right)^{3/5}. \tag{2.11}$$

The Fried parameter can be physically interpreted as the aperture size, which has the same resolution as a diffraction-limited aperture without turbulence [93, 94]. The r_0 parameter can also be defined as the diameter of a wavefront area over which the root mean square phase variations due to atmosphere are equal to 1 rad. A typical value for r_0 in the visible region of spectrum lies in the range of a few ten-centimeters.

2.3 Adaptive optics

2.3.1 Principle of adaptive optics

After propagating through the turbulent atmosphere over a long distance, the wavefront may be severely distorted, which causes the degradation of performance in an optical system. AO systems are usually used to correct the incident or outgoing wave in such an optical system. Fig. 2.3 shows a conventional AO imaging system, which includes the deformable mirror, the wavefront sensor and the wavefront computer.

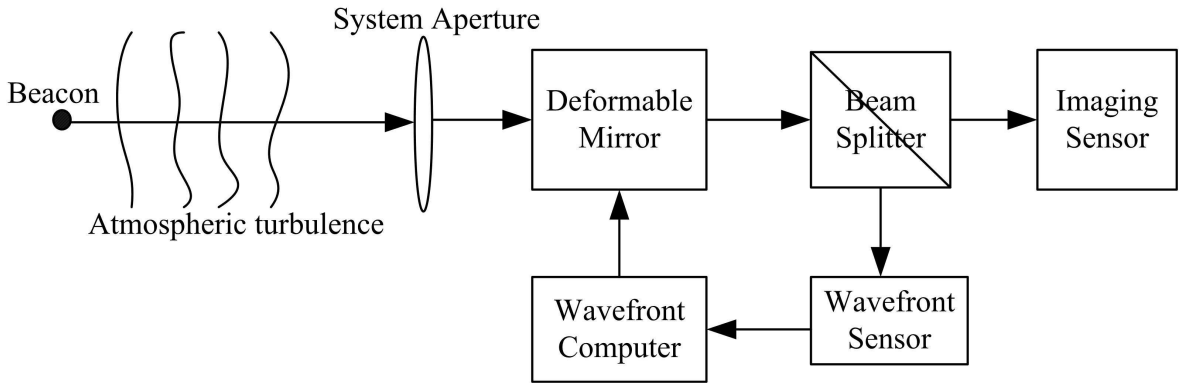

Figure 2.3: Diagram of an AO imaging system.

In this AO system, the wavefront sensor measures the phase profile of an incident perturbed optical wave field, which can be generally presented as $A\exp[i\theta(\mathbf{x})]$, where A

and θ are the amplitude and the phase, respectively, and $\mathbf{x}$ is the position vector in the system aperture. The measured data are sent to the computer to calculate and reconstruct the wavefront and the control signals for the deformable mirror. The flexible surface of a deformable mirror can be shaped according to the wavefront control signals at high speed. If the figure of the deformable mirror surface is $\hat{\theta}(\mathbf{x})$, then the optical field just after reflecting from the deformable mirror can be expressed as

$$A\exp[i\epsilon(\mathbf{x})] = A\exp\left[i\left(\theta(\mathbf{x}) - \hat{\theta}(\mathbf{x})\right)\right]. \tag{2.12}$$

In an ideal AO system, the deformable mirror surface can be shaped exactly according to the perturbed wavefront $\theta(\mathbf{x})$ and then the residual phase error $\epsilon(\mathbf{x})$ will be zero. In this way, the deformable mirror can implement this phase conjugation [53, 95] on the perturbed wavefront. After reflecting from the deformable mirror, the wavefront becomes planar and may then form a high-quality image on the imaging sensor. By this means, an AO system is in principle able to correct atmospheric turbulence in real time.

2.3.2 Shack-Hartmann wavefront sensor

Various types of wavefront sensors are used in an AO system, such as the Shack-Hartmann wavefront sensor and the shearing interferometer wavefront sensor. These wavefront sensors measure the phase slopes of the incident wavefront. In this thesis, it is mainly concentrated on the Shack-Hartmann wavefront sensor due to its simplicity in applications.

The Shack-Hartmann wavefront sensor uses a lenslet array to sample the wavefront, as shown in Fig. 2.4. The focal points may be located on, before or after the back focal plane of the lenslet array due to the shape of the incident wavefront. At the same time, the focal points may also have a lateral or longitudinal shifts on the focal plane due to the slope of the wavefront. The slope for each of these samples is given by the location of the focal point formed by each lenslet in its back focal plane. To simplify the analysis the lenslet array is assumed to be a square array of lenslets, each with a square-shaped subaperture, as shown in Fig. 2.5. A detector array, such as a charge coupled device (CCD), is placed in the back focal plane of the lenslet array. A small subarray of this detector array is dedicated to each lenslet of the lenslet array. This subarray is used to determine the location of the focal point produced by each lenslet. The location of the focal point for the (m, n)-th subaperture (lenslet) is given by a position vector $\mathbf{u}^{m,n}$ that is calculated

from the centroid of the measured intensity distribution in the back focal plane,

$$\mathbf{u}^{m,n} = \frac{\int_H I(\mathbf{u})\mathbf{u}\ \mathrm{d}^2u}{\int_H I(\mathbf{u})\ \mathrm{d}^2u} - \mathbf{u_0}^{m,n}, \tag{2.13}$$

where $\mathbf{u_0}^{m,n}$ is the location of the focal point for a normally incident plane wave; $I(\mathbf{u})$ is the intensity distribution over the detector plane; H is the window of the subarray of detectors on the detector plane; and d^2u is the two-dimensional integration measure on the detector plane.

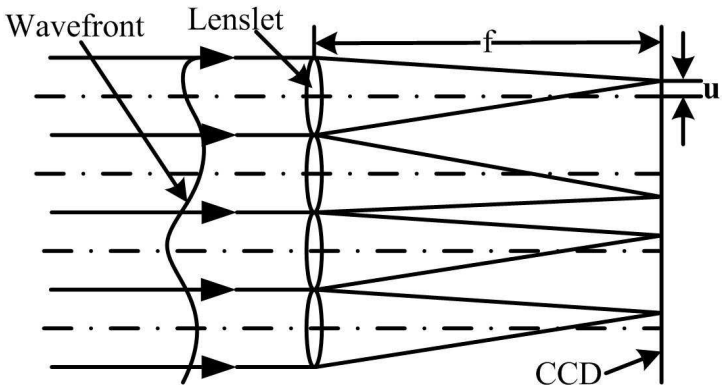

Figure 2.4: One-dimensional representation of a Shack-Hartmann wavefront sensor.

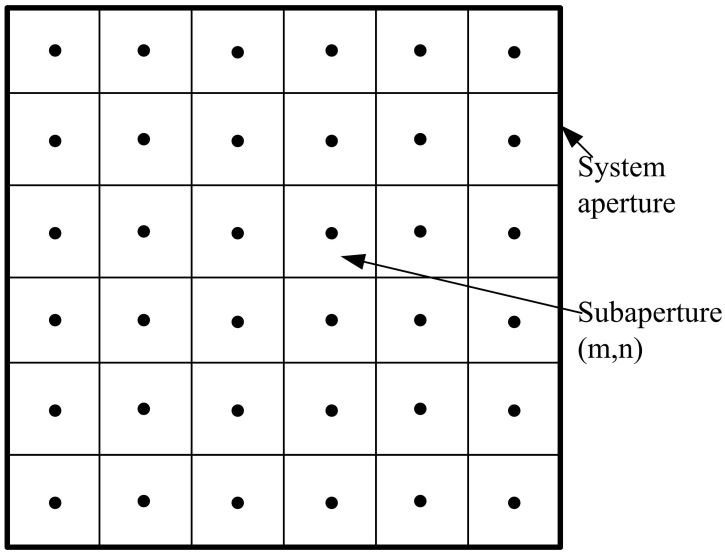

Figure 2.5: An array of subapertures (small squares) within the system aperture of the Shack-Hartmann wavefront sensor. The average phase slope values are associated with the dots inside the small squares.

The average phase slope for each subaperture is given by the location of the focal point, as determined by the intensity centroid in Eq. (2.13). This relationship follows from the Fourier relationship, between the phase tilt of the incident wave in front of a

lens and the location of the resulting focal point behind it, as portrayed in Fig. 2.6. So the average phase slope over the (m, n)-th subaperture can be expressed as

$$\mathbf{G}^{m,n} = \frac{\int_\Omega \nabla\theta(\mathbf{x})\ \mathrm{d}^2x}{\int_\Omega\ \mathrm{d}^2x} = \frac{k}{f}\mathbf{u}^{m,n}, \tag{2.14}$$

where $\nabla\theta(\mathbf{x})$ is the gradient of the phase function of the incident wave; $\mathbf{x}$ denotes the two-dimensional position vector on the lenslet plane; $k(= 2\pi/\lambda)$ is the wave number; f is the focal length of the lenslets; Ω is the area of the lenslet subaperture; and $\mathbf{u}^{m,n}$ is the location of the (m, n)-th focal point on the detector plane, as defined in Eq. (2.13). The $\mathbf{G}^{m,n}$-values given by Eq. (2.14) represent the sampled output vector field of the Shack-Hartmann wavefront sensor. Each value is associated with a point in the centre of the particular subaperture, as denoted by the dots in Fig. 2.5.

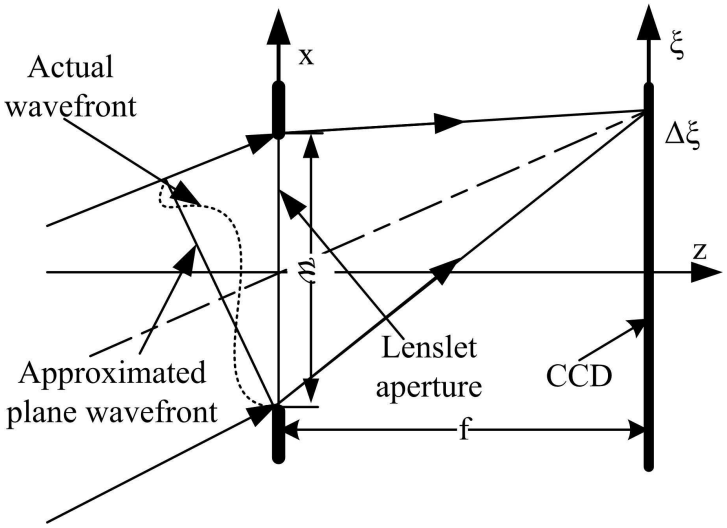

Figure 2.6: One-dimensional representation of one lenslet in the Shack-Hartmann wavefront sensor, showing the shift of the focal point due to the average tilt of the incident wavefront.

The relative error of image centroid measurements is associated with scintillations when a Shack-Hartmann wavefront sensor is used to measure the distorted wavefront of a scintillated beam in an AO system [96]. In the condition with a given strength of turbulence , this relative error will increase as the ratio of the subaperture size w to the Fried parameter r_0 increases. It is known that the Shack-Hartmann wavefront sensor, for the uniform distribution of the strength of turbulence, provides poor estimation accuracy when the ratio of the subaperture size w to the Fried parameter r_0 is more than 0.25 [25].

2.3.3 Deformable mirror

Another important component in an AO system is the deformable mirror. A deformable mirror is a thin reflective glass with a flexible surface that is bonded on an array of actuators. The actuators can pull or push against the mirror surface to change its shape according to the measured wavefront from the wavefront sensor. By deforming its surface to match the shape of the perturbed wavefront, a deformable mirror may perform the wavefront correction.

Real deformable mirrors have only a finite number of degrees of freedom due to the use of the discrete actuator array. The n-th influence function describes how the n-th actuator changes the surface shape of the local region in the mirror surface with a unit signal. Different functions, such as polynomials, trigonometric functions and super-Gaussian functions, may be used to represent the deformable mirror influence functions [4]. Therefore, the phase profile formed by a deformable mirror can be expressed as

$$\hat{\theta}(\mathbf{x}) = \sum_n c_n r_n(\mathbf{x}), \tag{2.15}$$

where c_n is the control signal applied on the n-th actuator and $r_n(\mathbf{x})$ is the n-th influence function.

2.3.4 Phase reconstruction

The outputs of a wavefront sensor in the horizontal and vertical directions are sampled phase differences, which can be estimated as

$$\Delta\theta^x_{m,n} = \theta_{m+1,n} - \theta_{m,n}, \tag{2.16}$$

$$\Delta\theta^y_{m,n} = \theta_{m,n+1} - \theta_{m,n}, \tag{2.17}$$

where $\theta_{m,n}$ is the phase needing to be reconstructed; $\Delta\theta^x_{m,n}$ and $\Delta\theta^y_{m,n}$ denote the phase difference in the x and y direction respectively.

The least-squares solution to the phase function is the solution to the discretized Poisson's equation, which can be expressed as [33]

$$(\theta_{m+1,n} - 2\theta_{m,n} + \theta_{m-1,n}) + (\theta_{m,n+1} - 2\theta_{m,n} + \theta_{m,n-1}) = \varrho_{m,n}, \tag{2.18}$$

where

$$\varrho_{m,n} = (\Delta\theta^x_{m,n} - \Delta\theta^x_{m-1,n}) + (\Delta\theta^y_{m,n} - \Delta\theta^y_{m,n-1}). \tag{2.19}$$

Eq. (2.18) represents the relationship between the wavefront sensor measured phase difference $\Delta\theta$ and the same sampled input phase θ. It can also be rewritten in matrix notation as,

$$\mathbf{P}\bar{\theta} = \Delta\bar{\theta}, \tag{2.20}$$

where $\mathbf{P}$ is a matrix representing the physical relationships between the phase and the phase differences, $\Delta\bar{\theta}$ and $\bar{\theta}$ are regarded as one-dimensional vectors of the phase differences and the sampled phase respectively. Therefore, the perturbed wavefront then can be reconstructed with a least-squares estimate of θ, given by [26, 33]

$$\bar{\theta}_{LS} = (\mathbf{P}^T\mathbf{P})^{-1}\mathbf{P}^T\Delta\bar{\theta}, \tag{2.21}$$

where $\bar{\theta}_{LS}$ is also a one-dimensional vector containing the estimated phase values. The elements of the vector $\bar{\theta}_{LS}$ can be rearranged into an two-dimensional array denoted by θ_{LS}, which is the least-squares reconstructed phase for the perturbed wavefront.

The least-squares estimate in Eq. (2.21) can usually be fulfilled with a particular two-dimensional discrete cosine transform (DCT). By performing the DCT of the matrixes of θ and ϱ and substituting them into both sides of Eq. (2.18), the least-squares estimated phase can be obtained in DCT domain as [33]

$$\hat{\theta}_{m,n} = \frac{\hat{\varrho}_{m,n}}{2\cos(m\pi/M) + 2\cos(n\pi/N) - 4}, \tag{2.22}$$

where (M, N) is the array size and $\hat{\varrho}$ is the DCT of ϱ. Therefore, the least-squares reconstructed phase function θ_{LS} can be found by taking the inverse DCT of $\hat{\theta}$.

2.4 Optical vortices

2.4.1 Description of an optical vortex

An optical vortex [39, 40, 62], also called a phase singularity or a branch point, is a screw dislocation where the amplitude goes to zero and the phase is undefined in a complex optical field. Around the vortex core, the phase increases by a value of $\tau 2\pi$ with the integer τ being referred to as the topological charge of the vortex. The direction of the phase increment indicates the sign of the vortex topological charge. Therefore, a vortex can be positive or negative. If the phase increment around the vortex is linear with the azimuthal angle, this vortex is called a canonical vortex. Otherwise it is called a noncanonical vortex. Two adjacent oppositely charged vortices form an optical vortex dipole.

In general, the complex amplitude function, $V_c(x, y)$, of a canonical vortex can be expressed in Cartesian coordinates as,

$$V_c(x, y) = x \pm iy. \tag{2.23}$$

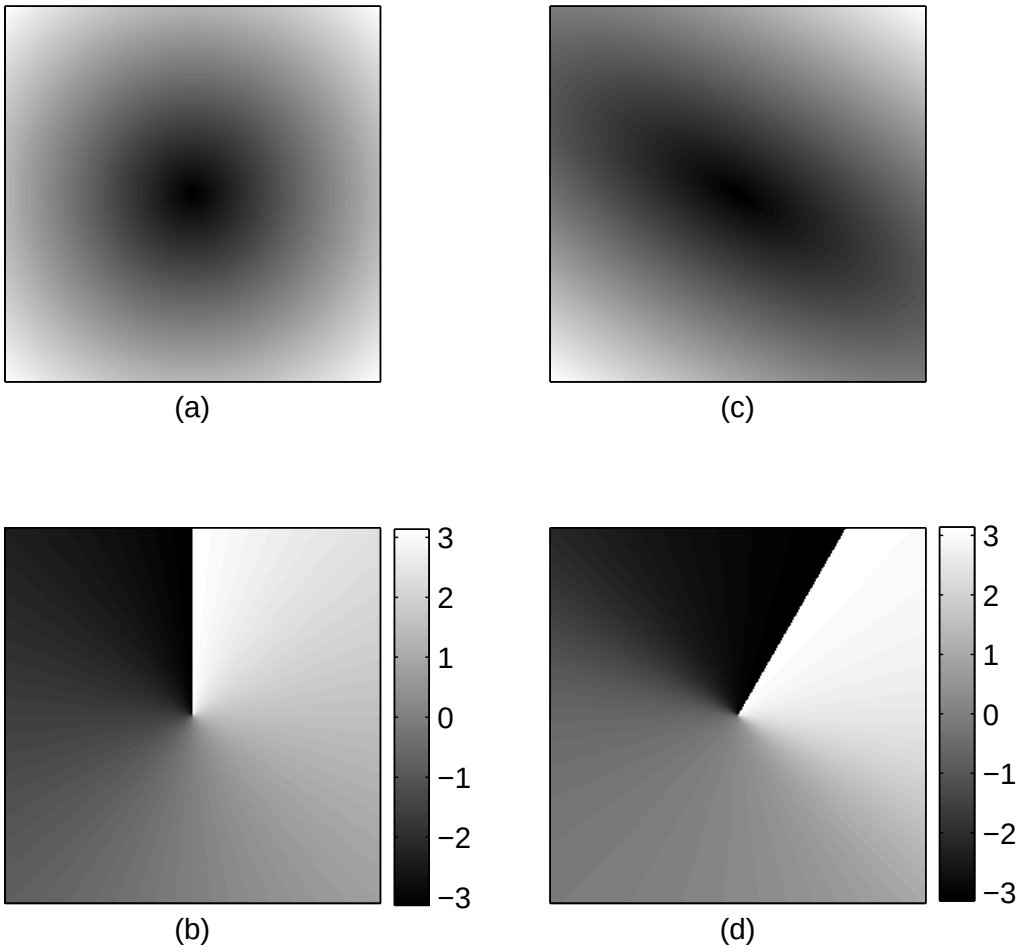

Figure 2.7: Amplitude (a) and phase (b) profiles of a canonical vortex. Amplitude (c) and phase (d) profiles of a noncanonical vortex, with anisotropy angle $\alpha = \pi/4$ and orientation angle $\beta = \pi/3$.

The complex amplitude function, $V(x, y)$, of a noncanonical vortex can be expressed by a linear combination of two canonical vortices [97, 98], given by

$$V(x, y) = \frac{1}{\sqrt{2}} \left[\xi(x + iy) + \zeta(x - iy)\right], \tag{2.24}$$

where

$$\xi = \cos(\alpha/2) \exp(i\beta/2), \tag{2.25}$$

$$\zeta = \sin(\alpha/2) \exp(-i\beta/2), \tag{2.26}$$

and the angles, $0 < \alpha < \pi$ and $0 < \beta < 2\pi$, respectively denote the anisotropy and orientation of the vortex.

Anisotropy and orientation describe the morphology of a vortex. Fig. 2.7 shows an example of the amplitude and the phase of a canonical optical vortex and a noncanonical vortex. Comparing the amplitude and phase profiles of a canonical vortex and a noncanonical vortex depicted in Fig. 2.7, it can be seen that an anisotropic (noncanonical) vortex has an elliptical appearance, which is scaled in a particular direction. A noncanonical vortex can be viewed as a squeezed canonical vortex.

The presence of an optical vortex in a phase function can be determined with the aid of a closed line integral over the gradient of the phase function [26],

$$\oint_C \nabla\theta \cdot \mathrm{d}l = \tau 2\pi, \tag{2.27}$$

where C denotes the closed integration contour; $\nabla\theta$ is the gradient of the phase function and τ is an integer that presents the net topological charge of all the vortices enclosed by the contour.

2.4.2 Vortex trajectory and morphology in a Gaussian beam

Gaussian functions are analytically tractable and widely used to represent laser beams. The propagation of Gaussian beams is well understood. Analytical expressions of the optical quantities associated with optical vortices in Gaussian beams can be derived and studied. Here, the trajectories and morphology evolution of an optical vortex dipole embedded in a Gaussian beam are briefly reviewed [69, 75].

In this thesis, the normalized transverse coordinates (u, v, t) will be used for convenience. The transverse coordinates, (x, y), are normalized by the Gaussian beam waist size ω, as $u = x/\omega$ and $v = y/\omega$. The propagation distance z is normalized by the Rayleigh range $R = \pi\omega^2/\lambda$, as $t = z/R$.

For a vortex dipole in a Gaussian beam, four coordinates is needed to describe the locations of two arbitrary vortices. Here only canonically launched vortices are considered. Owing to the rotational symmetry of a circular Gaussian beam, the v coordinates of the two vortex locations can be set as equal. Hence, the two oppositely charged vortices are initially located at $(\Delta u + u_0, v_0)$ and $(\Delta u - u_0, v_0)$ in the so-called launch plane at $t = t_0$. The beam prefactor for this canonical vortex dipole can then be expressed by

$$P(u, v, t_0) = [(u - \Delta u - u_0) + i(v - v_0)][(u - \Delta u + u_0) - i(v - v_0)]. \tag{2.28}$$

With Fresnel diffraction, the expression for the beam prefactor can be obtained at any arbitrary propagation distance t,

$$P(u,v,t) = [(u-a-\chi\Delta u)+i(v-b+\gamma\Delta u)][(u+a-\chi\Delta u)-i(v-b-\gamma\Delta u)]-\sigma\gamma(\gamma+i\chi), \tag{2.29}$$

where parameters are given by,

$$a = u_0\chi + v_0\gamma,\ b = v_0\chi - u_0\gamma, \tag{2.30}$$

$$\chi = (1+tt_0)/\sigma,\ \gamma = (t-t_0)/\sigma \text{ and } \sigma = 1+t_0^2. \tag{2.31}$$

From Eq. (2.29), the explicit expressions of the trajectories of a vortex dipole can be found as functions of the propagation distance t [69],

$$u_{1,2}(t) = \frac{\gamma^2\Delta u\sigma\chi \pm a\mathcal{D}^{1/2}}{2(\gamma^2\Delta u^2+a^2)} + \chi\Delta u, \tag{2.32}$$

$$v_{1,2}(t) = \frac{\gamma\left(a\sigma\chi \mp \Delta u\mathcal{D}^{1/2}\right)}{2(\gamma^2\Delta u^2+a^2)} + b, \tag{2.33}$$

where the subscripts 1 and 2 refer to the two vortices of the dipole respectively; the two signs are respectively associated with the two vortices of the dipole; the discriminant $\mathcal{D}$ is given by

$$\mathcal{D} = [\gamma^2(2\Delta u^2+\sigma)+2a^2]^2 - \sigma^2\gamma^2(\chi^2+\gamma^2). \tag{2.34}$$

Here, $\mathcal{D}=0$ implies the critical points where the vortices are created or annihilated in pairs. From Eq. (2.29), It can be seen that this field contains a coupling term, $-\sigma\gamma(\gamma+i\chi)$, which makes the vortices behave non-linearly. According to the vortex trajectories in Eqs. (2.32) and (2.33), vortices in a dipole will either move apart from each other or annihilate each other during beam propagation.

The vortex morphologies can be obtained directly from the complex amplitude distribution, $U(u,v)$, of the beam at the location of the vortex [99], given by

$$\alpha = \arccos\left(\frac{|f_-|^2-|f_+|^2}{|f_-|^2+|f_+|^2}\right), \tag{2.35}$$

$$\beta = \frac{i}{2}\ln\left(\frac{f_+f_-^*}{f_+^*f_-}\right), \tag{2.36}$$

where α represents the vortex anisotropy angle and β represents the relative orientation angle for the vortex and

$$f_\pm = \frac{1}{\sqrt{2}}\left(\frac{\partial U}{\partial u} \pm i\frac{\partial U}{\partial v}\right), \tag{2.37}$$

and * represents the complex conjugate.

Similarly, the explicit expressions for the morphology of the vortices in a dipole can be found as functions of the propagation distance t [75],

$$\cos(\alpha) = \pm\frac{\mathcal{D}^{1/2}}{\gamma^2(\sigma + 2\Delta u^2) + 2a^2}, \tag{2.38}$$

$$\tan(\beta) = \pm\frac{\chi\mathcal{D}^{1/2}}{\gamma(2a^2 + 2\gamma^2\Delta u^2 - \chi^2\sigma)}, \tag{2.39}$$

where the two signs are respectively associated with the two vortices in a dipole. Note that the morphologies of the vortices will change immediately after the launch plane and they will never become canonical again along the propagation direction. When the vortices are annihilated at the critical point where the discriminant $\mathcal{D} \to 0$, both $\cos(\alpha)$ and $\tan(\beta)$ approach zero. This implies that these two vortices will be squeezed severely into two edge dislocations in alignment and then annihilate each other when $\mathcal{D} \to 0$.

2.4.3 Optical vortices in a scintillated beam

The phase function of a scintillated optical beam can in general be represented by the sum of a continuous phase function and an arbitrary number of optical vortices as

$$\theta(x, y) = \theta_c(x, y) + \sum_{n}^{N} \phi(x - x_n, y - y_n; \alpha_n, \beta_n), \tag{2.40}$$

where $\theta_c(x, y)$ is the continuous background phase function; $\phi(x - x_n, y - y_n; \alpha_n, \beta_n)$ represents the phase function of a noncanonical vortex with its anisotropy angle α_n and orientation angle β_n, located at (x_n, y_n); N denotes the number of the vortices in the wave field.

Chapter 3

Optical vortex detection with a Shack-Hartmann wavefront sensor

3.1 Introduction

While AO systems are able to remove moderate wavefront distortions in scintillated optical beams, optical vortices that appear in strongly scintillated beams can severely degrade the performance of such an AO system. Therefore the detection of these optical vortices is an important aspect of strong-scintillation AO. In this chapter the detection of the locations and topological charges of the optical vortices is implemented with the aid of the solenoidal part of the phase gradient function. The Shack-Hartmann wavefront sensor is widely used to measure the phase slopes of the distorted wavefront in AO systems. It is shown that the Shack-Hartmann wavefront sensor is not completely insensitive to the phase function of an optical vortex. In other words, this phase function is not completely hidden, but is contained in the solenoidal part of the output of the Shack-Hartmann wavefront sensor. Therefore it can be used to locate the optical vortices that are present in the wavefront.

The effect of the averaging process on an optical vortex in the Shack-Hartmann wavefront measurement is analyzed by performing the actual integration of the phase gradient function of such a vortex over the area of a wavefront sensor subaperture. From this result it can be seen that it is possible to extract the required information of the optical vortices regardless of the effects of the averaging process. For a continuous vector field the vortices can be identified by computing the curl of this vector field. The output from a Shack-Hartmann wavefront sensor is in the form of a sampled vector field that approx-

imately represents the gradient of the phase function of the scintillated beam. The curl operation is implemented on this sampled vector field in terms of finite differences. This finite difference curl operation is referred to as the circulation of the sampled vector field. The complete detection process thus consists of the averaging process performed by the Shack-Hartmann wavefront sensor subapertures and the circulation process performed on its output. The effect of the morphology and relative position of the vortex on this detection process is also investigated.

The remainder of the chapter is organized as follows. In Section 3.2 the principle upon which the detection of optical vortices is based and some notations are provided. In Section 3.3 the detection of optical vortices with the output of the Shack-Hartmann wavefront sensor is discussed. This detection is analyzed for a canonical optical vortex and the peak value is computed in Subsection 3.3.1 and then this analysis is repeated for the more general noncanonical optical vortex in Subsection 3.3.2. The complete expression of the circulation for a noncanonical optical vortex is also provided. Numerical investigations are provided in Section 3.4 to test the procedure on more realistic data. A summary and conclusions are provided in Section 3.5.

3.2 Theory of vortex detection

In general, the phase function of a vortex with arbitrary morphology can be expressed as

$$\phi(x, y; \alpha, \beta) = -\frac{i}{2} \ln \left[\frac{\xi(x + iy) + \zeta(x - iy)}{\xi^*(x - iy) + \zeta^*(x + iy)} \right], \tag{3.1}$$

where * represents the complex conjugate; ξ and ζ respectively represent the anisotropy and the orientation of the vortex morphology in terms of the morphology angles α and β, as in Eqs. (2.25) and (2.26).

The output of a Shack-Hartmann wavefront sensor, which measures the gradient of the phase function, can be used to implement a vortex detection procedure with a physical system. For the moment it is assumed that this measurement is ideal. The output of a Shack-Hartmann wavefront sensor can be viewed as a vector field $\mathbf{G} = G_x(x, y)\hat{x} + G_y(x, y)\hat{y}$. If this vector field represents the gradient of a continuous phase function, it must have

$$\frac{\partial G_x(x, y)}{\partial y} = \frac{\partial G_y(x, y)}{\partial x}. \tag{3.2}$$

If it is found that this is not the case then it indicates that $\mathbf{G}$ cannot be the gradient of a continuous phase function. This points to the presence of optical vortices. The extent to

which the equality in Eq. (3.2) fails is given by the difference between its left-hand and right-hand sides, which becomes the curl of the vector field. Since the vector field only has x- and y-components that only depend on x and y, its curl is a scalar which represents the z-component given by

$$D(x, y) = \nabla_T \times \mathbf{G}(x, y). \tag{3.3}$$

If the phase function of a scintillated optical beam is continuous (without optical vortices), the curl of the gradient of the phase function would give zero. On the other hand, if there are optical vortices in the phase function of the beam, then the curl of this gradient is not zero [100]. Each vortex gives a Dirac delta function at the location of the vortex,

$$\nabla\times\nabla\phi(x, y, \alpha, \beta) = \tau 2\pi\delta(x)\delta(y), \tag{3.4}$$

where $\tau(= \pm 1)$ is the topological charge of the vortex. So the curl of the gradient of a phase function $\theta(x, y)$ that contains optical vortices gives a sum of Dirac delta functions, each multiplied by the topological charge of the vortices,

$$\nabla\times\nabla\theta(x, y) = 2\pi \sum_n \tau_n \delta(x - x_n)\delta(y - y_n). \tag{3.5}$$

By the same token the curl of the output vector field of a Shack-Hartmann wavefront sensor, shown in Eq. (3.3), gives us, according to Eq. (3.5), a distribution of optical vortices, showing us where they are located and what their topological charges are. The curl $D(x, y)$, as shown in Eq. (3.3), can be easily computed from $\mathbf{G}$ and then use the result to identify the optical vortices in the wavefront.

In the above discussion it is assumed to be the ideal case, which ignores the effects of the discreteness and finite size of the subapertures of the Shack-Hartmann wavefront sensor. The effect of the finite subapertures of the Shack-Hartmann wavefront sensor has been already discussed in Section 2.3.2. In the following section the Shack-Hartmann wavefront sensor will be considered more carefully. It will be seen that the subaperture size sets a scale beneath which optical vortices become unobservable and it also modifies the weight of 2π by which each vortex is multiplied.

3.3 Vortex detection with a Shack-Hartmann wavefront sensor

In Section 2.3.2 it can be seen that the output of the Shack-Hartmann wavefront sensor in a practical AO system is a sampled vector field $\mathbf{G}$ with each sample representing

the averaged phase slopes over one subaperture, as in Eq. (2.14). As pointed out in Section 3.2, the information about the locations of the optical vortices is concealed in the solenoidal part of this vector field. To extract this information from the sampled vector field, it needs to implement the curl operation of Eq. (3.3) numerically. Such a numerical implementation is equivalent to the line integral of Eq. (2.27). The numerical computation is done by computing what is referred to as the circulation, given by

$$\begin{aligned} D^{m,n} &= \frac{w}{2}\left(G_x^{m,n} + G_x^{m,n+1} + G_y^{m,n+1} + G_y^{m+1,n+1}\right. \\ &\quad \left. -G_x^{m+1,n+1} - G_x^{m+1,n} - G_y^{m+1,n} - G_y^{m,n}\right), \end{aligned} \tag{3.6}$$

where w is the subaperture window size and the superscript m, n denotes the subaperture index. The physical implementation of the circulation process is presented in Fig. 3.1. The samples used in the calculation are denoted by the points in the centres of the

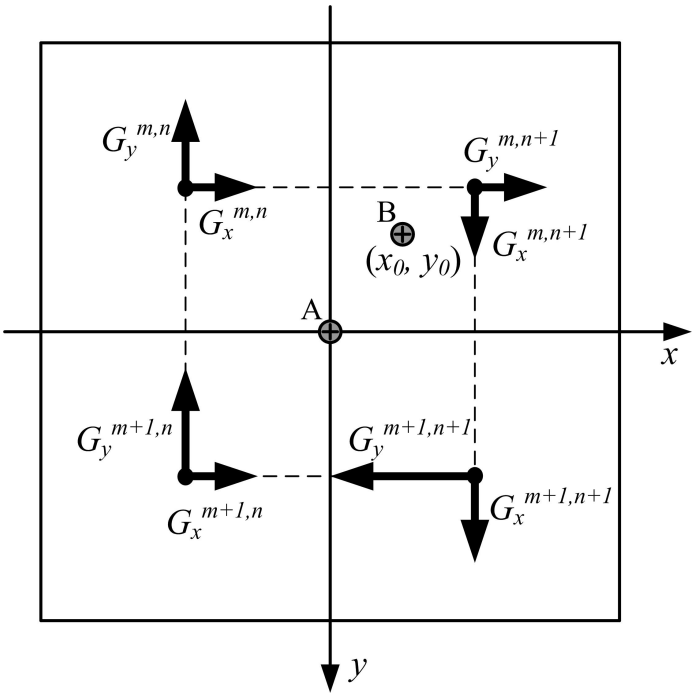

Figure 3.1: Circulation $D^{m,n}$ over four subapertures with an optical vortex located either at the centre (assumed to be the origin), denoted by **A** or at some arbitrary location (x_0, y_0) denoted by **B**. The four subapertures are represented by the four squares. The dot at the centre of each subaperture is the position with which the average phase slope value **G** of that subaperture is associated. The arrows represent the components of **G**. The dashed lines represent the contour used for the calculation of the circulation.

subapertures shown in Fig. 3.1. The circulation represents a line integral performed over the four subapertures along a contour denoted by the dashed lines. Note that the result

of this circulation operation represents a value D that should be associated with a point in the centre of the four subapertures. However, it is assigned the same index m, n that is associated with the upper left subaperture.

The continuous phase slopes and the solenoidal phase slopes can be separated from the sampled vector field $\mathbf{G}$ according to the circulation D by a method described in Appendix A. The result of this computation D is a distribution of the topological charges of the optical vortices. It is positive (negative) at the locations of optical vortices with positive (negative) topological charges and it should be zero where there are no vortices. However, this distribution is affected by the averaging process, the sampled nature of the data and, of course, noise. As a result the values are not exactly zero when there are no vortices. Moreover, the value of $D^{m,n}$ at the location of a single positive vortex is not 2π as it would be expected if the circulation is an exact implementation of the line integral Eq. (2.27). In the next two subsections, the effects of the practical implementation of the vortex detection procedure will be analyzed.

3.3.1 Canonical vortex

Here the situation where a canonical optical vortex is located in the centre of the four subapertures will be considered, as shown by point **A** in Fig. 3.1. The origin $(0, 0)$ of the coordinate system is assigned at this point. The complex amplitude function of a canonical optical vortex at the origin can be expressed as $(x \pm iy) = r \exp(\pm i\phi)$, where the sign indicates the topological charge of the vortex and r and ϕ are respectively the radial coordinate and the azimuthal coordinate. Here a positively charged vortex is considered. The phase function of the vortex is simply the azimuthal coordinate ϕ, provided that the vortex is located at the origin. The gradient of the phase function of a canonical optical vortex can then be expressed in Cartesian coordinates, as

$$\nabla\phi(x, y) = \frac{x\hat{y} - y\hat{x}}{x^2 + y^2}. \tag{3.7}$$

By substituting Eq. (3.7) into Eq. (2.14), an analytical expression for the average phase slope in the (m, n)-th subaperture can be obtain, given by

$$\begin{aligned} \mathbf{G}^{m,n} &= \frac{1}{w^2} \int_{-w}^{0} \int_{-w}^{0} \frac{x\hat{y} - y\hat{x}}{x^2 + y^2} \, \mathrm{d}x\mathrm{d}y \\ &= \left(\frac{\pi}{4w} + \frac{\ln 2}{2w} \right) (\hat{x} - \hat{y}). \end{aligned} \tag{3.8}$$

The integration boundaries are determined by the location of the (m, n)-th subaperture within the four subaperture area shown in Fig. 3.1. Because of the symmetry of the

phase function of a canonical vortex at the origin, the average phase slope values for the other subapertures will be the same apart from a change in direction. Then, according to Eqs. (3.6) and (3.8), the value for $D^{m,n}$ will be

$$D^{m,n} = 4wG_x^{m,n} = \pi + 2\ln(2) = 4.527887. \tag{3.9}$$

It is noted that the value of the circulation is $\pi + 2\ln 2$ and not the 2π that it can be found for the analytical case given by Eq. (2.27). It is the averaging process that is responsible for this difference and not the finite differences of the calculation process. It is found that if the same finite difference circulation calculation, Eq. (3.6), is performed on a sampled gradient function of a canonical optical vortex without the averaging process, the result is indeed 2π.

Although it is the averaging process that causes the difference, this circulation value is independent of the subaperture window size w. This is because the phase function of an optical vortex is scale invariant. So the difference is produced simply because some averaging takes place, but it does not matter how big the subapertures are over which the slopes are averaged.

When the vortex is not located at the origin, the centre of the four apertures, but at some other location such as position **B** at (x_0, y_0) in Fig. 3.1, it can be expected that the value of the circulation will change. The expression for the gradient of the phase function now becomes

$$\nabla\phi(x - x_0, y - y_0) = \frac{(x - x_0)\hat{y} - (y - y_0)\hat{x}}{(x - x_0)^2 + (y - y_0)^2}. \tag{3.10}$$

With Eq. (3.10) and Eq. (2.14), the average phase slopes **G** can be computed for the four subapertures. Then, with the aid of Eq. (3.6), $D^{m,n}$ can be obtained. The final expression is rather complicated. It can be obtained from the more general circulation expression for an optical vortex with arbitrary morphology and location, provided in Eq. (3.16).

Fig. 3.2 shows the circulation D as a function of the location of the vortex in terms of normalized coordinates $\mu = x_0/w$ and $\nu = y_0/w$. A top view of this function over the region $-2 < \mu < 2$ and $-2 < \nu < 2$ is shown in Fig. 3.2(a). The precise shape of the circulation function as a one-dimensional function of μ are shown in Fig. 3.2(b) for $\nu = 0$ (middle line) and for $\nu = \mu$ (diagonal). At the origin $(\mu, \nu) = (0, 0)$ the circulation function has a peak with the value $D = 4.53$, consistent with Eq. (3.9). Away from the origin the value of D decreases rapidly and approaches zero for $|\mu|, |\nu| > 1$. In some regions the value of D drops below zero. At the corners of the four subaperture area,

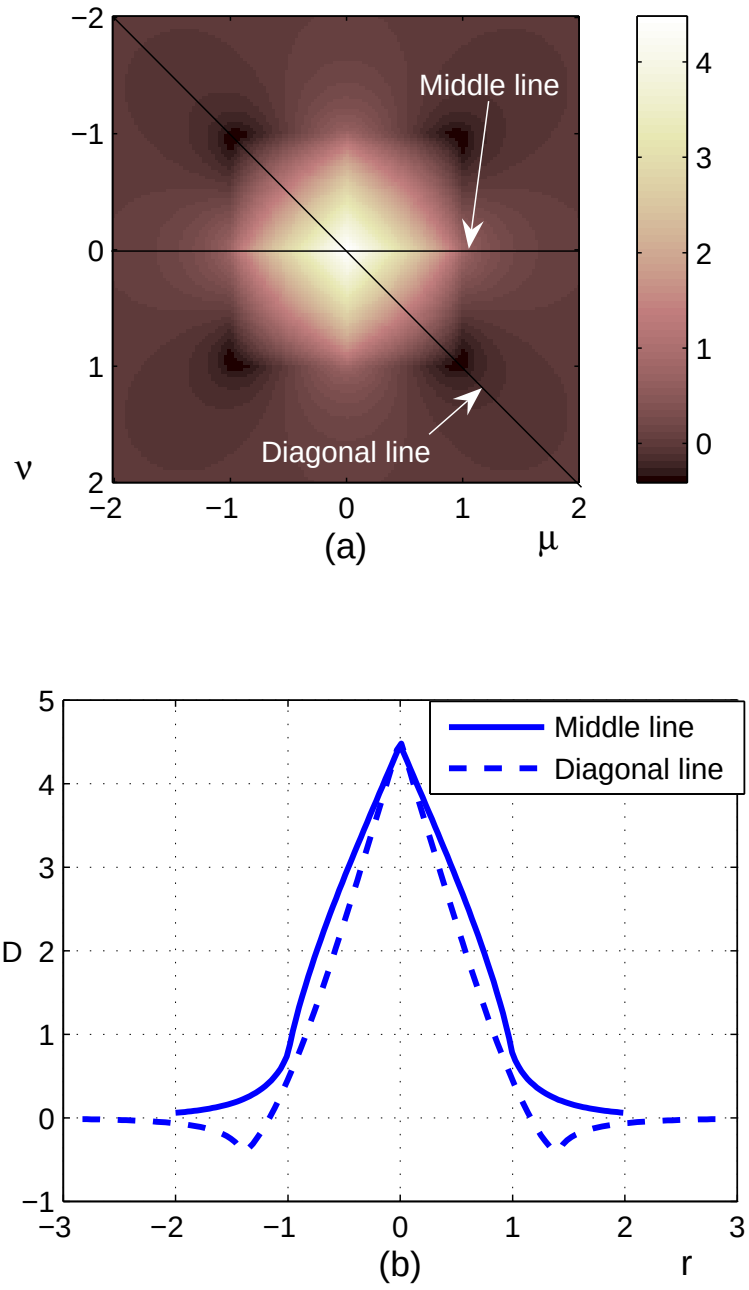

Figure 3.2: Circulation D for a canonical vortex. A top view of D is shown in (a) as a function of the relative position of the vortex inside the four subaperture area, shown in Fig. 3.1, for $-2 < \mu < 2$ and $-2 < \nu < 2$. One-dimensional functions of D are plotted as functions of $r = \sqrt{\mu^2 + \nu^2}$ in (b) along the 'diagonal line' and 'middle line,' respectively, as indicated in (a).

where $|\mu|, |\nu| = 1$, the circulation function forms negatively valued peaks with the value

$$D = \frac{\pi}{2} - 2\ln(5) - 2\arctan(2) + 5\ln(2) = -0.396641. \tag{3.11}$$

It can be seen that the circulation function never becomes exactly zero when the vortex is far away from the centre of the four subapertures, which implies that the existence of a vortex at some point in the output plane gives nonzero circulation values in all other parts of the output plane.

In view of the fact that the peak value of the circulation function is $\pi + 2\ln(2)$ instead of 2π, it is interesting to note that, if the four sample values of $D^{m,n}$ closest to the location of a vortex – i.e. the four values that surround the vortex – are added up then the result is closer to 2π.

3.3.2 Noncanonical vortex

Optical vortices in strongly scintillated beams are in general noncanonical. It is therefore necessary to know how the computation of the circulation is affected by the morphology of the vortex. The phase function of a vortex with an arbitrary morphology is given by Eq. (3.1). The gradient of this phase function can be expressed by

$$\nabla\phi(x, y) = \frac{(x\hat{y} - y\hat{x})C}{x^2(1 + A) - 2yxB + y^2(1 - A)}, \tag{3.12}$$

where

$$A = \sin(\alpha)\cos(\beta), \tag{3.13}$$

$$B = \sin(\alpha)\sin(\beta), \tag{3.14}$$

$$C = \cos(\alpha), \tag{3.15}$$

with the morphology angles α and β, as defined in Eqs. (2.25) and (2.26). The vortex can be translated to any location (x_0, y_0) by replacing $x \to x - x_0, y \to y - y_0$ in Eq. (3.12).

The same procedure that was used in Subsection 3.3.1 is used to analyze the noncanonical case. According to Eq. (2.14), the output of the Shack-Hartmann wavefront sensor is computed for the phase gradient given in Eq. (3.12), shifted to (x_0, y_0). Then the result is substituted into Eq. (3.6) to compute the circulation D. Here the general expression is provided for the circulation, Eq. (3.6), of the sampled average slope $\mathbf{G}$, Eq. (2.14), obtained as output from the Shack-Hartmann wavefront sensor when the input is the phase

function of a noncanonical vortex with arbitrary morphology angles α and β, located at an arbitrary point (in normalized coordinate $\mu = x_0/w$ and $\nu = y_0/w$) within the four subapertures shown in Fig. 3.1,

$$\begin{aligned}
D^{m,n} \;=\; & \frac{\mu_p(A_m - B)}{2A_m}\arctan\left[\frac{\mu_p B - \nu_m A_m}{\mu_p C}\right] - \frac{\mu_p(A_m + B)}{2A_m}\arctan\left[\frac{\mu_p B - \nu_p A_m}{\mu_p C}\right] \\
& + \frac{\mu_m(A_m + B)}{2A_m}\arctan\left[\frac{\mu_m B - \nu_m A_m}{\mu_m C}\right] - \frac{\mu_m(A_m - B)}{2A_m}\arctan\left[\frac{\mu_m B - \nu_p A_m}{\mu_m C}\right] \\
& + \frac{\nu_p(A_p - B)}{2A_p}\arctan\left[\frac{\nu_p B - \mu_m A_p}{\nu_p C}\right] - \frac{\nu_p(A_p + B)}{2A_p}\arctan\left[\frac{\nu_p B - \mu_p A_p}{\nu_p C}\right] \\
& + \frac{\nu_m(A_p + B)}{2A_p}\arctan\left[\frac{\nu_m B - \mu_m A_p}{\nu_m C}\right] - \frac{\nu_m(A_p - B)}{2A_p}\arctan\left[\frac{\nu_m B - \mu_p A_p}{\nu_m C}\right] \\
& - \frac{\mu_p B}{A_m}\arctan\left[\frac{\nu A_m - \mu_p B}{\mu_p C}\right] + \frac{\mu_m B}{A_m}\arctan\left[\frac{\nu A_m - \mu_m B}{\mu_m C}\right] \\
& - \frac{\nu_p B}{A_p}\arctan\left[\frac{\mu A_p - \nu_p B}{\nu_p C}\right] + \frac{\nu_m B}{A_p}\arctan\left[\frac{\mu A_p - \nu_m B}{\nu_m C}\right] \\
& + \mu\arctan\left[\frac{\mu B - \nu_p A_m}{\mu C}\right] - \mu\arctan\left[\frac{\mu B - \nu_m A_m}{\mu C}\right] \\
& + \nu\arctan\left[\frac{\nu B - \mu_p A_p}{\nu C}\right] - \nu\arctan\left[\frac{\nu B - \mu_m A_p}{\nu C}\right] \\
& + \frac{\mu_p C}{4A_m}\ln\frac{\left(2\mu_p\nu_m B - \mu_p^2 A_p - \nu_m^2 A_m\right)\left(2\mu_p\nu_p B - \mu_p^2 A_p - \nu_p^2 A_m\right)}{\left(2\mu_p\nu B - \mu_p^2 A_p - \nu^2 A_m\right)^2} \\
& - \frac{\mu_m C}{4A_m}\ln\frac{\left(2\mu_m\nu_p B - \mu_m^2 A_p - \nu_p^2 A_m\right)\left(2\mu_m\nu_m B - \mu_m^2 A_p - \nu_m^2 A_m\right)}{\left(2\mu_m\nu B - \mu_m^2 A_p - \nu^2 A_m\right)^2} \\
& + \frac{\nu_p C}{4A_p}\ln\frac{\left(2\mu_p\nu_p B - \mu_p^2 A_p - \nu_p^2 A_m\right)\left(2\mu_m\nu_p B - \mu_m^2 A_p - \nu_p^2 A_m\right)}{\left(2\mu\nu_p B - \mu^2 A_p - \nu_p^2 A_m\right)^2} \\
& - \frac{\nu_m C}{4A_p}\ln\frac{\left(2\mu_m\nu_m B - \mu_m^2 A_p - \nu_m^2 A_m\right)\left(2\mu_p\nu_m B - \mu_p^2 A_p - \nu_m^2 A_m\right)}{\left(2\mu\nu_m B - \mu^2 A_p - \nu_m^2 A_m\right)^2},
\end{aligned} \tag{3.16}$$

where $\mu_p = \mu + 1$, $\mu_m = \mu - 1$, $\nu_p = \nu + 1$, $\nu_m = \nu - 1$, $A_p = 1 + A$ and $A_m = 1 - A$, with A, B and C as defined in Eqs. (3.13)-(3.15).

Figure 3.3 shows the peak value at $(\mu, \nu) = (0, 0)$ for D as a function of the morphology angles α and β. Note that the peak is positive (negative) for $0 \leq \alpha < \pi/2$ ($\pi/2 < \alpha \leq \pi$). At $\alpha = \pi/2$ there is a discrete jump, which represents the change in the topological charge of the vortex. The fact that there is such a large difference between the values on either side of the jump indicates that the circulation D, calculated from the output of the Shack-Hartmann wavefront sensor, can in principle determine the topological charge of a vortex even if it is severely anisotropic. However, in a practical situation, optical vortices tend to have such severe anisotropic morphologies only when they appear in oppositely charged pairs close to each other. In such situations their circulation values will in general partially cancel each other, making them difficult to identify. Near the jump at $\alpha = \pi/2$

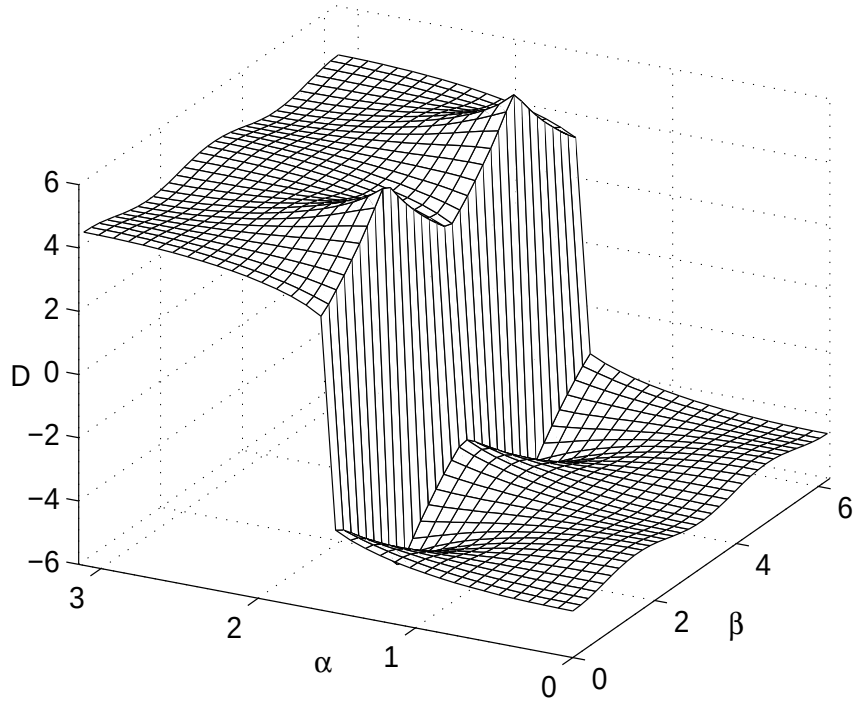

Figure 3.3: Peak value of circulation D as a function of the morphology angles $0 < \alpha < \pi$ and $0 < \beta < 2\pi$. The jump at $\alpha = \pi/2$ is due to the change in the topological charge of the vortex.

the value of D has its greatest fluctuation as a function of β. Next to the jump, D fluctuates between π and 2π. When α approaches the canonical values of 0 or π the value of D tends towards its canonical peak value of 4.53 and the fluctuations as a function of β diminish.

In Figs. 3.4 and 3.5 it is shown the plots of D over the region $-2 < \mu < 2$ and $-2 < \nu < 2$, for two different morphologies of the vortex. First the case when $\alpha = \pi/4$ and $\beta = \pi$ is considered. This represents a vortex with a moderate anisotropy oriented along the y-axis. The top view of the circulation function for this case is shown in Fig. 3.4(a) and the precise shape of the circulation function is shown in Fig. 3.4(b) in terms of three one-dimensional functions: along $\nu = 0$ (μ-line), along $\mu = 0$ (ν-line) and along the line where $\nu = \mu$ (diagonal line). The peak value at the origin is about 4.5. The function then decreases toward zero away from the origin. It is noted that the shape of the circulation function is more anisotropic than the shape in Fig. 3.2 in that the respective widths of the peak along the μ- and ν-directions are not equal. There are still regions where the function becomes negative.

Next the case where $\alpha = 4\pi/9$ and $\beta = \pi/2$ is considered. This represents a highly

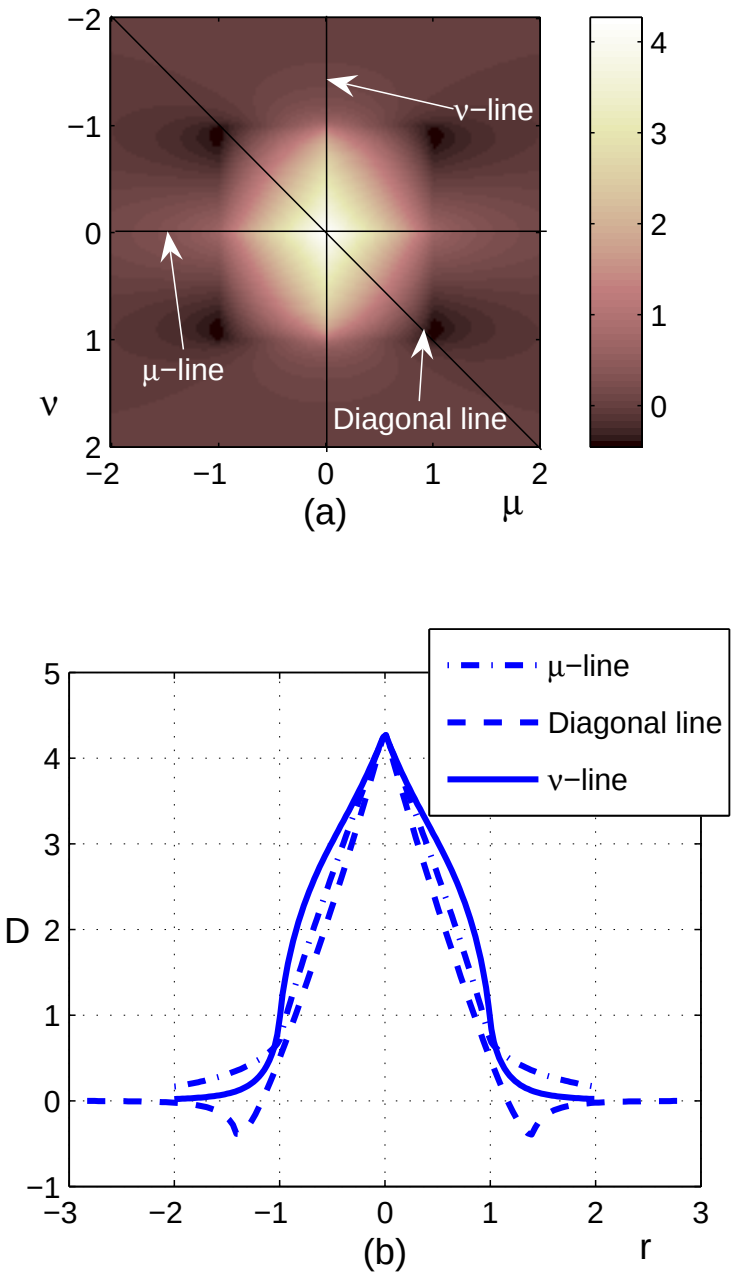

Figure 3.4: Circulation D for a noncanonical vortex, with $\alpha = \pi/4$ and $\beta = \pi$. A top view of D is shown in (a) as a function of the relative position of the vortex inside the four subaperture area, shown in Fig. 3.1, for $-2 < \mu < 2$ and $-2 < \nu < 2$. One-dimensional functions of D are plotted as functions of $r = \sqrt{\mu^2 + \nu^2}$ in (b) along the 'diagonal line', 'μ-line' and 'ν-line,' respectively, as indicated in (a).

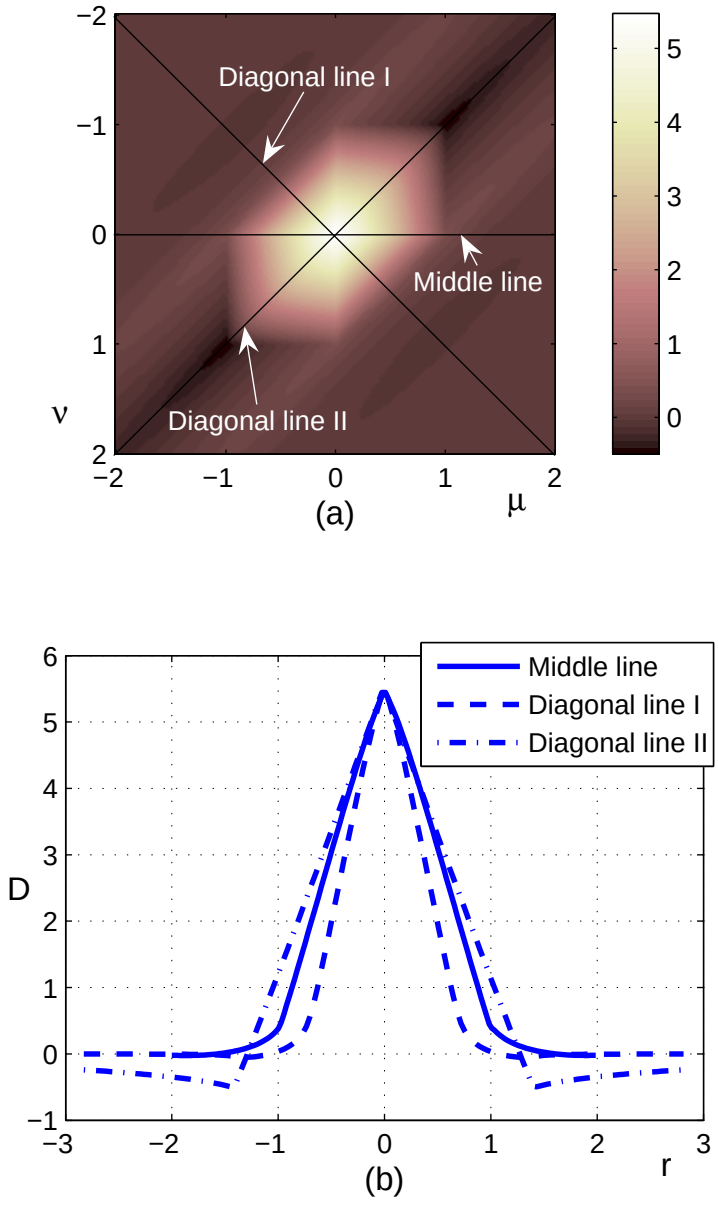

Figure 3.5: Circulation D for a noncanonical vortex, with $\alpha = 4\pi/9$ and $\beta = \pi/2$. A topview of D is shown in (a) as a function of the relative position of the vortex inside the four subaperture area, shown in Fig. 3.1, for $-2 < \mu < 2$ and $-2 < \nu < 2$. One-dimensional functions of D are plotted as functions of $r = \sqrt{\mu^2 + \nu^2}$ in (b) along the 'diagonal line I' (perpendicular to the orientation of the vortex), 'diagonal line II' (along the orientation of the vortex) and 'middle line,' respectively, as indicated in (a).

anisotropic vortex oriented diagonally along the line where $\nu = -\mu$. The top view of the circulation function for this case is shown in Fig. 3.5(a) and the precise shape of the circulation function is shown in Fig. 3.5(b) in terms of three one-dimensional functions: along $\nu = 0$ (middle line), along the line where $\nu = \mu$ (diagonal-I line) and along the line where $\nu = -\mu$ (diagonal-II line). The peak value at the origin is now about 5. The function decreases away from the origin, but the decrease is much slower along the orientation of the vortex. The shape of the circulation function is therefore much more anisotropic.

3.4 Numerical investigation

3.4.1 Vortex detection in a scintillated beam

Here a numerical simulation is provided to test the vortex detection procedure that was analytically investigated in the previous sections. A Gaussian beam with wavelength $\lambda = 987$ nm is simulated to propagate over a distance of $L = 100$ km through a turbulent atmosphere. The layered model of propagation described in Section 2.2 is used to perform this simulation. The strength of the turbulence is parameterized with the structure constant of the index of refractive fluctuations $C_n^2 = 4 \times 10^{-18}$ m$^{-2/3}$. Ten equally spaced phase screens are used to simulate this optical path. Each phase screen simulates a turbulent atmosphere layer with a thickness of $\Delta z = 10$ km and possesses a von Kámán spectrum, as in Eq. (2.2), with a turbulence outer scale of $L_0 = 100$ m. Here, the Rytov variance and Fried parameter can be calculated by Eq. (2.9) and Eq. (2.11). In this simulation,

$$\begin{aligned} \delta_{\chi,R}^2 &= 0.124 k^{7/6} L^{11/6} C_n^2 \approx 0.063, \\ r_0 &= 0.331 \left(\frac{\lambda^2}{L C_n^2} \right)^{3/5} \approx 56 \text{ cm}. \end{aligned} \tag{3.17}$$

The subaperture size of the Shack-Hartmann wavefront sensor is set as $w = 4$ cm. Therefore, the ratio of subaperture size to the Fried parameter is about 0.07. For a Shack-Hartmann wavefront sensor with a given subaperture size, this ratio indicates the strength of the turbulence in the optical path. The relative error of image centroid measurements associated with scintillations is no more than 4% if a physical Shack-Hartmann wavefront sensor works with the ratio of 0.07 in a practical AO system [96]. When the ratio of subaperture size to the Fried parameter is less than 0.25 in a uniform distribution of the strength of turbulence, a Shack-Hartmann wavefront sensor can achieve a good estima-

tion accuracy [25]. Therefore, the results obtained from the numerical simulations have reasonable agreement with practice.

All the phase screens and propagation are conducted on an $N \times N$ array with a sampling space of $\Delta = 1$ cm. To avoid the aliasing problems caused by using FFT in numerical simulations, the relationship between the array size N along one direction of the FFT array, the sampling space Δ and the propagation distance should satisfy [101]

$$N \geq \frac{2\lambda\Delta z}{\Delta^2}. \tag{3.18}$$

The same relationship in the other direction can be deducted if the same sampling space is used in both directions. It can be proven through Eq. (3.18) that calculation with a 256×256 array is satisfactory. This numerical method provides reasonable agreement between real world data and simulation data.

The phase of the beam may be distorted when it reaches the system aperture and in this example four optical vortices are found in the wavefront, as shown in Fig. 3.6(a). Central 80×80 circular area of the 256×256 array is viewed as the system aperture in this simulation. This beam then passes through the simulated Shack-Hartmann wavefront sensor, from which a sampled vector field $\mathbf{G}$ can be computed with Eq. (2.14). The circulation function D is then computed with Eq. (3.6). The resulting circulation function is shown in Fig. 3.6(b). Two of the vortices, one positive and one negative, are easily identified from their respective circulation values of 2.95 and -3.54, in the lower left corner of Fig. 3.6(a). Note that the magnitudes of both these values are smaller than 2π. This would be due to a combination of the fact that the vortices have noncanonical morphologies, the fact that they are not located at the ideal location in the centre of the four subapertures and noise that is present in the phase function. By integrating over a 3×3 neighborhood around these vortices, circulation values of 6.20 and -5.86 can be obtained, respectively, which are closer to $\pm 2\pi$.

The other two oppositely charged vortices in the upper right corner of Fig. 3.6(a) are much closer to each other. Therefore, their individual circulation functions overlap and, having opposite topological charges, they partially cancel each other. As a result the circulation peaks that represent these vortices are severely diminished. For example, the positive peak for this pair of vortices in Fig. 3.6(b) has a value of only 1.41. Oppositely charged vortices that are located closer to each other are therefore more difficult to detect.

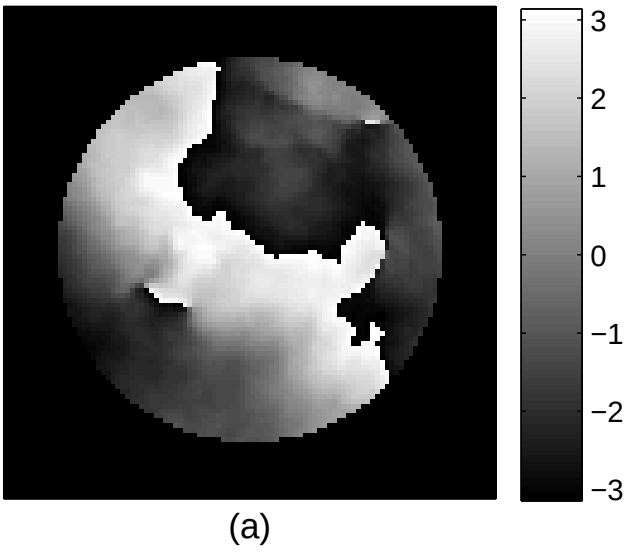

(a)

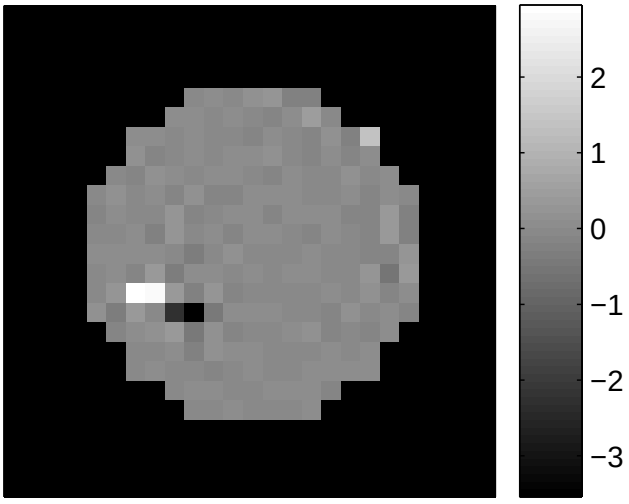

(b)

Figure 3.6: Numerical simulation results for a Gaussian beam propagated over a distance of 100 km through a turbulent atmosphere. The resulting phase of the beam inside the system aperture is shown in (a). There are two pairs of oppositely charged phase singularities. The pairs are, respectively, located at the lower left and the upper right of the system aperture. Circulation D, numerically calculated from the output of the Shack-Hartmann wavefront sensor, is shown in (b).

3.4.2 Noise circulations

From Fig. 3.6(b), it can be seen that the circulation value is not zero even if there are no vortices inside or near the subaperture. This nonzero circulation is referred to as noise circulation. It is caused by the phase fluctuations inside the subapertures. The circulation peak of the vortices may be submerged in the noise circulations, which will severely degrade the detection abilities of a Shack-Hartmann wavefront sensor due to false vortices being detected from noise circulations. In this section, numerical simulations are implemented to investigate the effects of the noise circulation.

Here, phase screens are generated to simulate turbulent atmosphere layers with the same parameters used in the previous Section 3.4.1 but different values of C_n^2 are used to simulate different conditions of turbulence in the optical path. the Fried parameters can be calculated for each C_n^2 with Eq. (2.11). Therefore, the ratio of subaperture size w to the Fried parameter r_0 can also be calculated. A wave field with only one positive vortex passes through such a phase screen and as a result phase fluctuations arise in the wave field. To avoid the complexity and focus on the noise circulations just after the phase screen, it is assumed that this vortex is canonical and located at the centre of the four subapertures in a Shack-Hartmann wavefront sensor.

In each simulation, circulations are calculated in the same way for each grid with Eq. (3.6). Noise circulations are also calculated in the same manner with Eq. (3.6) over every four subapertures where no vortices are inside or near these subapertures. Maximal noise circulation in each simulation is selected for statistics. At the same time, the sum of circulations for each 3×3 grids around the vortex are also calculated. The circulation D in each grid only depends on the vortex position and topological charge. However, the sum of the circulations over an area of the 3×3 grids around a vortex will approximate to 2π. It seems that this sum of circulations depends on how many grids included but its upper limit is 2π, i.e., this sum of circulations will be exact 2π if there are only one vortex with included area is infinite. The statistical results of the circulations as functions of the ratio of subaperture size w to the Fried parameter r_0 are shown in Fig. 3.7. The expectation values of the vortex circulation, the sum of 3×3 vortex circulation and the maximal noise circulations are shown by circles, triangles and diamonds respectively. Their associated standard deviations are shown by error bars.

It can be seen that the expectation value of the vortex circulation is about 4.52, which is consistent with the analytical result in Eq. (3.9). It seems that the vortex circulation remains unchanged when the ratio of w/r_0 increases, which means that vortex circulation

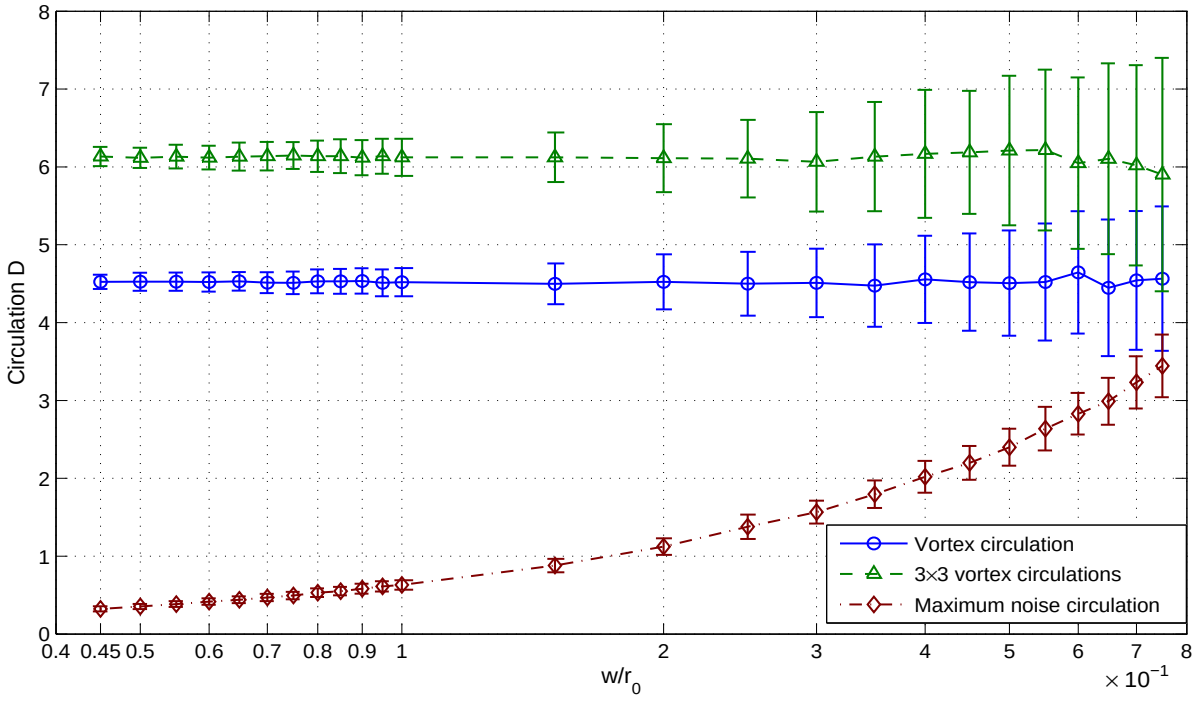

Figure 3.7: Circulations of vortex and noise as functions of the ratio of subaperture size w to the Fried parameter r_0. The circles show the expectation values of the vortex circulation. The diamonds show the expectation values of the maximal noise circulation. The triangles show the expectation values of a sum of vortex circulations over 3×3 subapertures around the vortex circulation peak. The error bars are their associated standard deviations.

is not sensitive to the phase fluctuations for a Shack-Hartmann wavefront sensor with a given subaperture size. It would benefit from the averaging process in the Shack-Hartmann vortex detection procedure. At the same time, the expectation value of the sum of 3×3 vortex circulations is about 6.1 (2π). It also remains unchanged when the ratio of w/r_0 becomes large. Therefore, stable vortex circulation peaks can be obtained in vortex detection with a Shack-Hartmann wavefront sensor.

In Fig. 3.7, it is shown that noise circulation increases with the increment of w/r_0. Hence, vortex circulations may be submerged in the noise circulations when the ratio of w/r_0 is very large. As a result, false vortices will be detected at the locations where the noise circulations are greater than the threshold of vortex circulation for vortex detection. In these simulated circumstances, the circulations of a vortex and noise begin to overlap each other when $w/r_0 > 0.7$. It means that false vortices will be detected when $w/r_0 > 0.7$. Here, only the results when the vortex is canonical and located at the centre of the four subapertures and the relationship between the noise circulation and the ratio of w/r_0 are provided. As discussed in previous sections, it is noted that the vortex circulation will drop down when it is noncanonical or located inside the subaperture. These influences on vortex circulation will be discussed in the next chapter.

3.5 Conclusion

The phase gradient that is produced as the output of a Shack-Hartmann wavefront sensor contains information about the continuous phase function of the incident wave, but also of the optical vortices in the wavefront. A least-squares projector [27–30] can be used to extract information about the continuous phase and can be used to correct continuous phase distortions. The information about the vortices is contained in the solenoidal part of the phase gradient. The curl of this part gives a topological charge distribution, which represents the locations and topological charges of the optical vortices. Theoretically each positive (negative) vortex should be indicated by a value of 2π (-2π) in the topological charge distribution.

The averaging process inherent to the Shack-Hartmann wavefront sensor has a significant effect on the computed topological charge distribution. Instead of the theoretical value of 2π, the actual value that is produced is at most about 4.53. The precise location of the vortex relative to the subapertures in the Shack-Hartmann wavefront sensor, as well as the morphology of the vortex, produce further variations in the value of the topological charge distribution at the location of a vortex. Nevertheless, these values are

generally large enough to identify an isolated vortex. It is therefore possible to extract the information of the location and topological charge of the vortices from the output obtained from a Shack-Hartmann wavefront sensor.

In the analytical investigation presented here only one vortex is considered. In the numerical simulation it is found that when different oppositely charged vortices are in close proximity to each other, their respective topological charge distributions, as produced by the circulation computations, would overlap, causing partial cancellation and a subsequent reduction in their peaks. This cancellation effect makes detection of these vortices more difficult. Further investigation will be done to understand the effect of multiple vortices located near each other on the detection process in the next chapter.

The phase functions of scintillated optical beams are in general noisy. The phase fluctuations in the wavefront sensor subaperture causes non-zero circulations when there is no vortex near the subaperture, which is referred to as noise circulation. This noise circulation may increase with the increment of the ratio of subaperture size w to the Fried parameter r_0. Simple numerical investigations with only one canonical vortex are provided. It is shown that the ability of detecting optical vortices deteriorates as noise circulation increases.

Here, the measurement errors, such as the readout noise and shot noise of CCD, in the Shack-Hartmann wavefront sensor are not considered. In practical implementation, these errors may affect the wavefront measurement and subsequently affect the detection of vortices.

Chapter 4

Dipole influence on Shack-Hartmann vortex detection

4.1 Introduction

In a strongly scintillated beam, there are generally numerous optical vortices. Adjacent vortices have a high probability of being of opposite charge [41]. Vortices will be created and annihilated in pairs during beam propagation. As described in Chapter 3, a Shack-Hartmann wavefront sensor can be used to detect optical vortices that appear in an optical beam after it has propagated over a long distance through a turbulent atmosphere. However, the evolution of the vortex morphology during beam propagation and the influence of nearby oppositely charged vortices adversely affect the Shack-Hartmann vortex detection process. In fact, the morphology evolution of two oppositely charged vortices during beam propagation is much more complicated than that of two vortices with the same charge [98]. This makes vortex detection complicated. At the same time, when two oppositely charged vortices approach each other, the cancellation effect makes vortex detection more difficult. The influence of the morphology and of the separation distance between oppositely charged vortices on Shack-Hartmann vortex detection is studied to determine the conditions for reliable vortex detection.

In this chapter, the influence of vortex morphology and the cancellation effect on vortex detection with a Shack-Hartmann wavefront sensor will be investigated, to extend the previous work on single vortex detection, which is described in Chapter 3. The influences of the vortex morphology evolution and the separation distance on vortex detection will be separately investigated in Subsections 4.2.1 and 4.2.2 respectively. Then, the combined

influence of vortex morphology and separation distance is considered for dipole detection in a Gaussian beam in Subsection 4.2.3. It is shown that the cancellation effect dominates over other parameters in Shack-Hartmann vortex detection when vortices are close to each other. In Section 4.3, numerical simulation results for vortex detection in strongly scintillated beams are provided. The statistical curves of vortex circulation as a function of separation distance are similar to the curves for a Gaussian beam with only one dipole. Conclusions are provided in Section 4.4.

4.2 Influences of dipole on vortex detection in a Gaussian beam

From Eq. (2.14), it can be seen that the Shack-Hartmann wavefront sensor measures the local average phase gradient inside each subaperture. Since the phase function contains the contributions of vortices embedded in the optical field, the phase profile of each vortex will influence the output of the Shack-Hartmann wavefront sensor. Hence, the output of the wavefront sensor is indirectly influenced by the morphologies of the vortices, as well as the distance between the vortices. Therefore, both the vortex morphology and the vortex separation distance need to be taken into consideration for Shack-Hartmann vortex detection.

To simplify the problems, the influence of one dipole that is embedded in a Gaussian beam on Shack-Hartmann vortex detection needs to be investigated. At this point, it needs to determine whether the main influence of the vortices on the detection is the vortex morphology or the separation distance between two vortices. Therefore, separate analyses of these two aspects will be provided below, and then, their combined influence in a Gaussian beam will be investigated. As defined in Subsection 2.4.2, the normalized transverse coordinates (u, v, t) are used for convenience in the following calculations.

4.2.1 Morphology

In random wave fields, the morphologies of optical vortices obey their probability density functions and the expectation value of anisotropy $\cos\alpha$ is $2/3$ and the vortex orientation angle is uniformly distributed in 0 and 2π (see Appendix B). However, as discussed for the vortex dipole in a Gaussian beam and in scintillated beams in Appendix C, the morphology of an optical vortex does not remain unchanged during beam propagation.

When a vortex dipole approaches an annihilation point (the discriminant $\mathcal{D} \to 0$ and the vortex separation distance approaches zero), the vortex anisotropy $\cos\alpha$ reduces to zero and both vortices become edge dislocations with their relative orientation in alignment. The vortex itself is squeezed severely when another oppositely charged vortex approaches it. Therefore, it needs to understand the influence of vortex morphologies on the Shack-Hartmann vortex detection.

From the trajectories of the vortices in Eqs. (2.32) and (2.33), the vortex separation distance d can be expressed as a function of the propagation distance t, given by

$$d(t) = \sqrt{[u_1(t) - u_2(t)]^2 + [v_1(t) - v_2(t)]^2} = \sqrt{\frac{\mathcal{D}}{\beta^2 \Delta u^2 + a^2}}. \tag{4.1}$$

The dipole will be created or annihilated at the points where $\mathcal{D} = 0$. Both $\mathcal{D}$ and d go smoothly to zero at such a critical point.

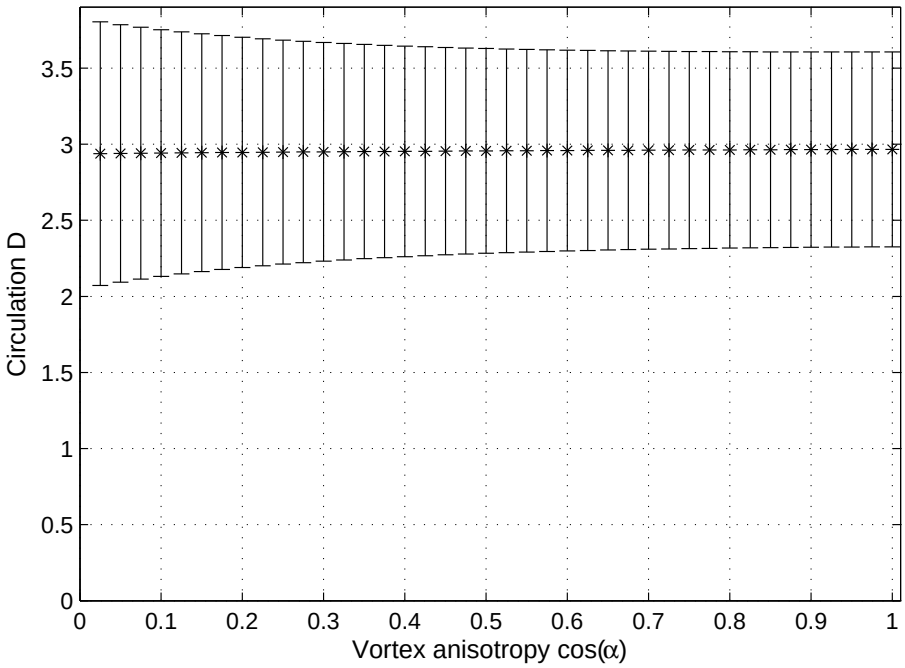

Figure 4.1: Vortex circulation D as a function of vortex anisotropy, $\cos(\alpha)$. The stars show the expectation values for all possible vortex locations inside the subaperture. Error bars show the associated standard deviations.

The circulation D can be calculated as a function of the vortex anisotropy by integrating the circulation when the vortex is located inside the subaperture [102] and its orientation is uniformly distributed between 0 to 2π [45]. In this subsection, all circulations are calculated for a single vortex with a given anisotropy to avoid the influence of the circulations of other vortices. All possible vortex morphologies have been considered for this single vortex.

Figure 4.1 shows circulation D as a function of the vortex anisotropy $\cos\alpha$, from a canonical vortex ($\cos\alpha = 1$) to an edge dislocation ($\cos\alpha = 0$). This mimics the vortex morphology evolution as the vortex approaches an annihilation point. The origin of the horizontal axis is the point where the vortex becomes an edge dislocation as it would be annihilated by an oppositely charged vortex. In Fig. 4.1 the expectation value of D remains almost unchanged when the vortex approaches an edge dislocation. The error bars show the associated standard deviations as the vortex is randomly located inside a subaperture with a uniformly distributed orientation. From Fig. 4.1 it can be seen that the morphology evolution of a vortex has very little influence on the circulation, which means it does not significantly reduce the detection ability of a Shack-Hartmann wavefront sensor during beam propagation.

4.2.2 Separation distance

The separation distance between two oppositely charged vortices gradually reduces to zero during beam propagation before they annihilate each other. The topological charge distribution of these two vortices may overlap and cancel each other when they are very close. To see how this cancellation affects the vortex detection process, the separation distance can be can varied while keeping the vortices canonical, thus ignoring the vortex morphology evolution.

First, one special case is considered for a positive vortex located at the origin, which is the centre of the four subapertures. Another negative vortex is located at $(d, 0)$. Therefore, the beam prefactor with these two optical vortices can simply be expressed as

$$P(u, v) = (u + iv)(u - d - iv), \tag{4.2}$$

where d is the separation distance between two vortices. The output of the Shack-Hartmann wavefront sensor can be calculated by substituting the gradient of the phase function of Eq. (4.2) into Eq. (2.14). The result is then substituted to Eq. (3.6) to calculate the vortex circulation, which can be expressed as

$$\begin{aligned} D \;=\; & 2\ln(2) + \frac{\pi}{2} + \frac{d+w}{w}\ln(w+d) + \frac{d}{w}\arctan\left(\frac{d-w}{w}\right) - \ln(d-w) \\ & + \frac{d-2w}{2w}\ln[(d+w)^2 + w^2] + \frac{d-2w}{2w}\ln[(d-w)^2 + w^2] \\ & - \frac{2d}{w}\arctan\left(\frac{d}{w}\right) + \ln(w^2 + d^2) + \frac{\pi d}{2w} - \frac{d}{w}\arctan\left(\frac{w}{w+d}\right) \\ & - \frac{d-2w}{2w}\ln(d-w)^2 + \frac{\pi\,\mathrm{sign}(d-w)}{2} + \frac{1}{w}\begin{cases} \pi(d - iw) & d < w \\ 0 & \text{elsewhere} \end{cases}, \end{aligned} \tag{4.3}$$

where sign(·) denotes the sign of the argument and w is the Shack-Hartmann subaperture size.

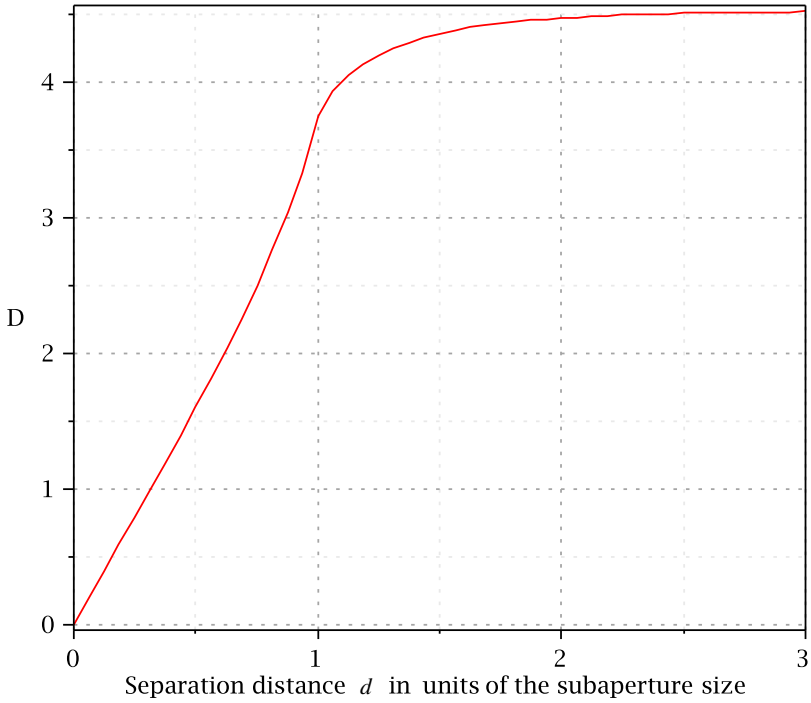

Figure 4.2: Circulation D of the positive vortex as a function of vortex separation distance when two vortices are assumed to be canonical and approach each other in a horizontal direction.

The graph in Fig. 4.2 shows the relationship between the circulation and the vortex separation distance when the vortex is located at the centre of the four subapertures. In this figure, the horizontal axis shows the distance between two vortices in units of the subaperture size w. It can be seen that the circulation value quickly drops down to zero when the separation distance is smaller than one subaperture size. The circulation value is also saturated at about 4.53, which is the peak circulation value for one single vortex as described in Chapter 3, when the separation distance is larger than 1.5 times the subaperture size. It indicates that the cancellation effect can be ignored when the separation distance is larger than 1.5 times the subaperture size. It is shown in Fig. 4.2 that a strong cancellation effect exists when two oppositely charged vortices approach each other.

The relationship between the circulation and the vortex separation distance as in Eq. (4.3) is analytically obtained for this special case where one positive vortex is located at the centre of the four subapertures. Similarly, all analytical expressions of circulation D can be obtained as functions of vortex separation distance for other cases, in which the vortex can be randomly located inside the subaperture and the oppositely charged

vortex approaches it in a random direction. To consider all of these situations, the beam prefactor is modified by expressing it simply as a product of two oppositely charged canonical vortices while setting one vortex at the origin, which is the centre of the four subapertures, expressed as

$$P(u,v) = (u+iv)\left[u - d\cos(\rho) - i(v - d\sin(\rho))\right], \tag{4.4}$$

where ρ is the relative angle between the connecting line of two vortices and the u axis and d is the vortex separation distance.

Here, only the detection for a positive vortex is considered, as it would be the same for the negative one. The relative approaching angle between the vortices can be any value in $[0, 2\pi)$ in the random wave field. To simulate situations where the vortex is randomly located inside the subaperture, the integration areas of those four subapertures are shifted while keeping the beam prefactor in Eq. (4.4) unchanged. Therefore, the circulation for the vortex can be directly calculated from this beam prefactor without propagating the beam. The circulation D can be obtained as a function of the vortex separation distance, by integrating the circulation when the vortex is located inside the subaperture and ρ is uniformly distributed between 0 and 2π. For any given vortex separation distance, the vortex is set to be canonical to avoid the influence of circulation due to morphology.

The graph in Fig. 4.3 shows the relationship between the circulation and the separation distance when another oppositely charged vortex approaches from different directions. The origin of the horizontal axis represents the point where the vortex is annihilated by an oppositely charged canonical vortex. In this figure, the expectation value of the circulation D saturates at about 2.9 when the vortex separation distance is larger than 1.5 times the subaperture size. It quickly drops down to zero when the two vortices approach and annihilate each other. Hence, although the influence from other vortices can be ignored when the vortex separation distance is larger than 1.5 times the subaperture size, the cancellation effect is very strong when two oppositely charged vortices are very close to each other. The error bars indicate the standard deviation in circulation as the vortex is randomly located inside a subaperture and the other vortex approaches from a different direction. Comparing Fig. 4.3 with Fig. 4.1, it can be seen that the separation distance dominates the circulation reduction before the vortex is annihilated. Figure 4.3 also indicates that, when two oppositely charged vortices are very close to each other, the cancellation effect of the topological charge distribution will make Shack-Hartmann vortex detection virtually impossible.

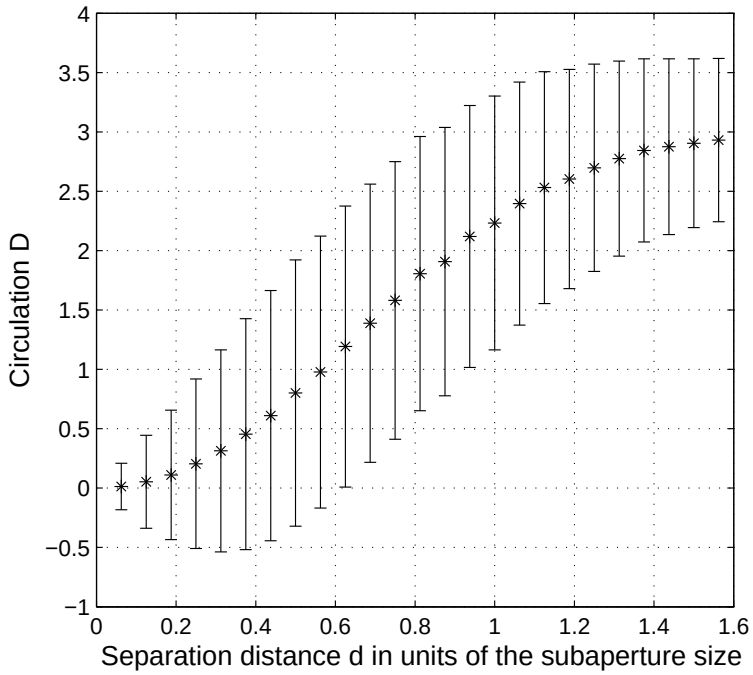

Figure 4.3: Vortex circulation D as a function of the separation distance d when both vortices in a dipole are assumed to remain canonical. The stars show the expectation value of D for all possible vortex locations inside the subaperture. Error bars show the associated standard deviations.

4.2.3 Vortex dipole in a Gaussian beam

Now the combined effects of the vortex separation distance and morphology evolution on the Shack-Hartmann vortex detection will be discussed. For this purpose a canonically launched vortex dipole propagating in a Gaussian beam is considered.

As shown in Fig. 4.4, once the position (u_1, v_1) of one of the vortices (here it is referred to the positive one) has been decided, the position (u_2, v_2) of the other one can be determined from the separation distance d and the relative angle ρ between the connecting line of two vortices and the u axis. The vortex can be located at any point inside the subaperture with equal probability. If it is assumed that, initially, the two oppositely charged vortices of a dipole are symmetrically located at $[d\cos(\rho)/2, d\sin(\rho)/2]$ and $[-d\cos(\rho)/2, -d\sin(\rho)/2]$, then the beam prefactor in the launch plane ($t = t_0$) can be expressed by

$$\begin{aligned} P(u, v, t_0) &= \left[\left(u - \frac{d\cos(\rho)}{2}\right) + i\left(v - \frac{d\sin(\rho)}{2}\right)\right] \\ &\quad \times \left[\left(u + \frac{d\cos(\rho)}{2}\right) - i\left(v + \frac{d\sin(\rho)}{2}\right)\right]. \end{aligned} \tag{4.5}$$

With Fresnel diffraction, the expression for the beam prefactor can be obtained at any

arbitrary propagation distance t,

$$P(u,v,t) = 1 - \frac{d^2}{4} + \frac{id(v\cos(\rho) - u\sin(\rho)) - 1}{(1-it)} + \frac{u^2+v^2}{(1-it)^2}. \tag{4.6}$$

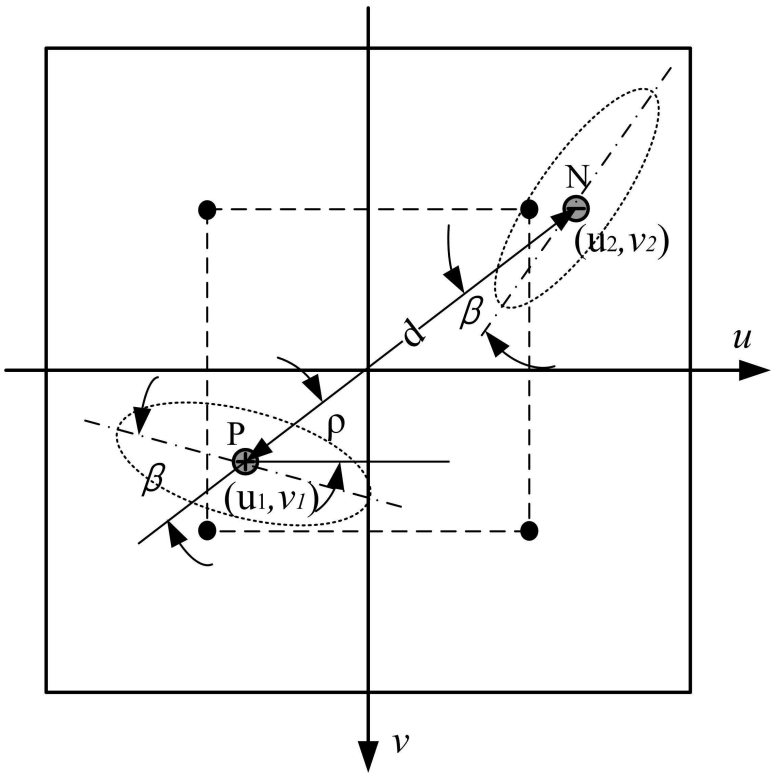

Figure 4.4: Dipole relative position in the Shack-Hartmann wavefront sensor subapertures. The four subapertures are represented by the four squares. Circled plus and circled minus denote the positive vortex located at $P(u_1, v_1)$ and negative vortex located at $N(u_2, v_2)$ respectively. The relative position between two vortices can be expressed by the distance d and approaching angle ρ. Two dotted ellipses respectively represent the anisotropy of the two vortices with relative orientation angle β.

By substituting Eq. (4.6) into Eq. (2.14), the theoretical outputs of a Shack-Hartmann wavefront sensor can be obtained. The results can then be substituted into Eq. (3.6) to calculate the circulation D. Numerical methods are employed to perform these calculations.

The procedure is as follows. On each transverse beam plane along the direction of propagation, Eq. (2.27) can be numerically applied to the phase gradient of the beam prefactor in Eq. (4.6) to find the locations of the vortices. The separation distance $d(t)$ and the approaching angle ρ between the two vortices can be calculated from the vortex

locations. Ideally, ρ would remain unchanged when d decreases prior to dipole annihilation. Only the cases where the positive vortex is located inside the dash lines in Fig. 4.4 are considered to evaluate the circulation (the same would apply for the negative vortex). For these cases, Eq. (2.14) is numerically integrated over four neighboring subapertures and the results are substituted into Eq. (3.6) to calculate the circulation D. This gives the vortex distribution in the subaperture on the upper left-hand side.

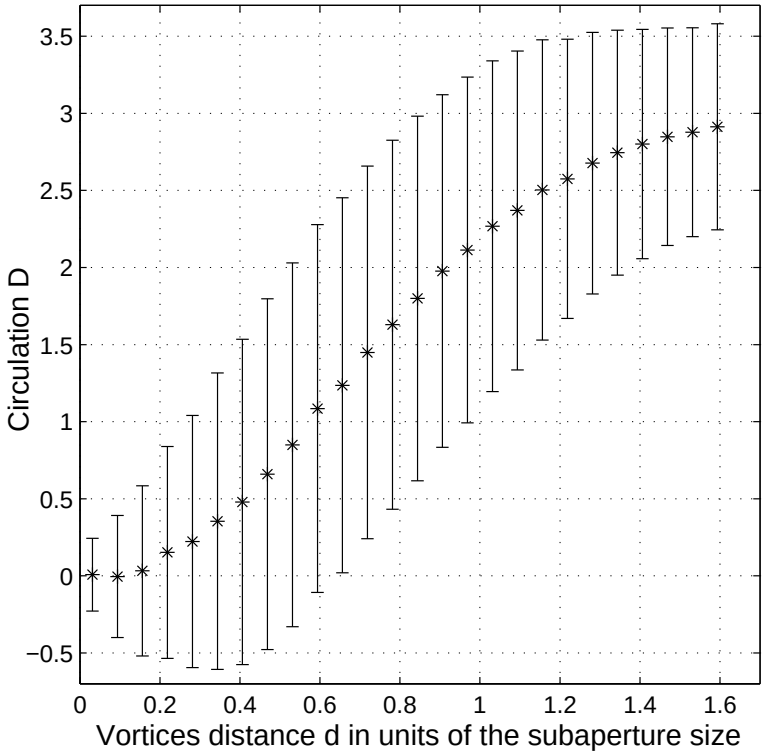

Figure 4.5: Vortex circulation D as a function of the separation distance d when a dipole is embedded in a free-space propagating Gaussian beam. The stars show the expectation value for all possible vortex locations inside the subaperture. Error bars show the associated standard deviations.

The graph in Fig. 4.5 shows the statistical values of D as a function of d. The expectation values are shown by stars and their associated standard deviations are shown by error bars. Comparing Fig. 4.5 with Fig. 4.3, it can be seen that the curves are very similar, which indicates that the influence of the separation distance is dominant, while the influence of the morphology is insignificant. The expectation value of D approaches zero when d approaches zero due to the cancellation effects between two vortices. The expectation value is also saturated at about 2.9 when the vortex separation distance is larger than 1.5 times the subaperture size, which agrees with the value obtained in Fig. 4.3. It means that the cancellation effect from the negative vortex can be ignored for separation distances larger than 1.5 times the subaperture size.

4.3 Numerical simulations

Numerical simulations of strongly scintillated beams containing optical vortices are used to test the above analysis. In these simulations, a plane wave with wavelength $\lambda = 500$ nm propagates through a turbulent atmosphere over a distance of $L = 15$ km. The strength of the turbulence is parameterized by the atmospheric refractive-index structure constant: $C_n^2 = 2 \times 10^{-17}$ m$^{-2/3}$. Therefore, the Rytov invariance and Fried parameter are,

$$\begin{aligned} \sigma_{\chi,R}^2 &= 0.307 k^{7/6} L^{11/6} C_n^2 = 0.053, \\ r_0 &= 0.185 \left(\frac{\lambda^2}{L C_n^2} \right)^{3/5} \approx 16.6 \text{ cm}. \end{aligned} \tag{4.7}$$

This 15 km turbulent atmosphere is simulated by 15 random phase screens as in the layered model described in Section 2.2. Each phase screen simulates an atmosphere layer with a thickness of $\Delta z = 1$ km and possesses the von Kámán spectrum, as in Eq. 2.2, with a turbulence outer scale of $L_0 = 100$ m. Because the beam propagation is conducted on an $N \times N$ array with the FFT algorithm, the numerical array size N, the sampling space Δ, the phase screen separation distance and the wave length λ must satisfy $N \geq (2\lambda\Delta z)/\Delta^2$, as in Eq. (3.18). Here, the sampling space is set as $\Delta = 1$ mm. Then, the array size must satisfy $N \geq 1000$. Therefore, the wave field can be represented by a 1024×1024 numerical array in the beam propagation procedure. The Shack-Hartmann wavefront sensor subaperture is modelled by a square with a size of $w = 0.8$ cm. The ratio of subaperture size to the Fried parameter r_0 is about 0.048, with which the results obtained from numerical simulations will have reasonable agreement with practice [25, 96].

Under these conditions, optical vortices are generally created in the target plane. An example of such a scintillated beam is shown in Fig. 4.6. In this figure, it can be seen that numerous optical vortices are present in the receiver aperture after the beam has propagated through a turbulent atmosphere over such a long distance. In these simulations, only vortex dipoles where the two oppositely charged vortices are separated by less than $2w$ and all other vortices are further than $2w$ away from them, are taken into consideration. A separation distance of $2w$ is chosen because the circulation distribution of one vortex can be ignored beyond an area of 2×2 subapertures.

The vortex locations are numerically obtained from the gradient of the phase function with Eq. (2.27). The separation distance d is numerically calculated from the vortex locations of each dipole. At the same time, the circulation distribution is calculated over the four subapertures that contain the positive vortex of each dipole. These four

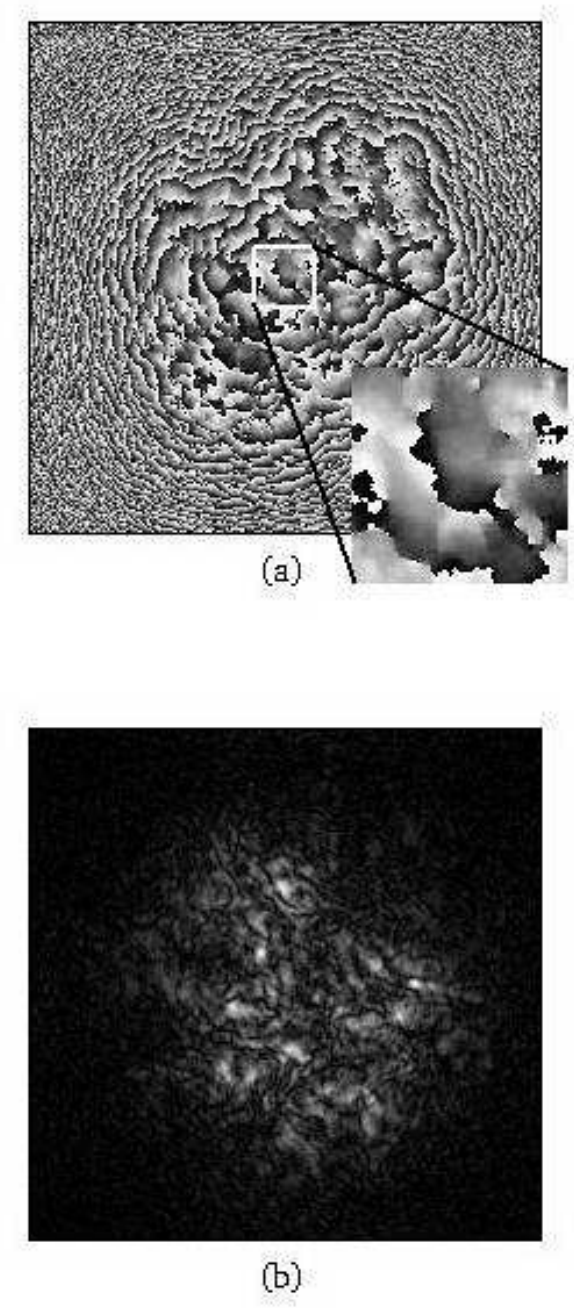

Figure 4.6: Phase (a) and amplitude (b) of an optical field in the receiver aperture after a beam has propagated through turbulent atmosphere over a distance of 15 km. Central 256 × 256 area of the 1024 × 1024 array are shown in these figures. The phase in the small white rectangle in (a) blows up to show the vortices clearly.

subapertures are purposely shifted so that all possible circulations can be calculated as if the positive vortex was randomly located inside the subaperture.

The simulation is performed repeatedly to obtain a large number of samples (6810 dipoles). The statistical results for circulation D as a function of separation distance d are shown in Fig. 4.7. The stars show the expectation values of D with their standard deviations shown as error bars. For comparison, the expectation values of D for the noiseless conditions in a Gaussian beam are also shown by dots in Fig. 4.7. It can be seen that the relation between D and d is very similar to the noiseless case in a Gaussian beam as shown in Fig. 4.5. Accordingly, the same conclusions can be drawn for dipole detection in strongly scintillated beams as for the previous noiseless case in Section 4.2.3. It seems that the circulation of a vortex is not dominated by the noise in the phase function but by the vortex separation distance, due to the averaging process in Eq. (2.14). Therefore, it can be argued that similar curves for the circulation D can be obtained as a function of vortex separation distance under conditions of different turbulent strength.

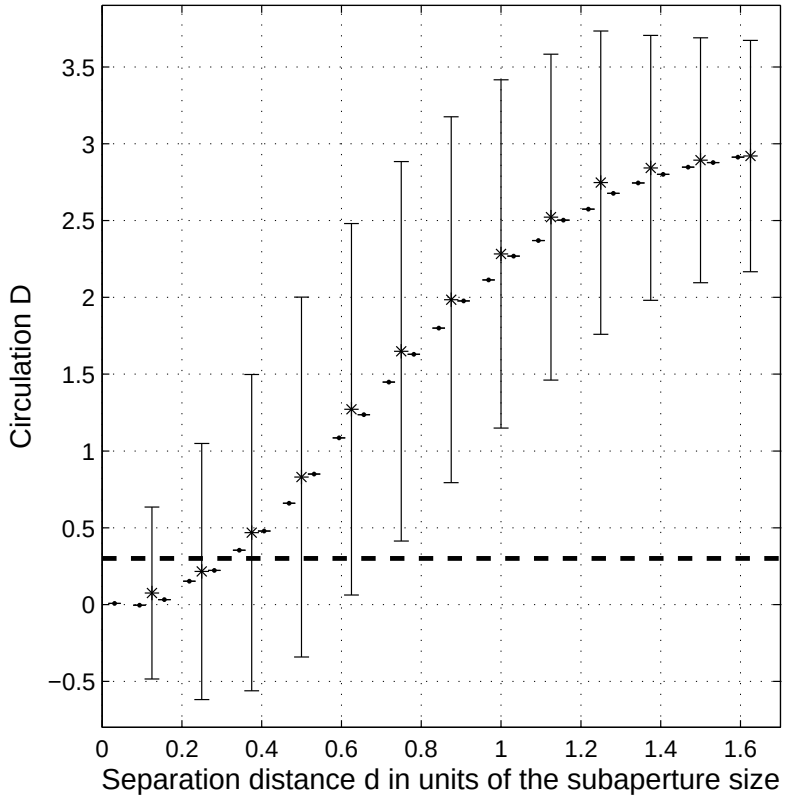

Figure 4.7: Circulation D as a function of separation distance d. The stars show the expectation value for all possible vortex locations inside the subaperture. Error bars show the standard deviations. The dots are the same expectation values shown in Fig. 4.5 for comparison. The horizontal dashed line represents the maximal noise circulation (0.3).

As discussed in subsection 3.4.2, owing to the noise fluctuations in the phase function, the circulation is not zero where no vortices are inside or near the four subapertures, which is referred to as noise circulation. As the dashed line shown in Fig. 4.7, the maximal noise circulation is about 0.3 for the ratio of w/r_0 used here in simulations is 0.048. If a threshold of vortex circulation is set at 0.5 for vortex detection, all of the vortices can be detected when their separation distance is larger than $0.8w$ in simulations. Therefore, in a condition with a given value of the ratio of w/r_0, the detecting ability of a Shack-Hartmann wavefront sensor is mainly decided by the vortex separation distance.

It is noted that the variations of noise circulation depend on the ratio of w/r_0 as shown in Fig. 3.7. The noise circulation increases as the strength of turbulence becomes strong for a Shack-Hartmann wavefront sensor with a given subaperture size. The threshold of vortex circulation have to be increased to detect optical vortices by that given Shack-Hartmann wavefront sensor when the noise circulation increases. Hence, the vortex separation distance of those vortices, which can be detected by that given Shack-Hartmann wavefront sensor, will increase owing to the increment of turbulent strength. It means that the vortex detection ability of that given Shack-Hartmann wavefront sensor is reduced as the strength of turbulence increases.

In practice, a Shack-Hartmann wavefront sensor with small subapertures, which means reducing the ratio of w/r_0, can be used to detect vortices with small separation distances. However, as shown in Fig. 4.7, the expectation value of vortex circulation is saturated at about 2.9 with its lower level of standard deviations being about 2.2, when the vortex separation distance is larger than 1.5 times the subaperture size. When the noise circulation is larger than 2.2, the vortex circulation will be overlapped with the noise circulation, even if the vortices are far away from each other or the subaperture size of the Shack-Hartmann wavefront sensor is small enough. A threshold of vortex circulation cannot be set to detect vortices anymore. Therefore, the noise circulation caused by atmospheric turbulence puts an upper limit of the vortex detection ability of a Shack-Hartmann wavefront sensor.

4.4 Conclusion

During Shack-Hartmann vortex detection, the distribution of circulation values for positive and negative vortices will cancel one another when these two vortices are very close to each other. This cancellation effect is especially strong when the two vortices in a dipole are separated by fewer than two subaperture sizes. The value of vortex circulation D is also influenced by the vortex morphology and relative position of the vortices inside

the sensor subaperture. However, it seems that Shack-Hartmann vortex detection is not sensitive to morphology evolution during beam propagation. Our analysis shows that the circulation is mainly decided by the vortex separation distance.

When the two vortices are separated by a distance larger than two subaperture sizes, the expected circulation D is about 2.9, which does not depend on the strength of turbulence and is large enough for vortex detection. In numerical simulations, with the ratio of w/r_0 being 0.048, the Shack-Hartmann wavefront sensor cannot be used to detect the dipoles when the separation distance is smaller than 0.8 times subaperture size due to the noise circulations which have already been discussed in the Subsection 3.4.2. Optical vortices which are separated by a smaller physical distance can only be detected by a Shack-Hartmann wavefront sensor with higher resolutions. However, the reduction in subaperture size may cause other problems, such as a low sensor signal-noise-ratio. It is also noted that noise circulation, which depends on the strength of atmospheric turbulence, influences the vortex detection ability of a Shack-Hartmann wavefront sensor.

Chapter 5

Accelerating the annihilation of an optical vortex dipole

5.1 Introduction

When a Gaussian beam with two oppositely charged vortices propagates in free space, these two vortices will move around on the transverse beam plane. They may either move together and annihilate each other spontaneously or survive all the way, depending on the conditions. It was found that there are two main factors that cause the lateral movement of an optical vortex, the intensity gradient and the phase gradient, which are produced by other vortices and by the background beam at the vortex core [78,79]. These are successful in explaining the linear motion for a vortex soliton [103, 104] and the rotation between two vortices with the same topological charge [80]. However, if this hypothesis was also correct for the vortex dipole, it would arrive at the incorrect conclusion that two vortices should shift in the same transverse direction while retaining their separation distance, and therefore would never annihilate each other. As a matter of fact, the vortices in a dipole will annihilate each other or move away from each other during beam propagation. Actually, it cannot merely be focused on the phase or intensity gradient at the vortex core when dealing with vortex dipoles, because two oppositely charged vortices will affect each other during beam propagation. For this reason, it is very difficult to control dipole annihilation by only manipulating local parameters. In a given light beam, the intrinsic parameters of each vortex and the vortex distribution are fixed and difficult to adjust with deformable mirrors. Therefore, vortex manipulation in a light beam through control of the outside parameters, such as the background phase, is the only option open to us,

and is investigated in this chapter.

Optical vortices may be removed from a light beam by forcing them to annihilate in pairs. Since the lateral vortex motion is partly determined by the background phase, it would be believed that an appropriate background phase function can be used to force a vortex dipole to annihilate. However, it is obvious that new vortices will be created if this background phase function is similar to a random phase screen. Other types of background phases, such as the spherical, cylindrical or wedge-typed phase surface, show the poor ability to forcing a dipole in a strongly scintillated beam to annihilate. Therefore, an arbitrary choice of a background phase function is often more likely to produce additional vortices instead of getting rid of them. So to find out what an appropriate background phase function should be like, the background phase function near the vortex dipole annihilation point is investigated. To simplify the problems, it is considered for a canonically launched vortex dipole in a Gaussian beam propagating in free space. The background phase function created by these two oppositely charged vortices that will annihilate each other is investigated. In the case of vortex dipole annihilation, it is assumed that this background phase function has the potential to force two oppositely charged vortices to move towards each other and annihilate each other. However, it is difficult to separate this background phase function from the vortex-bearing optical field. Instead the background phase function on the transverse beam plane just after the plane where a vortex dipole annihilated is used. it can be argued that this phase function still retains the potential of forcing two vortices to move towards each other because of the small changes in background phase profile before and after a dipole annihilation. It also has a continuous phase profile, which can in principle be implemented by deformable mirrors. It is shown by numerical simulations that vortex dipole annihilation is accelerated by using this background phase function.

The remainder of this chapter is organized as follows: The background phase created by the coupling effects between two oppositely charged vortices is extracted by a numerical method in Section 5.2. It is found that the background phase function after a dipole annihilation retains the potential to force two oppositely charged vortices to annihilate each other. In Section 5.3 a procedure is described that how to apply this background phase function to accelerate the dipole annihilation in a Gaussian beam. Numerical simulations provided in Section 5.4 show that this kind of background phase has the ability to accelerate vortex dipole annihilation. Conclusions are provided in Section 5.5.

5.2 Background phase extraction

In general, the complex amplitude function, $E(u, v, t)$, of a Gaussian beam with optical vortices on a transverse plane at t can be expressed in normalized coordinates as

$$E(u, v, t) = P(u, v, t)E_g(u, v, t), \tag{5.1}$$

where

$$E_g(u, v, t) = \exp\left(-\frac{u^2 + v^2}{1 - it}\right), \tag{5.2}$$

is the pure Gaussian beam and $P(u, v, t)$ is a complex bivariate polynomial beam prefactor of finite order, which contains optical vortices. The beam prefactor can be expressed as

$$P(u, v, t) = |P|\, e^{j\theta(u,v)}, \tag{5.3}$$

in terms of the amplitude $|P|$, and the phase function $\theta(u, v)$ as the sum of a continuous phase function $\theta_c(u, v)$ and an arbitrary number of optical vortices $\Phi(u-u_n, v-v_n; \alpha_n, \beta_n)$, as in Eq. (2.40).

It is difficult in practice to extract the background phase analytically from a Gaussian beam with a vortex dipole, especially to extract the background phase in a beam with several dipoles. Therefore this extraction procedure is implemented numerically.

For a Gaussian beam with a canonically launched dipole, the locations of optical vortices, (u_1, v_1) and (u_2, v_2), can be calculated according to Eqs. (2.32) and (2.33), and their morphology angles, (α_1, β_1) and (α_2, β_2), according to Eqs. (2.38) and (2.39) on any arbitrary transverse beam plane at $t = t_1$.

If the initial parameters of a Gaussian beam are not known, numerical methods can be used to obtain the vortex locations and morphology angles. On the beam transverse plane at propagation distance t_1, a closed line integral of the gradient of the phase function of the optical field, as in Eq. (2.27), can be numerically applied to locate the vortices on the transverse plane [26, 105]. The locations of the vortices, (u_j, v_j), are indicated where the integral has a nonzero value. In practical optical systems, a Shack-Hartmann wavefront sensor may be used to locate the vortices in the Gaussian beam as described in Chapter 3. The vortex morphology angles, (α_j, β_j), at (u_j, v_j), can also be directly calculated from the complex amplitude of the optical field according to Eqs. (2.35) and (2.36). Using Eq. (2.24), together with these vortex locations and morphologies, a vortex field V_d can

be constructed as the product of all vortices, given by

$$\begin{aligned} V_d &= \frac{1}{2}\left[(\xi_1+\zeta_1)(u-u_1)+i(\xi_1-\zeta_1)(v-v_1)\right] \\ &\quad\times\left[(\xi_2+\zeta_2)(u-u_2)+i(\xi_2-\zeta_2)(v-v_2)\right]\cdots \\ &\quad\times\left[(\xi_j+\zeta_j)(u-u_j)+i(\xi_j-\zeta_j)(v-v_j)\right]\cdots, \end{aligned} \tag{5.4}$$

where (ξ_j, ζ_j) are expressed in terms of α_j and β_j as in Eqs. (2.25) and (2.26), with $j = 1, 2, \cdots$.

According to Eq. (5.1), the background phase function at $t = t_1$ can be extracted as

$$\theta_{bg} = \arg\left\{\frac{E_{t1}}{E_g V_d}\right\}, \tag{5.5}$$

where $\arg\{\cdot\}$ denotes the phase of the argument; V_d is given in Eq. (5.4); E_{t1} is the complex amplitude function of the polynomial Gaussian beam on the transverse plane of t_1; and E_g is a pure Gaussian beam, given in Eq. (5.2), at $t = t1$.

As predicted by the vortex trajectories in Eqs. (2.32) and (2.33), the vortex dipole embedded in its background phase, θ_{bg}, annihilates after a relatively short distance of propagation. Figure 5.1 shows the phase functions of a Gaussian beam before and after a vortex dipole annihilation. In Fig. 5.1(a) it shows the phase function of a Gaussian beam with two oppositely charged vortices just before the dipole is annihilated. These two vortices are very close to each other. In this figure, they are located at the end of the short black line with their separation distance being the same with the length of the black line. This phase function is discontinuous due to the presence of vortices. A continuous background phase function can be extracted from this Gaussian beam before the dipole annihilation using Eq.(5.5). The result is shown in Fig. 5.1(b). In the case of vortex dipole annihilation, it can be assumed that this background phase function prior to vortex dipole annihilation contains the potential to force two oppositely charged vortices to move toward each other. This background phase function can be applied to force a vortex dipole to annihilate, because it is continuous and can thus in principle be implemented by a deformable mirror in an AO system. However, it is very difficult to find the exact locations and morphologies of the vortices in a beam owing to the finite resolution that appears in the extraction procedure. Residual phase errors may be retained in the extracted background phase function, which can subsequently produce additional vortices during propagation.

After the vortex dipole annihilation, the phase function will become smooth and continuous, as shown in Fig. 5.1(c). The background phase function, as shown in Fig. 5.1(d), can be extracted from the Gaussian beam by removing E_g only. This background phase

function is similar to the background phase function shown in Fig. 5.1(b), except for the black strip. The reason for the similarity between these two background phase functions is that the phase function changes gradually with propagation distance. Hence, it can be argued that this background phase function after the vortex dipole annihilation still retains the potential to force two oppositely charged vortices to move toward each other, as before dipole annihilation. Therefore, this continuous background phase function found behind a dipole annihilation point can be applied to accelerate the annihilation of two oppositely charged vortices in a Gaussian beam.

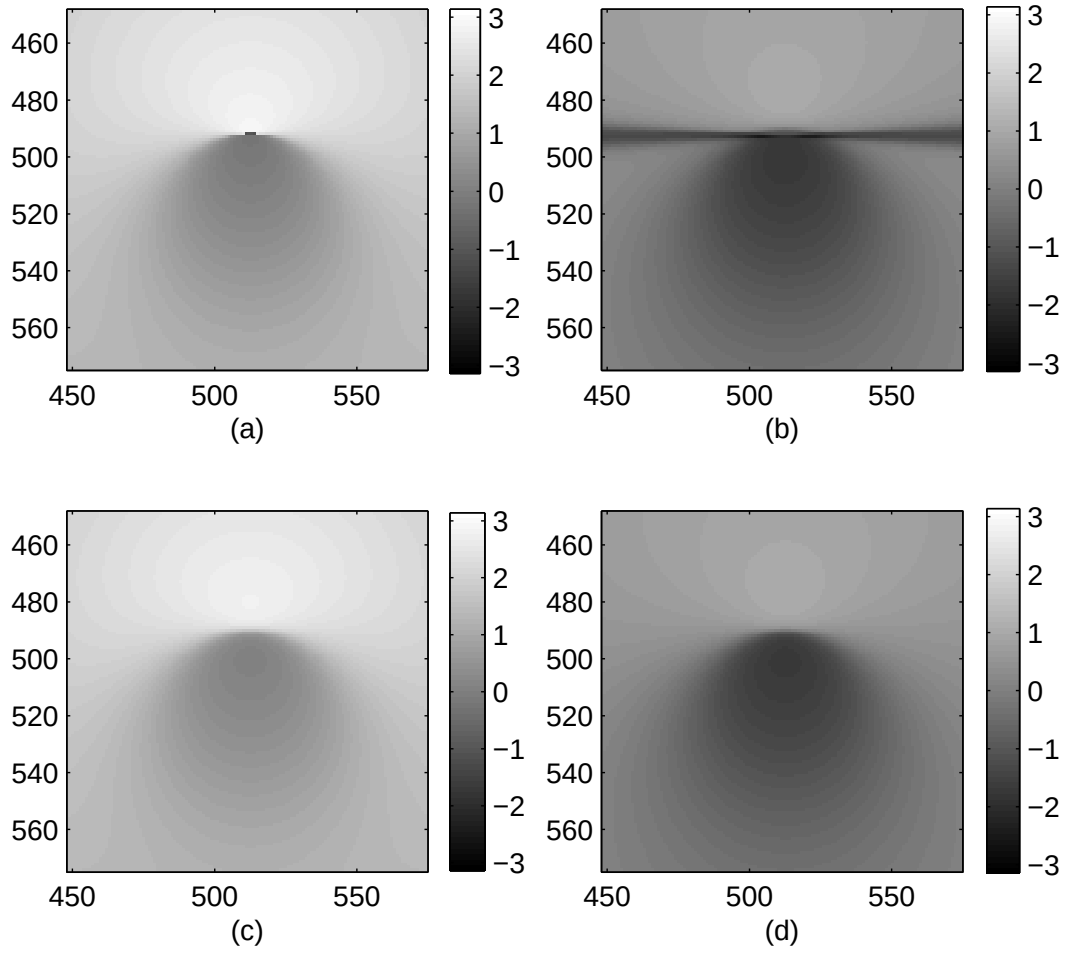

Figure 5.1: Phase functions of a Gaussian beam before and after a vortex dipole annihilation. Figure (a) shows the phase function with two oppositely charge optical vortices, which are located at the ends of the short black line. Figure (b) shows the background phase function extracted from the phase function in Figure (a). Figure (c) shows the continuous phase function after the dipole annihilation. Figure (d) shows the background phase function extracted from the phase function in Figure (c).

The advantage of using the latter background phase function is that no residual errors will be introduced as there is no need to calculate vortex locations and morphologies during this background phase extraction. A three-dimensional view of the background phase function that is extracted after the dipole annihilation is also shown in Fig. 5.2. This background phase function is not asymmetric because the phase function prior to the annihilation is not asymmetric due to the dipole. It can be seen that this phase function is smooth and continuous without any vortices, although the gradient of this background phase function is still steep in the area where the dipole annihilated. Moreover, the background phase function may become smoother as it propagates beyond the dipole annihilation point. It can be assumed that the gradient of this continuous background phase function is not too large and that it can in principle be approximated by a deformable mirror. If this were not the case a phase function further behind the annihilation point could be used, provided that it does not go so far that the acceleration process does not work anymore. The relationship between the phase smoothness and the distance behind the dipole annihilation point and how this affects the acceleration of the annihilation process are issues for further study and will not be discussed in this thesis.

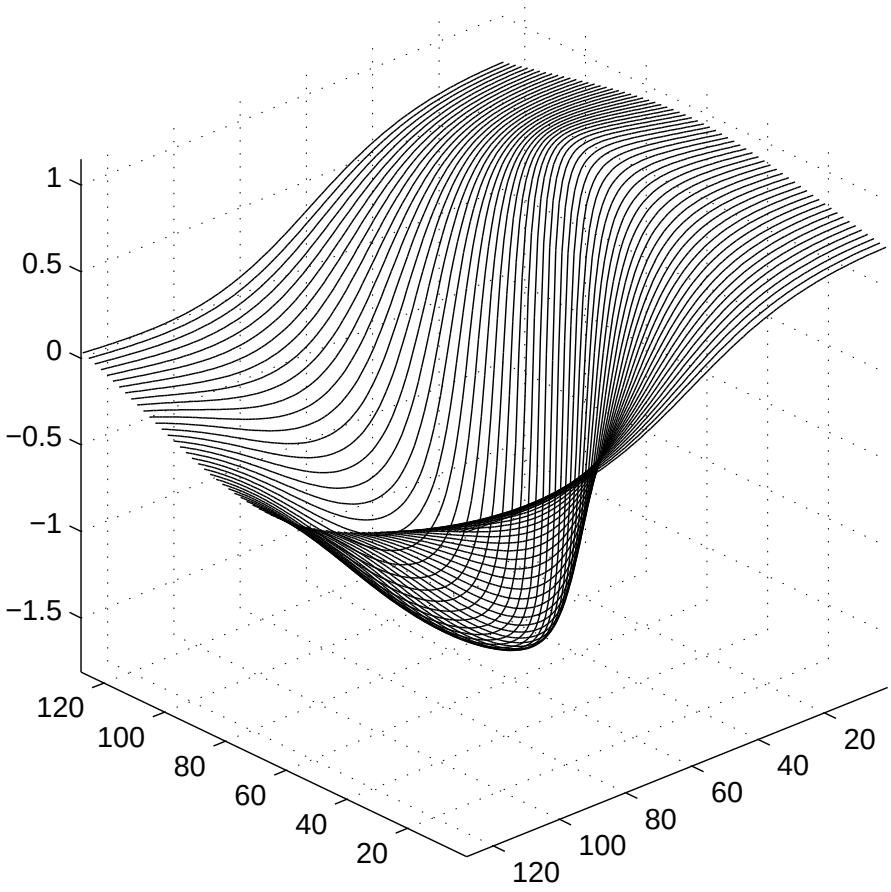

Figure 5.2: A three-dimensional view of the background phase function after a vortex dipole annihilation.

5.3 Accelerate dipole annihilation with a background phase

Here a procedure is described that how to accelerate the annihilation of a vortex dipole in an arbitrary beam, G, with a background phase created according to the locations of the vortices. Figure 5.3(a) shows the amplitude profile of a vortex-bearing Gaussian beam, as an example for the subsequent discussion of this procedure. This beam is represented by an array of 1024×1024 pixels with pixel size $\Delta = 10\ um$. The beam waist size is $\omega_0 = 640\ \mu$m and the wavelength is $\lambda = 1\ \mu$m. Two oppositely charged vortices are arbitrarily located at $(u_1, v_1) = (5/16, 5/16)$ and $(u_2, v_2) = (-15/32, -5/32)$. The separation distance between the two vortices is $d = 0.91$.

Once the vortex locations, (u_1, v_1) and (u_2, v_2), have been obtained, the vortex separation distance d and the dipole angle ρ, relative to the horizontal axis, can be calculated from these locations. Using this information, a Gaussian distribution, G_0, can then be generated, in the waist of the beam with two oppositely charged canonical vortices, located symmetrically on opposite sides of the beam centre. This is expressed as

$$G_0 = \left[u + iv + \frac{d}{2}\exp(i\rho))\right]\left[u - iv - \frac{d}{2}\exp(-i\rho)\right]\exp(-u^2 - v^2). \tag{5.6}$$

According to the vortex trajectory functions in Eqs. (2.32) and (2.33), the propagation distance t_a and the location (u_a, v_a) where two vortices in G_0 annihilate each other can be theoretically calculated. These are given by

$$t_a = \frac{d^2}{2\sqrt{1-d^2}}, \tag{5.7}$$

$$u_a = \frac{d(d^2-2)\sin(\rho)}{4\sqrt{1-d^2}}, \tag{5.8}$$

$$v_a = \frac{d(d^2-2)\cos(\rho)}{4\sqrt{1-d^2}}. \tag{5.9}$$

It follows from Eqs. (5.7-5.9) that a condition for dipole annihilation is that the normalized vortex separation distance must satisfy $d < 1$. In this example, for the Gaussian beam created from vortex locations, $(u_1, v_1) = (5/16, 5/16)$ and $(u_2, v_2) = (-15/32, -5/32)$, it is obtained that $t_a = 1$ and $(u_a, v_a) = (0.33, -0.55)$.

This Gaussian beam in Eq. (5.6) can now propagate over a distance of $t_a + \delta$, where δ is a small propagation distance compared to t_a, and produce a distribution, G_a, without vortices. Then, a continuous background phase function, θ_a, can be obtained by only

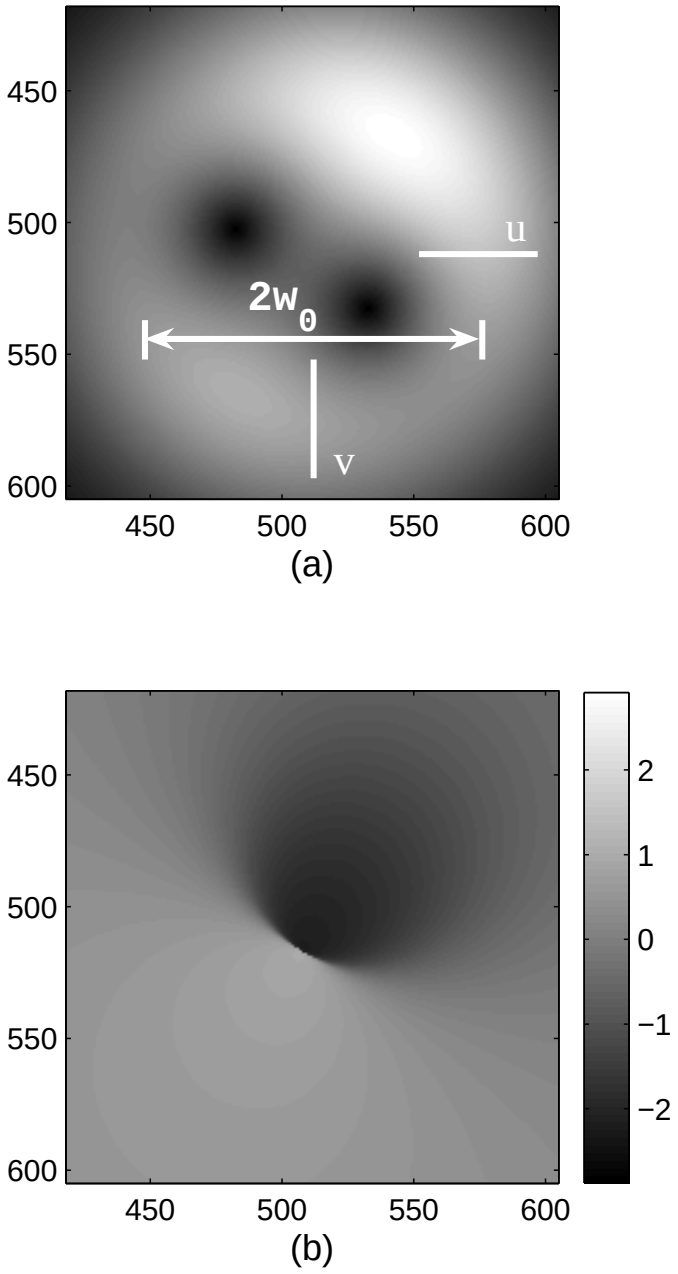

Figure 5.3: Figure (a) shows the amplitude of a Gaussian beam with two oppositely charged vortices, shown as two dark cores, separated by a distance of $d = 0.91$. The Gaussian beam waist size is $\omega_0 = 640$ μm. Figure (b) shows a background phase function created according to the locations of the vortices in Figure (a).

removing the pure Gaussian beam and extracting the phase,

$$\theta_a = \arg\left\{G_a \exp\left(\frac{u^2+v^2}{1-it_a}\right)\right\}. \tag{5.10}$$

Next, the phase function θ_a is shifted to the location of the dipole centroid in G, to obtain

$$\theta_a^{'} = \theta_a(u-\Delta_u, v-\Delta_v), \tag{5.11}$$

where $\Delta_u = u_a-(u_1+u_2)/2$ and $\Delta_v = v_a-(v_1+v_2)/2$. For the beam shown in Fig. 5.3(a), a background phase function is created with Eqs. (5.10) and (5.11), as shown in Fig 5.3(b). By multiplying the beam G with this background phase function $\theta_a^{'}$, it gets

$$G^{'} = G\exp(i\theta_a^{'}). \tag{5.12}$$

In the propagation of this new beam $G^{'}$, the dipole will annihilate after a much shorter propagation distance than that needed for G. During the propagation of the beam shown in Fig. 5.3(a) with the background phase function as in Eq. (5.12), the dipole annihilates at a propagation distance of $t = 0.11$. Without this background phase, the dipole annihilates at a propagation distance of $t = 0.53$.

Therefore, the dipole annihilation acceleration procedure in a Gaussian beam can be implemented in the following steps:

- Locate the vortices, calculate vortex separation distance, vortex relative angle and vortex morphologies;
- For each dipole, create a new Gaussian beam containing that dipole and propagate it until the dipole is annihilated;
- Extract the background phase from the Gaussian beam after the dipole annihilation;
- Repeat the first three steps until the background phases have been created for all of the dipoles;
- Multiply these background phases with the original beam to obtain a new beam, which shows that the dipoles will annihilate in a relatively short distance of free-space propagation.

5.4 Numerical investigation

Numerical simulations on a computer not only give us considerable insight into the propagation of a vortex-bearing Gaussian beam, but also provide easy control of the beam propagation procedure to simulate complicated physical experiments. To determine the efficiency of the acceleration procedure described in Section 5.3, several numerical simulations are performed with vortex dipoles embedded in a Gaussian beam. These simulations include Gaussian beams with canonically launched vortex dipoles as well as noncanonically launched vortex dipoles. Provided that the vortices are not too far from the optical axis of the Gaussian beam, it is found that, with the background phase, all vortex dipoles annihilate after a shorter propagation distance than without it.

In this section, a typical numerical simulation is provided to test the method of accelerating vortex dipole annihilation in a Gaussian beam. In this simulation, a Gaussian beam propagation is computed with the rigorous scalar diffraction procedure [106]. On the transverse beam planes, the total wave function is represented by an array of 1024×1024 pixels. To be definite the pixel size is set as $\Delta = 10$ μm, and use a wavelength of $\lambda = 1$ μm. The Gaussian beam waist size is $\omega_0 = 640$ μm ($z_R = 1.29$ m). Here, the origin is located at the beam centre.

In its waist, the Gaussian beam contains four vortices, as shown in Figs. 5.4(a) and 5.4(b). Two positive canonical vortices V_1 and V_3 are located at $(300, 300)$ μm and $(-300, -300)$ μm, respectively, and two negative canonical vortices V_2 and V_4 are located at $(-400, 300)$ μm and $(300, -400)$ μm, respectively. Two neighboring oppositely charged vortices can be viewed as a vortex dipole. Therefore, V_1 and V_4 form one vortex dipole with its vortex separation distance $d_{14} = 700$ μm while V_2 and V_3 form another vortex dipole with its vortex separation distance $d_{23} = 608.28$ μm.

Since there are two dipoles in this Gaussian beam, the dynamical behavior of optical vortices will be rather complicated. The details of the dynamical behavior are not discussed here, other than the annihilation distances of the vortex dipoles. According to Eqs. (5.7)-(5.9), a canonically launched vortex dipole will survive all the way to the far field if the vortex separation distance d is larger than the beam waist size ω_0. Therefore, it can be expected that these two dipoles may not annihilate for a long distance of propagation or survive all the way during beam propagation, because the vortex separation distance d_{14} is larger than the beam waist size ω_0 and d_{23} is also approximated to ω_0. As shown in Figs. 5.4(c) and 5.4(d), these two dipoles have still survived after free-space beam propagation over a long distance of $3.1z_R$. It is found that the vortices in these two

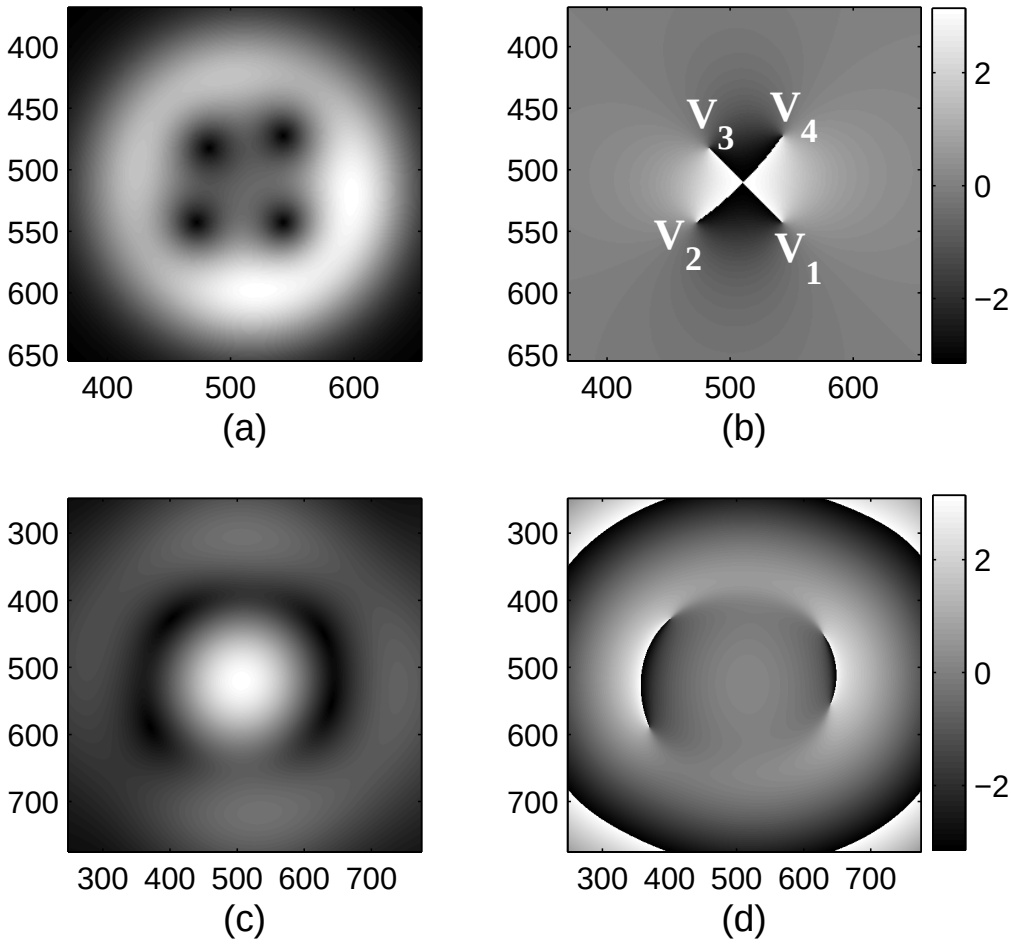

Figure 5.4: Amplitude (a) and phase (b) of a Gaussian beam with two positive canonical vortices (V_1 and V_3) and two negative canonical vortices (V_2 and V_4). The Gaussian beam waist size is $\omega_0 = 640$ μm. Amplitude (c) and phase (d) after the Gaussian beam, as shown in Figure (a) and (b), propagates in free space over a distance of $3.1z_R$. Those two dipoles still exist in the beam with their vortex separation distances being enlarged.

dipoles move apart from each other instead of toward each other. On the transverse plane at $3.1z_R$, d_{14} and d_{23} are enlarged to 1729.85 and 1096.59 μm respectively. It may be expected that these two vortex dipoles may survive during the further beam propagation until they move out of the field.

By using the procedure discussed in Section 5.3, a background phase function is created based on the locations of these two dipoles. For the Gaussian beam with these two dipoles, the resulting background phase function is shown in Fig. 5.5(a). It can be seen that this background phase function is continuous and can be implemented by a deformable mirror. Multiplying this phase with the initial Gaussian beam, a significant difference may be found in the dynamical behavior of these two dipoles. They do not move apart from each other any more, but instead move toward each other and annihilate each other during beam propagation. In Figs. 5.5(c) and 5.5(d), it is shown that all four vortices disappeared through annihilation after a free-space propagation distance of only $0.15z_R$. Further beam propagation for another distance of z_R beyond the annihilation point shows that no vortices arise again in this Gaussian beam. In practice, the resulting continuous phase function after annihilation can be removed with another deformable mirror to obtain a well-corrected beam.

5.5 Conclusion

During the propagation of a Gaussian beam, the vortices embedded in the beam can have very complicated trajectories [69]. Sometimes two oppositely charged vortices will move toward each other and annihilate each other, while at other times they will survive all the way to the far field. Intuitively it can be expected that the background phase function created by a dipole just prior to annihilation should have the potential to force the vortices to move toward each other. Therefore, it can be used to accelerate the dipole annihilation. However, it is impractical to extract this continuous background phase function analytically or numerically before the dipole has annihilated. Instead the continuous background phase function just after the dipole annihilation plane is used, which presumably retains the potential to force the vortices to annihilate each other. This continuous background phase function after dipole annihilation contains no vortices and is therefore assumed to be able to be approximated by deformable mirrors. Numerical simulations show that this continuous phase function can efficiently accelerate the annihilation of vortex dipoles in a Gaussian beam. In fact, it can even force vortices that would have survived all the way to annihilate each other after a relatively short distance of propagation. At the same time,

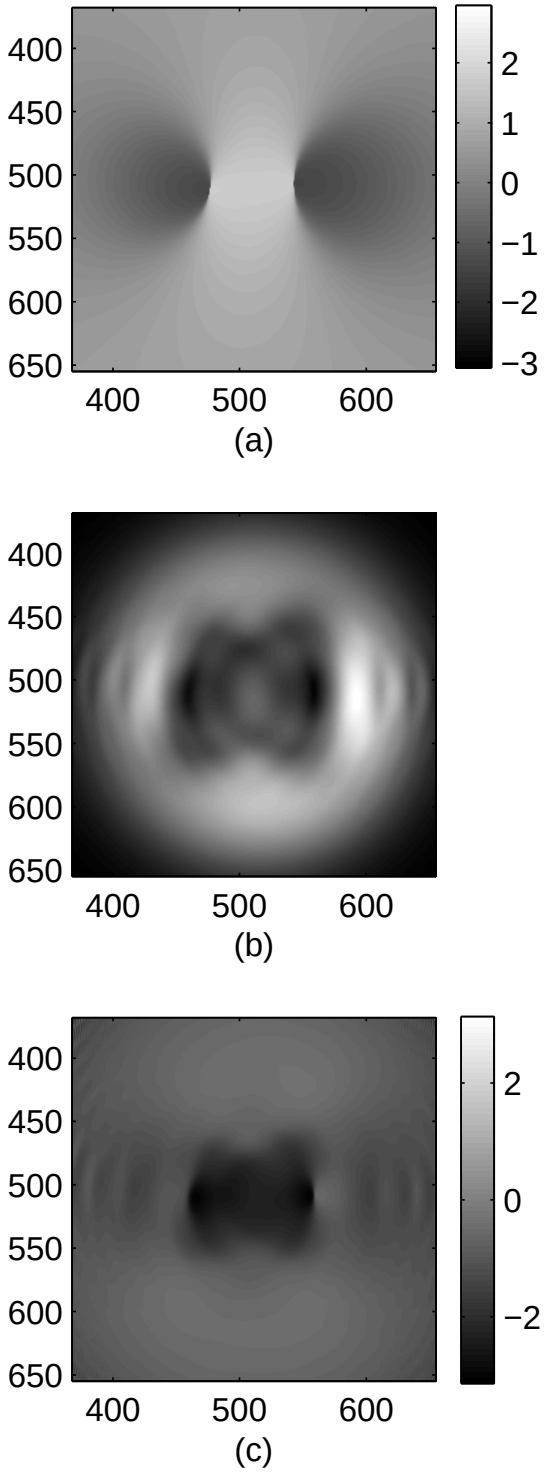

Figure 5.5: Background phase function (a) created to force the vortex dipoles in Fig. 5.4(a) to annihilate. Amplitude (b) and phase (c) of the Gaussian beam after the beam propagated with the background phase as shown in Figure (a) in free space over a distance of $0.15z_R$. All four vortices have disappeared through dipole annihilation.

similar background phase can be created according to the vortex locations in every dipole with the method motioned in this chapter. Therefore, all of the vortex dipoles in a beam can be forced to annihilate with only one step of phase modulation.

The phase function created by this procedure thus provides a way to get rid of optical vortices in an optical beam by forcing vortex dipoles to annihilate efficiently over a relatively short distance of propagation. The continuous phase function that exists after the forced dipole annihilations can be removed with another deformable mirror to obtain a well-corrected beam. This method should be able to remove vortex dipoles in an arbitrary optical beam, including strongly scintillated beams.

Although this background phase created with this method may not be an optimal choice to get rid of optical vortices, it give some indications that optical vortices can be controlled to annihilate with a phase modulation. Whether there are other optimal choices or not still needs to be investigated in the future.

In general, optical beams are noisy and contain numerous optical vortices as a result of beam propagation through a turbulent atmosphere. The analysis in this chapter does not include any noise. It is nevertheless expected that the procedure described here will still be effective in strongly scintillated beams. This is a very important aspect that will be discussed in the next chapter.

Chapter 6

Strongly scintillated beam correction through forced dipole annihilation

6.1 Introduction

In a conventional AO system, the optical wave incident on the receiver aperture is commonly measured by a wavefront sensor, such as a Shack-Hartmann wavefront sensor. In weakly turbulent atmospheric conditions, the wavefront in the receiver aperture is only weakly perturbed and can be accurately reconstructed by so-called wavefront reconstructors [19–21] that employ least-squares methods. The reconstructed wavefront profile must be continuous as it is formed by a deformable mirror.

When the turbulence in the optical path becomes stronger, such as a laser beam that propagates horizontally near the ground for several kilometers, the wavefront in the receiver aperture will be severely distorted with the presence of numerous optical vortices. The optical vortices will cause the wavefront reconstructors in a conventional AO system to fail, because of the violation of the continuous phase assumption. Therefore, the presence of optical vortices severely limits the performance of AO system in strongly scintillated beam corrections. One way to improve the performance of the AO system is to get rid of the optical vortices in the wave field.

In this chapter, based on the previous work of accelerating vortex dipole annihilation in a Gaussian beam in Chapter 5, a beam correction system is proposed with a few conventional AO systems which use the forced dipole annihilation through phase modulation. The least-squares phase correction is used to remove the continuous phase fluctuations in

the wave field. It is found that the removal of the least-squares reconstructed phase in a strongly scintillated beam may cause some vortex dipoles with relatively short separation distances to annihilate by themselves after a short distance of propagation. However, it is not powerful enough to get rid of all optical vortices, especially the vortex dipoles with large separation distances.

Therefore, in addition to measuring and correcting continuous phase fluctuations in the wave field, the vortex locations are also calculated from wavefront measurements. Then vortex dipoles are identified according to vortex locations. For each dipole, a continuous background phase, which is intended to force the dipole to annihilate, is created with the method described in Chapter 5. All these continuous background phase functions, combined with the least-squares phase function, are then implemented by a deformable mirror to correct the incident distorted wave with an AO system. After a short distance of beam propagation, many optical vortices are annihilated in pairs. Owing to the large range of the distribution of the vortex separation distances in a strongly scintillated beam, it is very difficult to find one appropriate beam propagating distance after which all of the optical vortices are annihilated simultaneously. Therefore, another two or three AO systems that implement the same beam corrections are introduced. It is found that most of the optical vortices will be annihilated in pairs after the scintillated beam has passed through a few AO systems with this kind of phase correction scheme, which is referred to as the dipole annihilation and least-squares (DALS) phase correction scheme. As a result, the wavefront of the corrected beam becomes smooth and flat, which can form a higher intensity bright spot on the imaging sensor than the strongly scintillated beam without any correction, or with least-squares phase correction only.

The remainder of this chapter is organized as follows: In Section 6.2, an optical system for strongly scintillated beam correction is presented. The influence of the continuous phase, which is reconstructed from wavefront measurements with least-squares methods, on the vortex dipoles is analyzed in Section 6.2.1. An algorithm is also provided to identify the vortex dipoles from the vortex locations in Section 6.2.2. In Section 6.2.3, a background phase created from the dipoles, combined with the least-squares reconstructed phase, is used to correct the phase distortions in the incident distorted wavefront. Numerical simulations are provided in Section 6.3 to test this optical system on more realistic scintillated beams. Compared with the results obtained from the systems with least-squares phase correction only, statistical curves obtained from the optical system with a DALS phase correction scheme show the significant improvements in the system's performance. Then, conclusions are drawn in Section 6.4.

6.2 Strongly scintillated beam correction system

A functional block diagram of a strong scintillation correction optical system is plotted in Fig. 6.1. In this system, a few AO systems are used to measure and correct the distorted beam successively. Each of them is a conventional AO system composed of a Shack-Hartmann wavefront sensor, a deformable mirror. All but the last AO system implement the new DALS phase correction scheme. The corrected beam then forms an image on the imaging sensor to show the improvement in performance.

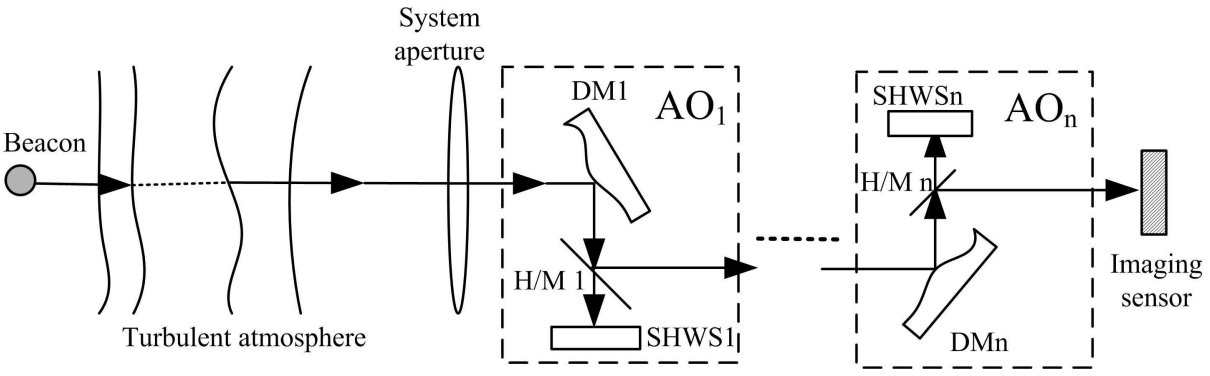

Figure 6.1: Diagram of an optical system for strong scintillation correction. A few AO systems are used in this system. The last AO system is used to correct continuous phase fluctuations by removing the least-squares phase only. Other AO systems are used to fulfil the vortex dipole annihilation and continuous phase correction for the scintillated beam in a successive way.

After an optical beam passes through turbulent atmosphere over a long distance, both the amplitude and the phase of the wave in the system aperture are distorted. Optical vortices can be presented in the system aperture. Let the complex-valued wavefront incident upon the system aperture from the beacon be represented in xy-coordinates by

$$U(x,y) = A(x,y)\exp\left[i\theta(x,y)\right], \tag{6.1}$$

where $A(x,y)$ is the amplitude of the wave field, and $\theta(x,y)$ is the distorted phase function of the wave field, which can be expressed as the sum of a continuous phase function $\theta_c(x,y)$ and a large number of optical vortices $\sum_n^N \phi(x-x_n, y-y_n; \alpha_n, \beta_n)$, as in Eq. (2.40).

This strongly distorted wavefront can be measured by a Shack-Hartmann wavefront sensor. Optical vortices in the wavefront can be located from the outputs of the wavefront sensor. Based on the vortex locations, vortex dipoles can then be identified. The aim of the system is to correct the distorted phase $\theta(x,y)$ by removing the optical vortices and the continuous phase fluctuations in the wave field before the beam forms an image on the imaging sensor.

The continuous phase function $\theta_c(x, y)$ can be reconstructed by a least-squares method and removed by a deformable mirror. However, the solenoidal phase part $\sum_n^N \phi(x - x_n, y - y_n; \alpha_n, \beta_n)$, which represents the contribution of optical vortices, will still remain in the wave field after $\theta_c(x, y)$ has been removed by a least-squares correction. Fig. 6.2(a) shows an example of a distorted phase function which contains a large number of optical vortices. A continuous phase function as shown in Fig. 6.2(b) can be reconstructed from the vortex-bearing phase function as shown in Fig. 6.2(a) with a least-squares method that is described in Subsection 2.3.4. However, after the continuous phase function has been removed from the distorted phase function, the solenoidal phase part still remains in the wave field, as shown in Fig. 6.2(c).

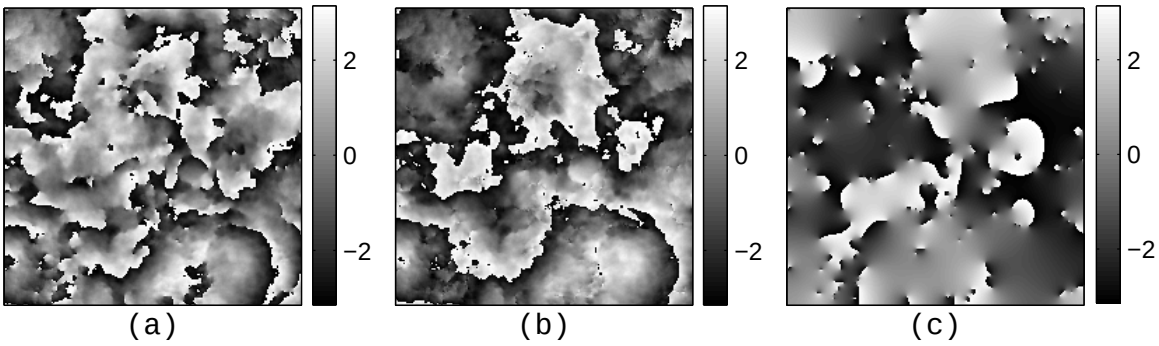

Figure 6.2: Figure (a) shows the distorted phase profile, $\theta(x, y)$, with numerous optical vortices. Figure (b) shows the continuous phase profile, $\theta_c(x, y)$, which is reconstructed from $\theta(x, y)$ with a least-squares method. Figure (c) shows the solenoidal phase profile after $\theta_c(x, y)$ has been removed from $\theta(x, y)$. The vortices are located at the ends of the black-white discontinuity (branch cuts).

It is known that a typical deformable mirror surface cannot be shaped to form a vortex phase profile [15]. In other words, the solenoidal phase part cannot be directly corrected by a typical deformable mirror. In general, optical vortices are created or annihilated on pairs during beam propagation, unless they already exist on the boundary of the optical field and may move out of the field. Therefore, the only way to correct the solenoidal phase part is to get rid of these optical vortices by forcing them to annihilate in pairs. After vortex annihilation, the wavefront becomes continuous and smooth without vortices, and can be corrected by a least-squares reconstructed phase. Based on the theory of accelerating vortex dipole annihilation described in Chapter 5, a background phase, $\theta_b(x, y)$, can be computed based on those vortex dipoles to force them to annihilate after a short distance of propagation. A combination of this background phase $\theta_b(x, y)$ and the continuous phase $\theta_c(x, y)$ still has a continuous profile, which can in principle be approximated by a deformable mirror as

$$\theta^{DM}(x, y) = \theta_c(x, y) - \theta_b(x, y). \tag{6.2}$$

After reflecting from such a deformable mirror, the continuous phase is removed and the distorted phase of the wave field becomes

$$\theta'(x,y) = \sum_{n}^{N} \phi(x - x_n, y - y_n; \alpha_n, \beta_n) + \theta_b(x,y). \tag{6.3}$$

The amplitude of the beam is not changed. This corrected beam, $A(x,y)\exp[i\theta'(x,y)]$, then propagates in free space for a short distance, where many optical vortices may annihilate in pairs. When the beam reaches the next AO system, it contains fewer optical vortices. The phase of the wave field then becomes

$$\theta''(x,y) = \sum_{n'}^{N'} \phi(x - x_{n'}, y - y_{n'}; \alpha_{n'}, \beta_{n'}) + \theta'_c(x,y), \tag{6.4}$$

where $\theta''(x,y)$ contains significantly fewer vortices than $\theta'(x,y)$ due to vortex dipole annihilation; $\theta'_c(x,y)$ is the continuous phase fluctuations because the phase function is distorted again after free-space propagation of a vortex-bearing beam. This process which removes the continuous phase fluctuations and forces dipoles to annihilate is referred to as the dipole annihilation and least-squares (DALS) phase correction.

As predicted in Eq. (5.7), the vortex dipole will annihilate in a distance of propagation, which is proportional to the vortex separation distance. It means that the larger the vortex separation distance is, the longer the required propagation distance for dipole annihilation. It is also true when using a background phase function to force the dipole to annihilate. In a strongly scintillated beam, the vortex separation distances of the dipoles can be distributed over a very large range. It means that different propagation distances are required to force dipoles to annihilate with a background phase. As a result, it is in fact very difficult to force all vortex dipoles to annihilate simultaneously with only one appropriate distance of propagation. Hence, the distorted beam needs to be corrected by a few successive AO systems with the same procedure as in the first AO system. After a few steps of DALS phase correction in the successive AO systems, no vortices are expected to be retained in the wavefront. Only continuous phase fluctuations remain in the wave field, which can be measured and corrected by the last conventional AO system with only a least-squares phase correction. After passing through this AO system, the wavefront becomes flat and is then able to form a high intensity spot on the imaging sensor.

In this strong scintillation correction optical system, conventional AO systems are used with the new DALS phase correction scheme. The important aspect of this system is the computation of the continuous phase function θ_c and the background phase function θ_b in each AO system. The continuous phase function θ_c can be computed by a least-squares method, as described in Subsection 2.3.4. However, the removal of θ_c also influences the

dynamical behavior of vortex dipoles during beam propagation, which will be discussed in the next Subsection 6.2.1. The creation of a background phase that is used to force a vortex dipole in a Gaussian beam to annihilate has already been discussed in Chapter 5. In this chapter, an algorithm will be provided to identify the vortex dipoles in strongly scintillated beams and create a background continuous phase function θ_b based on these vortex dipoles in the following Subsections 6.2.2 and 6.2.3 respectively.

6.2.1 Influence of least-squares reconstructed phase on vortex dipoles

In a conventional AO system, the least-squares reconstructed phase can accurately remove the phase fluctuations in a weakly distorted wavefront with phase conjugation. However, the phase fluctuations cannot be well corrected in a strongly scintillated beam with this kind of AO system owing to the presence of optical vortices. The solenoidal phase part that represents optical vortices still remains after the continuous least-squares phase has been removed, as can be seen in Fig. 6.2(c). However, the removal of the least-squares reconstructed phase from the distorted wavefront does have influence on the optical vortices. From Fig. 6.2(c), it can be seen that the background phase around vortices becomes very smooth compared to that in Fig. 6.2(a). Since a vortex moves around on its embedded background field [79], it can be assumed that the behavior of the optical vortices may be significantly different after the removal of the continuous least-squares phase.

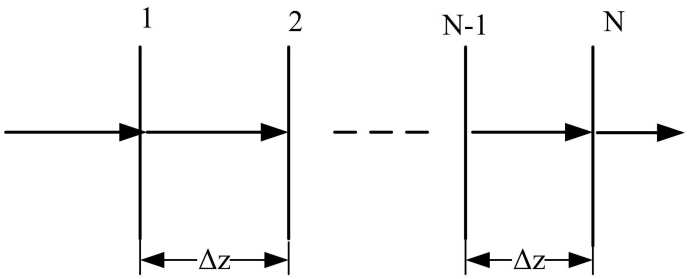

Figure 6.3: Diagram of multi-step least-squares phase correction. At each step, from 1 to N, the continuous phase of the wave field is removed with a least-squares method. The least-squares corrected beam propagates in free space for a distance of $\Delta z = 500$ m before it reaches the next phase correction plane.

To investigate the effect, a specific simulation is performed to implement several consecutive least-squares phase corrections for an arbitrary scintillated beam. The procedure of this least-squares phase correction is shown in Fig. 6.3. The beam that reaches the first correction plane on the left-hand side, is strongly scintillated and contains numerous

optical vortices in its central area. At each plane, from 1 to N, the optical vortices embedded inside the beam central area are counted, and the continuous phase is reconstructed and removed with a least-squares method. Then the corrected beam propagates in free space for a distance of $\Delta z = 500$ m to the next phase correction plane. During each step of beam propagation, some of the vortex dipoles are annihilated. Therefore, it can be expected that fewer optical vortices are retained in the wave field after several steps of least-squares phase corrections.

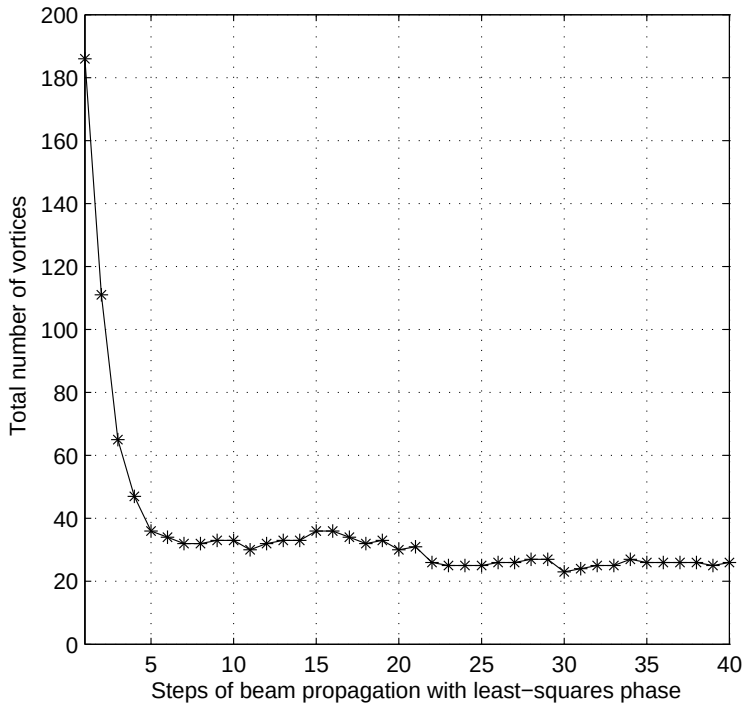

Figure 6.4: Total number of vortices in the beam as a function of the steps of least-squares phase correction.

Figure 6.4 shows the the total number of vortices as a function of the least-squares phase correction steps. In this simulation, this scintillated beam contains 186 vortices in its central area when it reaches first correction plane. It can be seen that the total number of vortices drops quickly to 36 on the 5th correction plane. However, it drops very slowly thereafter. When the beam reaches the 40th correction plane, there are still 26 optical vortices remained in the wave field. By inspecting the total number of vortices after each propagation step, it can be found that more steps of this least-squares phase correction procedure do not reduce the number of vortices significantly after the first five steps. As this simulation shown in Fig. 6.4 has been implemented for a typical strongly scintillated beam, similar simulations can be implemented for other beams. At the same time, this simulation can also be implemented for other beams under different turbulent conditions. It shows the similar trend in the curves of total number of vortices.

To find out how the least-squares phase makes the vortices annihilate, the behavior of optical vortices is compared after one step of propagation for this strongly scintillated beam with and without removing the least-squares phase. The phase function of this scintillated beam, which contains 186 optical vortices, is shown in Fig. 6.5(a). After a short distance of propagation of this scintillated beam, some new vortex dipoles are created while some of the dipoles are annihilated or some of the vortices moves out of the field, as shown in Fig. 6.5(b). If the original phase function shown in Fig. 6.5(a) is corrected by removing the least-squares phase, it can be seen that the phase profile is smoother apart from optical vortices, as shown in Fig. 6.5(c). The vortices are the ends of the branch cuts [14]. After the same distance of propagation, this least-squares phase corrected beam contains fewer optical vortices. The total number of optical vortices in the same central area is now reduced to 110. From the phase function shown in Fig. 6.5(d), it can be seen that some of the vortices are annihilated in pairs. It is noted that the phase is distorted again after the short distance of propagation. This process can be repeated to remove optical vortices.

From the areas circled with the ellipses in Figs. 6.5(b), 6.5(c) and 6.5(d), it can be seen that the vortex dipoles with a relatively short separation distance may annihilate by themselves after the removal of the least-squares phase. It seems that the removal of this continuous phase causes some vortices to obtain the power of moving towards each other and annihilating each other. After the removal of this continuous phase from the scintillated beam, the background phase around any arbitrary vortex becomes smoother and only has the phase contributions created by other vortices.

It can be assumed that each vortex dipole is embedded in a quasi-Gaussian beam after the removal of the least-squares phase. The waist size of the beam is approximated by the speckle size of the scintillated beam. Therefore, some of these vortex dipoles, with their vortex separation distances that are shorter than the waist size of their embedded Gaussian beam, may satisfy the annihilation condition according to Eq. (5.7). As a result, these vortex dipoles in the least-squares corrected beam may annihilate by themselves after a short distance of propagation. To some extent, It can be argued that the least-squares phase correction may change the behavior of some vortex dipoles in a scintillated beam and make them annihilate after propagation.

Figure 6.6 shows the phase function of the same central area of this scintillated beam after 40 steps of least-squares phase correction. Only 26 optical vortices remain in this corrected beam. A total of 160 optical vortices disappeared during beam propagation. It is noted that most of the optical vortices disappear due to the vortex dipole annihilation,

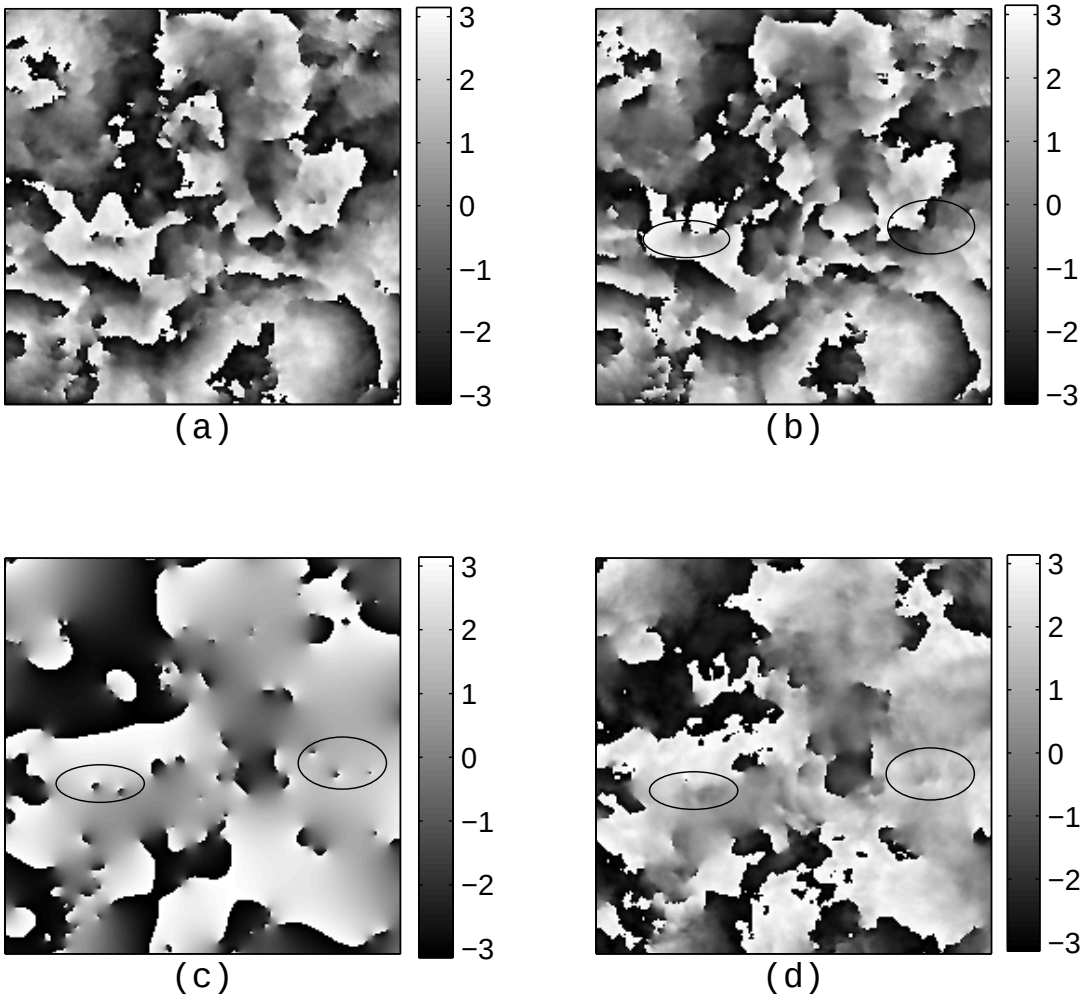

Figure 6.5: Figure (a) shows the phase function of an arbitrary strongly scintillated beam with numerous vortices. Figure (b) shows the phase function after a short distance of propagation of this scintillated beam in figure (a). Figure (c) shows the phase function with the least-squares phase removed from the phase function in figure (a). Figure (d) shows the phase function after a short distance of propagation of the least-squares corrected scintillated beam. Ellipses in Figures (b), (c) and (d) are the same areas for comparison.

while a few of them disappeared by moving out of the central area of the beam. In Fig. 6.6, it can be also seen that vortex separation distances among the remaining vortices are relatively large. It means that this multi-step least-squares phase correction cannot remove vortex dipoles with large separation distances.

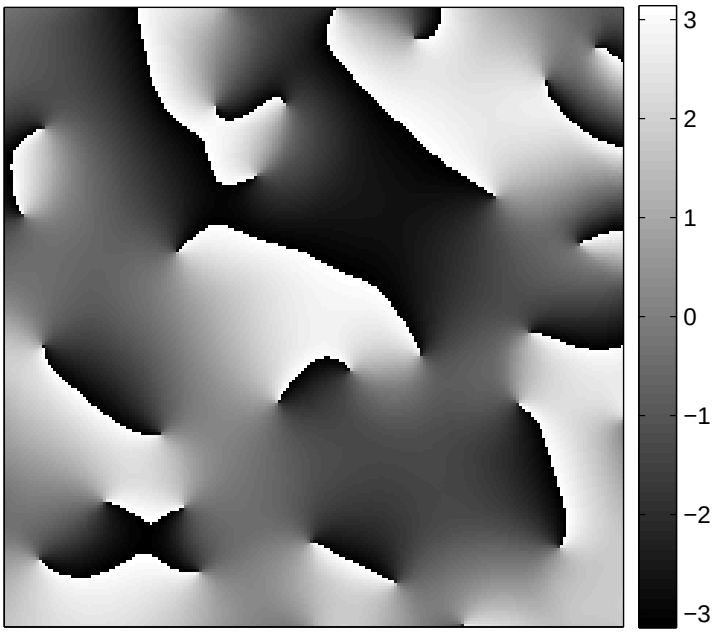

Figure 6.6: Phase profile of a strongly scintillated beam, whose phase is shown as in Fig. 6.5(a), after 40 steps of least-squares phase correction.

A similar argument as before can be used to explain this. It can be assumed that each vortex dipole with a large separation distance is embedded in a quasi-Gaussian beam with a beam waist size approximately equal to the speckle size of the scintillated beam. The vortex separation distance is larger than the beam waist size, and therefore does not satisfy the vortex dipole annihilation condition according to Eq. (5.7). Hence, these vortices may not annihilate each other but move away from each other after propagation. More least-squares phase correction steps will not be able to remove these dipoles. As a result, these vortex dipoles will always remain in the wave field, which is an upper limit of this kind of multi-step least-squares phase correction.

If similar conclusions can be drawn for any arbitrary strongly scintillated beam, it can be argued that least-squares phase correction not only removes the continuous phase but also helps to remove vortex dipoles with relatively short vortex separation distances. However, it cannot correct the vortex dipoles with large separation distances.

6.2.2 Vortex dipole identification in a scintillated beam

To get rid of the optical vortices, it needs to force them to annihilate in pairs. Therefore, firstly it needs to identify the vortex dipoles composed of two oppositely charged vortices with a short vortex separation distance. Optical vortices are always created and annihilated in oppositely charged pairs. After their creation, vortices may move around on the transverse beam plane during beam propagation, which makes the vortex distribution very complicated in a strongly scintillated beam. In general, two oppositely charged vortices, which are closest to each other, can be viewed as a vortex dipole. It is referred to as the *shortest separation distance rule* in vortex dipole identification. With this rule, it is relatively easy to identify the elementary vortex dipoles based on the vortex locations in a wave field.

However, this shortest separation distance rule is not always accurate in the identification of vortex dipoles. For instance consider an arrangement of two positive vortices and two negative vortices as shown in Fig. 6.7(a). It is assumed that these four vortices are relatively far from all other vortices in the beam. According to the shortest separation distance rule, P_1 and N_1 may form a vortex dipole, marked as $\widetilde{P_1N_1}$ (the same notation $\widetilde{PN}$ will be used as a dipole hereafter), because N_1 is the nearest oppositely charged vortex to P_1. After the dipole $\widetilde{P_1N_1}$ is identified, the vortex P_2 must form another dipole with vortex N_2, as $\widetilde{P_2N_2}$. The vortex separation distances of these two dipoles, P_1N_1 and P_2N_2, are shown by the dashed lines in Fig. 6.7(a).

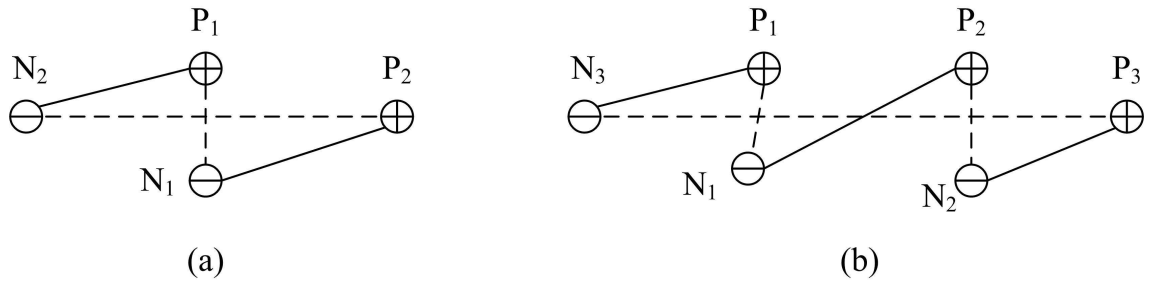

Figure 6.7: Two diagrams of vortex dipole assembly. The positive (negative) vortex is shown by a circled plus (minus). The dashed lines show the connection of two oppositely charged vortices, which form a dipole with the shortest separation distance rule. The solid lines show the connection of two oppositely charged vortices, which form a dipole with the no-cross rule.

Since these two vortex dipoles need to be forced to annihilate with a background phase in a short distance of beam propagation, the vortex dipole assembly of $\widetilde{P_1N_1}$ and $\widetilde{P_2N_2}$ identified by the shortest separation distance rule is not an optimal choice. The reasons

can be explained as follows. According to the annihilation distance in Eq. (5.7), it can be seen that the propagation distance for dipole annihilation is proportional to the vortex separation distance. This is also true for the cases of accelerating the annihilation of a vortex dipole with a background phase. Hence, there will be a big difference in the required annihilation distances for these two dipoles when the separation distance P_1N_1 is much shorter or much larger than P_2N_2. This big difference in required annihilation distances is not advantageous in forcing these two dipoles to annihilate. At the same time, it seems that collisions may arise when these two dipoles are forced to annihilate because their background phases functions are on top of each other for two pairs in Fig. 6.7(a). As a result, more new vortices may be created near the intersection of the connection lines of these two vortex dipoles. Hence, this choice of vortex dipole assembly of $\widetilde{P_1N_1}$ and $\widetilde{P_2N_2}$ has to be discarded. If the the shortest separation distance rule is not used, two vortex dipoles can be identified in another way as $\widetilde{P_1N_2}$ and $\widetilde{P_2N_1}$, with their vortex separation distances, P_1N_2 and P_2N_1, shown by solid lines in Fig. 6.7(a). Then $\widetilde{P_1N_2}$ and $\widetilde{P_2N_1}$ will be an optimal choice. In this vortex dipole assembly, P_1N_2 and P_2N_1 do not intersect, which is referred to as the *no-cross rule* in the vortex dipole identification.

This no-cross rule can be used to rearrange the vortices by exchanging them in dipoles whose connection lines intersect after the dipoles have simply been identified by the shortest separation distance rule. Fig. 6.7(b) shows such an example of vortex dipole assembly. According to the shortest separation distance rule, a vortex dipole $\widetilde{P_1N_1}$ is firstly identified from these six vortices. Similarly, another vortex dipole $\widetilde{P_2N_2}$ is then identified from the remaining four vortices. As a result, $\widetilde{P_3N_3}$ will be identified as a third vortex dipole. Because of the intersection of dashed lines P_1N_1, P_2N_2 and P_3N_3, P_1 and P_3 need to be exchanged so as to rearrange them into two new dipoles, as $\widetilde{P_1N_3}$ and $\widetilde{P_3N_1}$. Similarly, P_3 and P_2 need to be exchanged again so as to rearrange them into another two new dipoles, as $\widetilde{P_2N_1}$ and $\widetilde{P_3N_2}$. Finally, three dipoles, $\widetilde{P_1N_3}$, $\widetilde{P_2N_1}$ and $\widetilde{P_3N_2}$, are obtained, which are connected by solid lines as shown in Fig. 6.7(b).

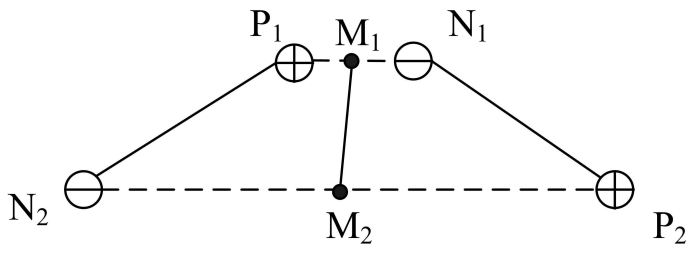

Figure 6.8: Diagram of two neighboring dipoles. M_1 and M_2 are the mid-points of P_1N_1 and P_2N_2 respectively.

Another special case in which the vortices in dipoles have to be rearranged is shown in Fig. 6.8. According to the shortest separation distance rule, two dipoles can be found, $\widetilde{P_1N_1}$ with a relatively short separation distance and $\widetilde{P_2N_2}$ with a relatively large separation distance. It seems that the arrangement of these two dipoles is not in conflict with the no-cross rule. For similar reasons as in the case shown in Fig. 6.7(a), the difference of the required propagation distances for these two dipoles to annihilate will be large when P_1N_1 is much shorter or much larger than P_2N_2. Hence, this dipole assembly is not an optimal arrangement when these dipoles are tried to be forced to annihilate. The vortices need to be rearranged as dipoles, $\widetilde{P_1N_2}$ and $\widetilde{P_2N_1}$, that are connected by solid lines as shown in Fig. 6.8. Here, a judgement is set for this kind of case, that is, if the separation distance between two mid-points M_1 and M_2 is shorter than half of the longer vortex separation distance P_2N_2, the positive vortices are exchanged in these two dipoles. Otherwise, they are not exchanged. This is referred to as the *shorter mid-line rule*.

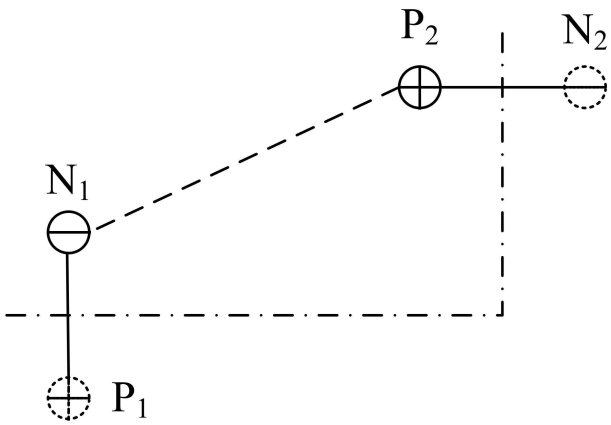

Figure 6.9: Diagram of two vortices, P_2 and N_1, which are close to the field edges. The dash-dotted lines denote the edges of the field. Two dashed line circles denote two virtual vortices outside the field.

The third special case is shown in Fig. 6.9. There are only two oppositely charged vortices in this area. Obviously, these two vortices is viewed as a dipole. However, these two vortices are very close to the field edges. It seems to be easier to force them to move out of the field than force them to annihilate. It can be assumed that there is a virtual positive vortex P_1 at the opposite side of the field edge for the negative vortex N_1. The dipole $\widetilde{P_1N_1}$ will be forced to annihilate. Similarly, there is a virtual negative vortex N_2 at the opposite side of the field edge for the positive vortex P_2 and the dipole $\widetilde{P_2N_2}$ will be forced to annihilate. Similar to the second special case, a judgement is set for this kind of case. If the distances from both vortices to their nearest edges are shorter than half of the vortex separation distance, it is satisfied with the third case and each of the two vortices forms a dipole with its virtual oppositely charged vortex separately. This is referred to as the *edge rule*.

According to these four vortex dipole rules discussed above, vortex dipoles can be identified based on the vortex locations in scintillated beams. An algorithm is proposed here with its flow chart shown in Fig. 6.10. It is noted that some isolated vortices near field edges may be retained in the finite optical field due to an odd number of vortices. The dipoles identified in this way need to be forced to annihilate by using an appropriate background phase, which will be discussed in the next Subsection 6.2.3.

6.2.3 Background phase for vortex dipole annihilation

In each AO step of the beam correction system, the continuous phase θ_c may be computed with a least-squares method. For each vortex dipole identified by the algorithm described in Subsection 6.2.2, a background phase function can be computed to force the dipole to annihilate by the method described in Chapter 5. However, not all of the vortex dipoles are provided with background phase functions, because some of the vortex dipoles will annihilate by themselves during beam propagation after the removal of least-squares phase θ_c. Here, based on the experiences from the numerical simulations, it is found that two oppositely charged vortices that are very close to each other are easy to annihilate by themselves during beam propagation after the removal of θ_c. If the vortex separation distance is shorter than the length of the diagonal line between two pixels, the vortex dipole is not provided with a background phase function.

A continuous background phase θ_b can be expressed as a sum of the background phase functions for all vortex dipoles which are taken into consideration for forced dipole annihilation,

$$\theta_b = \sum_{m}^{M} \theta_m(x - x_m^+, y - y_m^+; x - x_m^-, y - y_m^-), \tag{6.5}$$

where m is an index and M is the number of vortex dipoles that are provided with back ground phase functions; (x_m^+, y_m^+) and (x_m^-, y_m^-) are respectively the locations of the positive and the negative vortex in a dipole; θ_m is the background phase function calculated with the method described in Chapter 5 for each vortex dipole. Since θ_m is a continuous phase function after a dipole annihilation, the sum, θ_b, is also continuous. Hence, $(\theta_c - \theta_b)$ also has a continuous phase profile, which can in principle be implemented by a deformable mirror.

The number of optical vortices is not immediately reduced just after reflecting from the deformable mirror in each AO step. This DALS phase correction only corrects the continuous phase fluctuations and changes the dynamical behavior of vortex dipoles in the

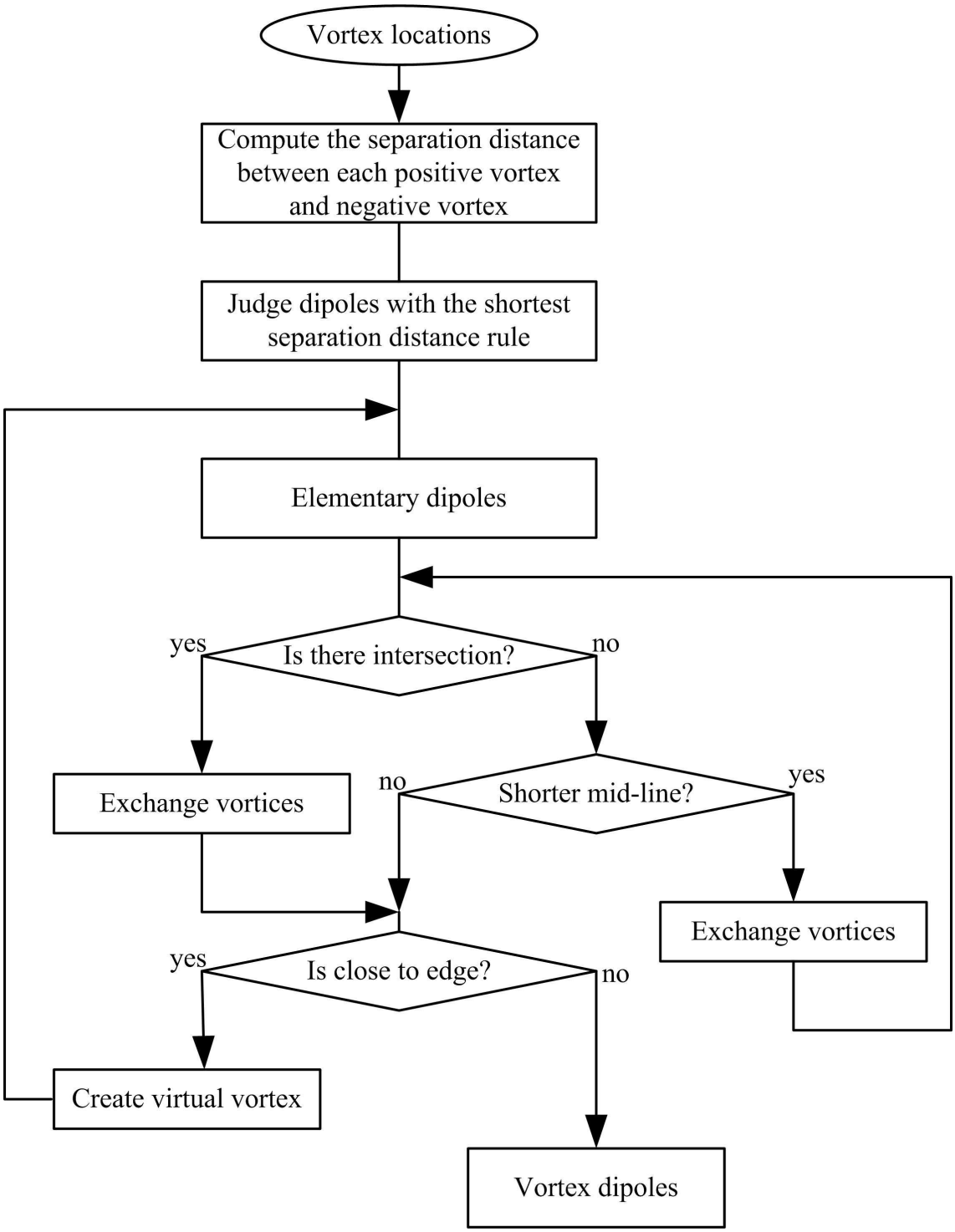

Figure 6.10: Flow chart of dipole identification from vortex locations.

wave field. The vortex dipoles will only be annihilated after some distance of propagation. After dipole annihilation, the solenoidal phase part, which represents the contributions of these optical vortices, is then converted into continuous phase fluctuations. These fluctuations can then be corrected by another least-squares reconstructed phase. With a few steps of DALS phase corrections, the number of vortices in a strongly scintillated beam is significantly reduced.

6.3 Numerical evaluations on the beam correction

6.3.1 Description of numerical simulations

The performance of the proposed correction process is evaluated with the aid of numerical simulations of a light beam propagating through turbulent atmosphere. The simulations follow the layered model of beam propagation, which was described in Section 2.2. A light beam, with a wavelength $\lambda = 500$ nm, propagates through 10 random phase screens that simulate a turbulent optical path of $L = 10$ km. Between consecutive phase screens, the beam propagates in free space for 1 km. Each phase screen represents a layer of turbulent atmosphere with a thickness of $\Delta z = 1$ km, as in Eq. 2.4. Phase screens possess the von Kámán spectrum, as in Eq. 2.2, with a turbulence outer scale of $L_0 = 100$ m. The strength of turbulence in each screen is controlled by adjusting the value of C_n^2. All of these phase screens and propagations are conducted in an $N \times N$ array with sampling space $\Delta = 2$ mm. According to Eq. (3.18), for numerical simulations, the number of an array needs to satisfy, $N \geq 2\lambda\Delta z/\Delta^2$. Here, working with arrays of size $N = 512$ is satisfactory. The central 200×200 pixels in the transverse beam plane is viewed as the system aperture which will be shown in the following figures.

6.3.2 Strongly scintillated beam correction

In this section, one special case will be presented for strongly scintillated beam corrections. A light beam is simulated to pass through a turbulent atmospherical path of 10 km with a turbulent strength of $C_n^2 = 2.52 \times 10^{-15}$ m$^{-2/3}$. After the beam has passed through 10 random phase screens, the optical wave is severely distorted and contains numerous optical vortices. The amplitude and the phase of the scintillated beam in the system aperture are shown in Figs. 6.11(a) and 6.11(b) respectively. In this simulation 186 optical vortices are presented in the system aperture.

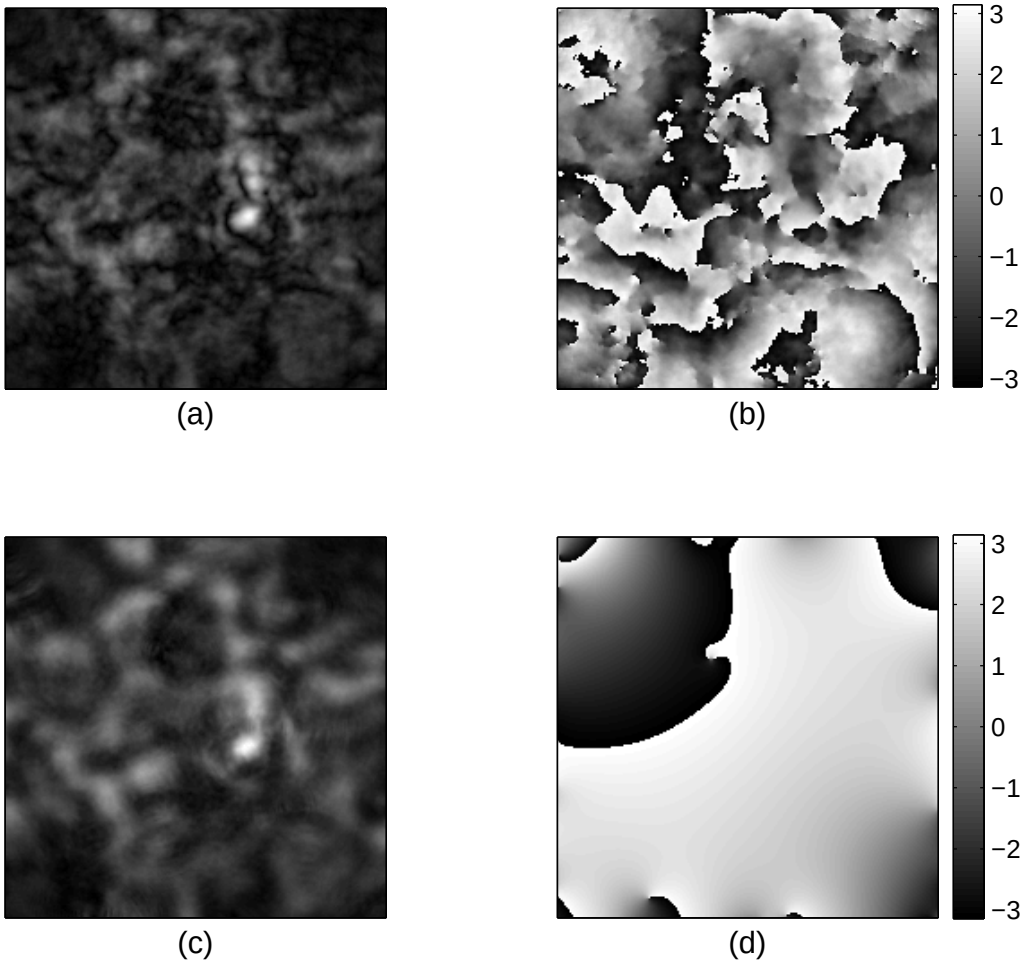

Figure 6.11: Amplitude (a) and phase (b) in the system aperture after a beam has propagated through the turbulent atmosphere over a distance of 10 km with turbulent strength $C_n^2 = 2.52 \times 10^{-15}$ m$^{-2/3}$. In total, there are 93 positive vortices and 93 negative vortices in the wave field. Amplitude (c) and phase (d) of the DALS corrected beam. There are only three optical vortices in the wave field and the phase becomes smooth.

This strongly scintillated beam can be corrected by an optical system with four successive AO systems, as shown in Fig. 6.1. In the first three AO systems, each of them uses DALS phase correction, as described in Section 6.2. After each step of DALS phase correction, the beam propagates in free space over a distance of 500 m, where the beam reaches the next AO system with a large number of optical vortices removed through annihilation. A fourth and last AO system is then used to correct the beam with only least-squares phase correction. Figs. 6.11(c) and 6.11(d) show the amplitude and the phase of the corrected beam respectively. The total number of optical vortices in this corrected beam is reduced to three. As shown in Fig. 6.11(d), the phase profile becomes smooth after such a DALS phase correction scheme.

It is noted that the required propagation distance after each step of DALS phase correction is 500 m in this numerical simulation. As a result, the whole system with four steps will be totally 2 km long, which is impractical in physical systems. However, this problem is actually caused by the limitations of the numerical simulation. Due to limited memory, the size of the arrays that can be used to represent the wave field is also limited. According to the Eq. (3.18), the sampling space can not be made arbitrary small when the propagation distance and wavelength are fixed. The size of large speckles in the scintillated beam is on the order of 20 mm for a sampling space of 2 mm, as is used in the numerical simulations here. If the speckles are viewed as quasi-Gaussian beams, their Rayleigh ranges are on the order of 2400 m. Therefore, a large propagation distance is needed to force the vortex dipoles to annihilate. In a real physical system, the speckle size in a scintillated laser beam would be much smaller than 20 mm. If it is about 1 mm, the required propagation distance will be on the order of 1 m.

6.3.3 Far fields

In a similar simulation, an identical beam propagated through a optical path over 10 km without atmospheric turbulence. Its far field amplitude pattern is a diffraction limited Airy disk, as shown in Fig. 6.12(a). When the strongly scintillated beam, as shown in Figs. 6.11(a) and 6.11(b), propagates into the far field without any correction, its far field amplitude pattern will not be a diffraction limited Airy disk but spread out as a blurred spot, which is shown in Fig. 6.12(b). This strongly scintillated beam can be corrected by least-squares phase correction. Its far field is shown in Fig. 6.12(c). It can be seen that the spot is smaller than the one without any correction. The strongly scintillated beam is propagated into its far field after being corrected by the DALS phase correction scheme. Its far field amplitude pattern is a high intensity bright spot as shown in Fig. 6.12(d).

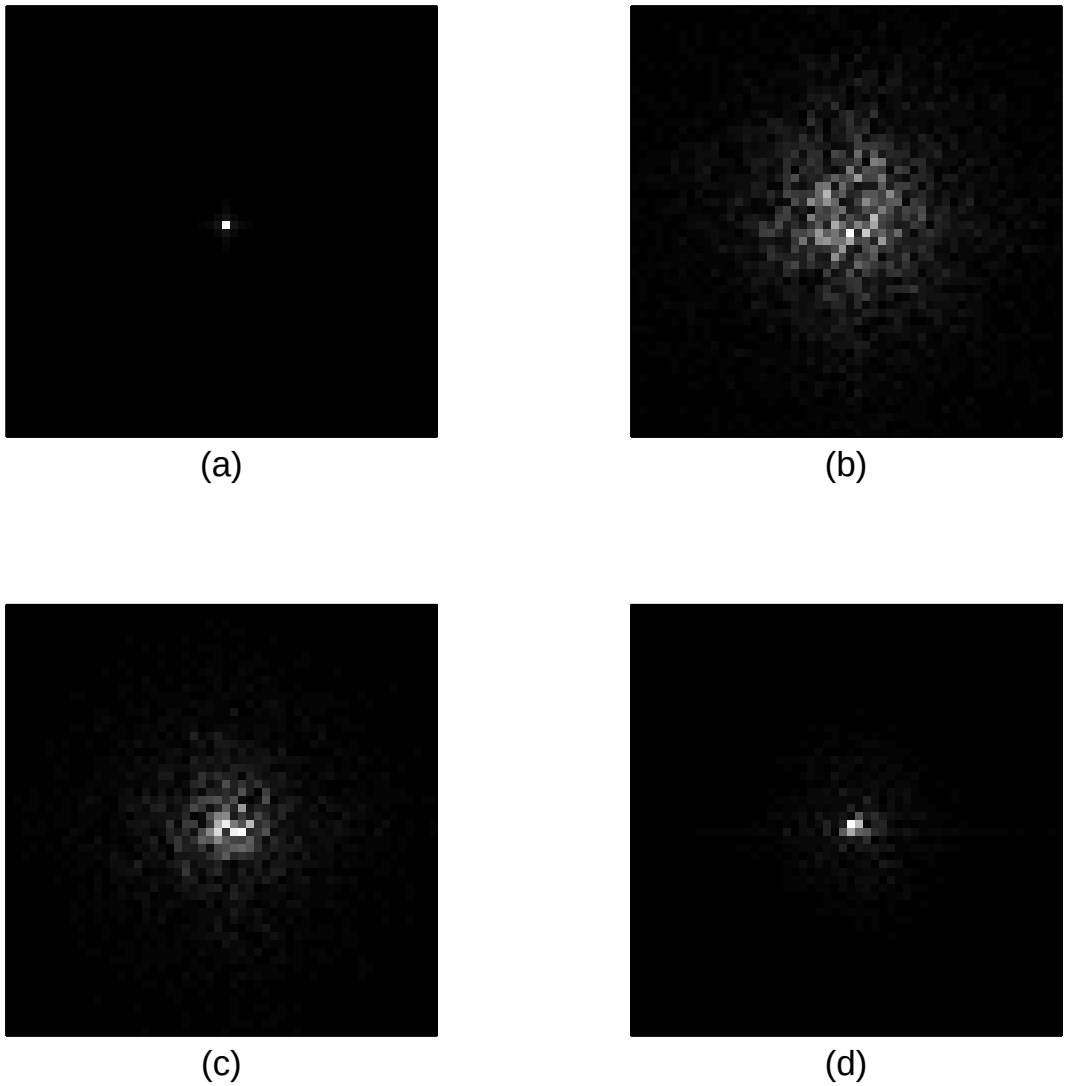

Figure 6.12: Far field amplitude (a) of a beam that propagates through free space. Far field amplitude (b) of a scintillated beam which propagates through turbulent atmosphere over a distance of 10 km, with turbulence strength $C_n^2 = 2.52 \times 10^{-15}$ m$^{-2/3}$. Far field amplitude (c) of the least-squares phase corrected beam. Far field amplitude (d) of the dipole annihilation and least-squares corrected beam.

From the far field amplitude patterns in Figs. 6.12(b), 6.12(c) and 6.12(d), it can be seen that the far field amplitude pattern after the DALS phase correction has a sharp bright spot with smaller size than those of the least-squares phase corrected beam and the uncorrected beam. It also indicates that the DALS phase correction scheme may improve the system performance, and outperforms the least-squares phase correction, under this kind of turbulent condition.

6.3.4 Radially averaged far field amplitude patterns

From numerical simulations, the radially averaged far field amplitude patterns can be computed by averaging the far field amplitude of corrected beams over circles of constant radius, given by

$$\overline{A(r)} = \frac{\int_C A(r,\phi)\mathrm{d}\hat{l}}{\int_C \mathrm{d}\hat{l}}, \tag{6.6}$$

where $A(r,\phi)$ is the amplitude value at the point of (r,ϕ) in the polar coordinates with the origin located at the beam centre in the far field plane; C is the closed integral line which is a circle with the radius of r.

These radially averaged far field amplitude patterns can show the sharpness of the bright spots for different correction schemes in different strengths of turbulence, which may indicate the image qualities of an optical imaging system. Here, three curves of the radially averaged far field amplitude pattern are provided for the turbulent strengths of $C_n^2 = 1.89\times10^{-15}$ m$^{-2/3}$, 2.52×10^{-15} m$^{-2/3}$, 4.41×10^{-15} m$^{-2/3}$, as shown in Figs. 6.13(a) to 6.13(c). These three figures provide comparisons of far field radially averaged amplitude for the results of beam correction under different strengths of turbulence.

From these three figures, it can be seen that the peak values of the far field amplitude reduce as turbulence becomes stronger. It seems that the peak values obtained from the DALS phase correction drop more slowly, as a function of C_n^2, than those obtained from the least-squares phase correction. At the same time, it can also be seen that the patterns obtained from the DALS phase correction are much steeper than those obtained from least-squares only correction, especially under strong turbulent conditions.

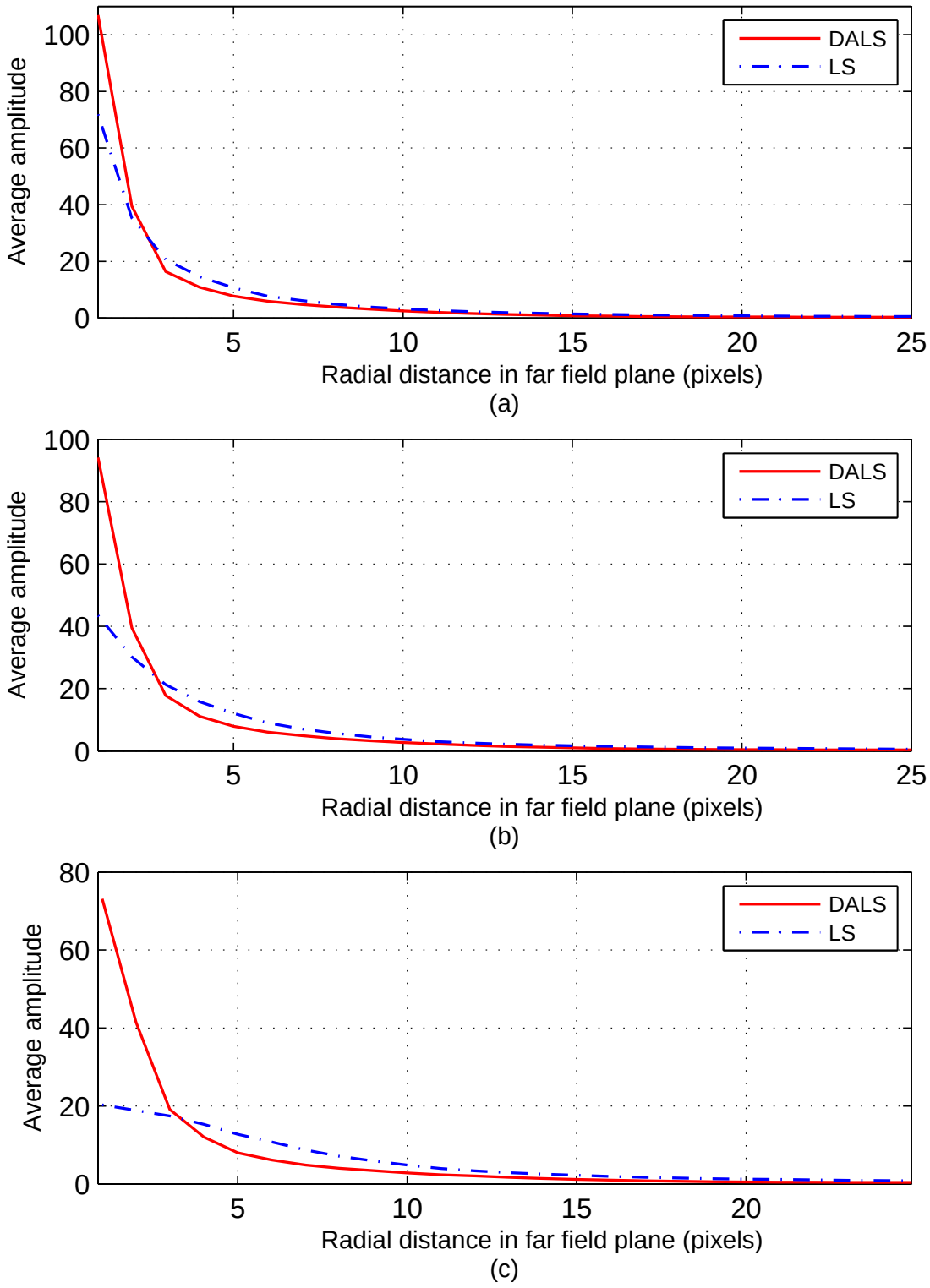

Figure 6.13: Radially averaged far field amplitudes of corrected beams: (a) $C_n^2 = 1.89 \times 10^{-15}$ m$^{-2/3}$; (b) $C_n^2 = 2.52 \times 10^{-15}$ m$^{-2/3}$; (c) $C_n^2 = 4.41 \times 10^{-15}$ m$^{-2/3}$. DALS, shown as the solid curve, is the result obtained from the dipole annihilation and least-squares correction; LS, shown as the dashed curve, is the result obtained from the least-squares only correction.

6.3.5 Total number of optical vortices

In this section, the performance of this beam correction system is evaluated through its ability to get rid of optical vortices in strongly scintillated beams. The vortices in a random wave field show the property of nearest neighbor anticorrelations [41]. The topological charge imbalance in a bounded region is therefore determined by the vortices on the boundary [107]. In other words, it can be expected that the total number of the positive vortices should be the same as the total number of the negative vortices when there are numerous vortices in a strongly scintillated beam. Therefore, only the total number of vortices is considered before and after beam correction. In each simulation, the total number of the optical vortices is counted before and after beam correction. The averaged total number of vortices before beam correction (N_b) is calculated by averaging the counted optical vortices over 50 simulations. The averaged total number of vortices after beam correction (N_a) is also calculated in a same way.

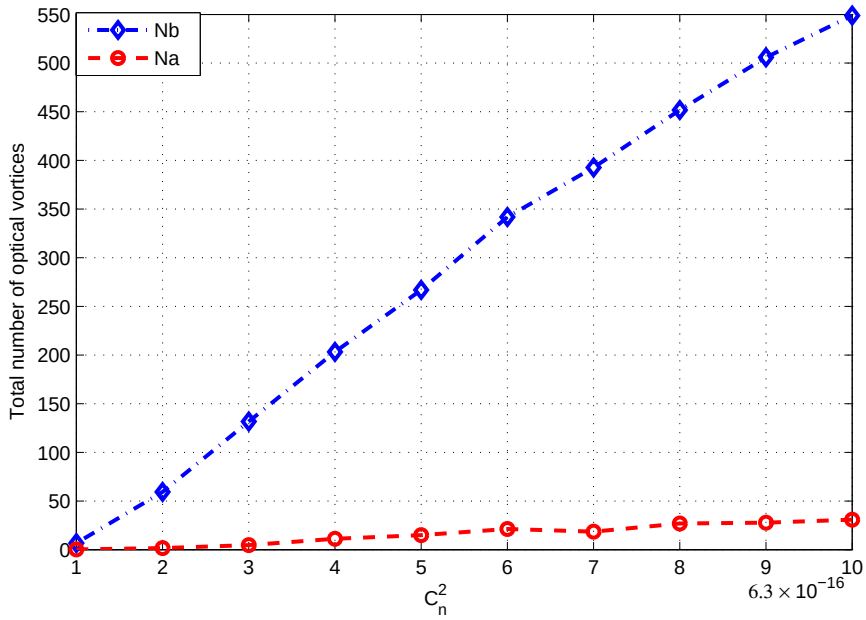

Figure 6.14: The relationship between the averaged total number of vortices and the strength of turbulence C_n^2. The diamonds show the averaged total number of vortices before beam correction (N_b). The circles show the averaged total number of vortices after beam correction (N_a).

Figure 6.14 shows the N_b and N_a as functions of the strength of turbulence. When $C_n^2 \geq 6.3\times10^{-16}$ m$^{-2/3}$, optical vortices begin to occur in the system aperture. It indicates that the onset of strong scintillation occurs in the vicinity of $C_n^2 = 6.3\times10^{-16}$ m$^{-2/3}$ for the geometry studied here. The number of optical vortices in the system aperture increases rapidly when atmospherical turbulence becomes stronger. In numerical simulations, there

are numerous optical vortices in the system aperture $N_b = 548.82$ when the turbulence is very strong ($C_n^2 = 6.3 \times 10^{-15}$ m$^{-2/3}$). After beam correction, the number of optical vortices is reduced significantly, as shown by the curve of N_a in Fig. 6.14. It can be seen that about 95% of the optical vortices are annihilated after beam correction. It indicates that the DALS phase correction scheme can effectively get rid of most vortex dipoles in strongly scintillated beams. Although most of the vortices are removed by the beam correction system, it can also be seen that N_a increases when turbulence becomes stronger. These vortices that remain in the wave field after the beam is corrected can also be removed if another one or two additional AO systems using DALS phase correction are added.

6.3.6 Strehl ratios

In numerical simulations, a beam propagates through a simulated optical path of 10 km with a given strength of turbulence and is then corrected by the optical system as in Fig. 6.1. This propagation and correction procedure is repeated 10 times with a fixed value of C_n^2 so that statistical performance can be determined under different turbulent atmospherical conditions. The outcome beam of the beam correction system with DALS phase correction is allowed to propagate into its far field, where the beam intensity is measured. In the absence of atmospheric turbulence, the intensity pattern would be a diffraction limited Airy disk, but with turbulence and AO correction the pattern is suboptimal. The Strehl ratio, S_r, is often used to evaluate the performance of an optical system [4]. It is given by

$$S_r = \frac{I(0,0)}{I_0(0,0)}, \tag{6.7}$$

where $I(0,0)$ is the actual on-axis far-field intensity and $I_0(0,0)$ is the diffraction limited on-axis far-field intensity. In numerical simulations, the averaged far field on-axis intensity, which is averaged over 50 simulations with a same value of C_n^2, is used to calculate the average Strehl ratio using Eq. (6.7). As a control experiment, the beam corrected by the least-squares phase correction is also allowed to propagate into the far field to obtain its on-axis intensity, and then its average Strehl ratio is computed in the same way for comparison.

Figure 6.15 shows the average Strehl ratios computed for the DALS phase correction and the least-squares phase correction. Both of these two average Strehl ratios drop as the strength of turbulence increases. When turbulence is weak, $C_n^2 \leq 1.26 \times 10^{-15}$ m$^{-2/3}$, these two correction schemes provide similar average Strehl ratios. However, when the

turbulence is stronger, $C_n^2 > 1.26 \times 10^{-15}$ m$^{-2/3}$, DALS phase correction begins to outperform least-squares phase correction. In the regime $C_n^2 \geq 4.41 \times 10^{-15}$ m$^{-2/3}$, the average Strehl ratio for the DALS phase correction is 15 to 25 times larger than that provided by the least-squares phase correction.

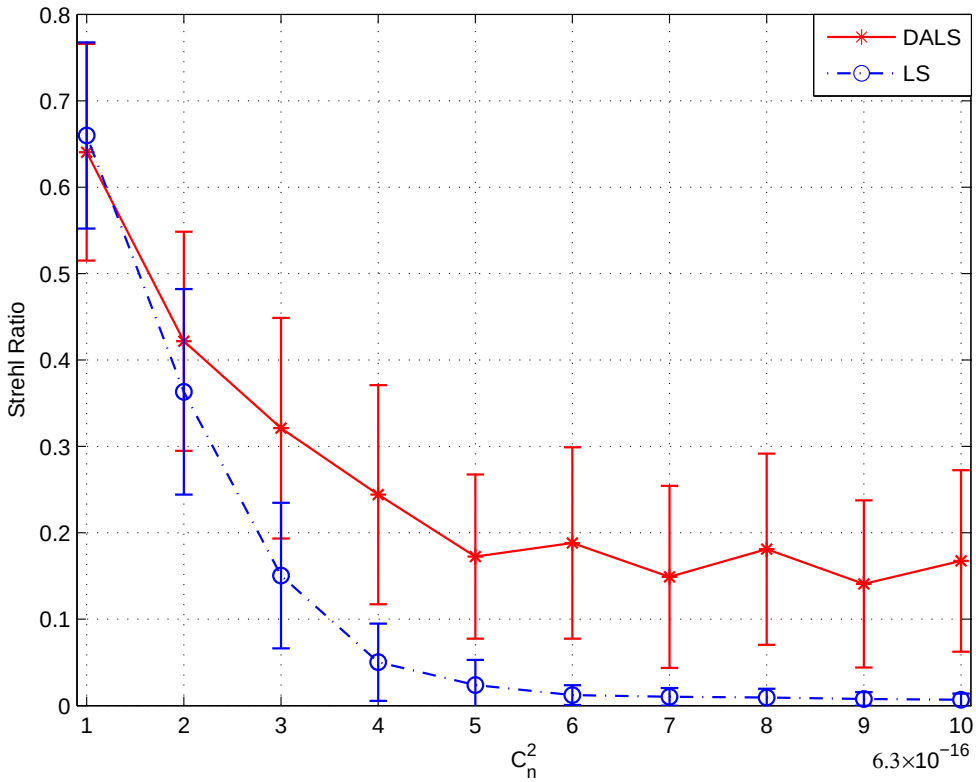

Figure 6.15: Strehl ratio as a function of C_n^2 for two different correction methods. DALS, shown as the solid curve, is the result obtained from the dipole annihilation and least-squares phase correction; LS, shown as the dashed curve, is the result obtained from least-squares phase correction. Error bars show their associated standard deviations.

The difference in the average Strehl ratio provided by these two beam correction procedures can be explained as follows. In weak turbulent conditions, there are few optical vortices in the wave field. The phase distortions are dominated by continuous phase fluctuations, which can be corrected by least-squares method. However, in strong turbulent conditions, there are a large number of optical vortices in the wave field. The phase distortions contain a large solenoidal phase part which cannot be corrected by the least-squares method. The DALS phase correction can convert the solenoidal phase part into continuous phase fluctuations by forcing the vortex dipoles to annihilate. Therefore, DALS phase correction can correct the strongly scintillated beams better than least-squares phase correction.

6.4 Conclusion

In this chapter, a new technique is introduced to correct strongly scintillated beams. It uses the least-squares reconstructed phase to remove the continuous phase fluctuations and forces the vortex dipole to annihilate with a back ground phase.The removal of the least-squares reconstructed phase in a strongly scintillated beam causes some vortex dipoles with short separation distances to annihilate by themselves after a short distance of propagation. An algorithm is proposed to identify vortex dipoles in a scintillated beam based on four rules of dipole identification. A continuous background phase is created to force those vortex dipoles with relatively large separation distances in the wave field to annihilate. The annihilation of vortex dipoles converts the solenoidal part of the phase into continuous phase fluctuations, which in turn can be corrected by a least-squares method.

The numerical simulation results show that DALS phase correction provides a performance improvement over the least-squares phase correction. Most optical vortices are removed from the beam after a few AO steps using DALS phase correction. A factor of up to 25 improvement in the average Strehl ratio shows the better scintillated beam correction with DALS phase correction than the one with least-squares phase correction, especially in strong turbulent conditions.

In this thesis, it is assumed that Shack-Hartmann wavefront sensors can measure the pointwise phase difference and deformable mirrors can change their surfaces with pointwise resolutions. These are idealizations that would be the upper bound of experimental implementations. Practical problems associated with the finite resolutions of the wavefront sensor and deformable mirror have not been investigated here but may form the basis for future studies. At the same time, the vortex separation distance, from which the dipole is considered for forcing annihilation, and the distance of propagation between each two steps of AO are based on experience. Similar to the noise circulation which depends on the ratio of the subaperture size to the Fried parameter r_0 as discussed in Subsection 3.4.2, the optimal choices of these two distances should also depend on their ratios to the Fried parameter. In numerical simulations, four steps of beam corrections are implemented. In total four AO systems were used without considering the cost of these AO systems. There are still some optical vortices remaining in the wave field after beam correction. Therefore, it is important to investigate how to use the least number of AO systems to remove as many of the optical vortices as possible in the future studies.

Chapter 7

Conclusions

7.1 Summary

This thesis mainly focuses on two topics about optical vortices in strongly scintillated beams. One is optical vortex detection with a conventional Shack-Hartmann wavefront sensor. The other is the correction of strongly scintillated beams through forced vortex dipole annihilation.

Based on vortex detection with a line integral over the phase gradient around a vortex, circulation is implemented over the outputs of a Shack-Hartmann wavefront sensor to detect optical vortices. The output of the wavefront sensor is computed with an area integration to obtain an analytical expression for vortex circulation. The vortex locations and topological charges can be determined from the peaks of the circulation. In these investigations, it is shown that this circulation value for a vortex is not $\pm 2\pi$ as is obtained from a line integral, but a smaller value depending on the relative positions and the morphologies of the vortex in the wavefront sensor subaperture. Since the outputs of a Shack-Hartmann wavefront sensor computed with area integrations approximate the outputs computed from the bright spots centroid shifts in a real Shack-Hartmann wavefront sensor, the vortex circulation values may be much closer to the results of physical experiments. At the same time, the influence of the morphology as the vortex is detected with a Shack-Hartmann wavefront sensor is also investigated.

In a strongly scintillated beam, there are generally numerous optical vortices. They are in general created and annihilated as vortex dipoles. Due to the cancellation effects in the circulations, the influence of a vortex dipole on the Shack-Hartmann vortex detection

is also investigated in this thesis. Investigations are carried out in a Gaussian beam for simplicity. Although the morphology of a vortex changes when the vortex is close to the annihilation point, it is shown that the vortex morphology evolution during beam propagation does not have a significant impact on Shack-Hartmann vortex detection. When two oppositely charged vortices approach each other, the vortex circulation peaks may cancel each other out. This cancellation effect is especially strong when the separation distance in a vortex dipole is smaller than twice the size of the Shack-Hartmann wavefront sensor subaperture. Therefore a small separation distance makes the Shack-Hartmann vortex detection more difficult. Statistical results obtained from numerical simulations for Shack-Hartmann vortex detection in strongly scintillated beams show good agreement with the investigations in a Gaussian beam..

For the correction of strongly scintillated beams, continuous phase fluctuations can be corrected with a conventional AO system by removing the least-squares reconstructed phase. This leaves behind the solenoidal phase distortions caused by optical vortices. The only way to correct strongly scintillated beams with numerous optical vortices is to get rid of these optical vortices by forcing them to annihilate in oppositely charged pairs. Since vortices are annihilated in pairs, the global background phase prior to dipole annihilation are investigated. This background phase shows the potential of forcing a vortex dipole to annihilate. However, the extraction of this background phase before dipole annihilation may introduce errors due to the finite resolutions. Therefore, the background phase after dipole annihilation is taken into consideration. Since the phase changes gradually during beam propagation, the background phase after dipole annihilation is assumed to retain the power of forcing a vortex dipole to annihilate. Therefore, a background phase can be created based on the locations of any vortex dipole, and in turn use it to remove vortex dipoles. Numerical simulations show that the background phase after dipole annihilation can efficiently accelerate the annihilation of a vortex dipole. Even if two oppositely charged vortices will move apart from each other and never annihilate each other during beam propagation, this background phase can force them to annihilate.

Based on the concept of accelerating the annihilation of a vortex dipole through continuous background phase modulation, a beam correction system is proposed. It consists of a few conventional AO systems using DALS phase correction. The least-squares phase correction scheme is also used to remove continuous phase fluctuations. It is found that the removal of the least-squares reconstructed phase in a strongly scintillated beam may cause some vortex dipoles with short separation distance to annihilate by themselves after a short distance of propagation. However, it has no impact on dipoles with large separation distances. An algorithm is proposed to identify vortex dipoles according to the

vortex locations. A background phase is created based on these dipoles, and is in turn used to force these dipoles to annihilate. In the beam correction system, the least-squares reconstructed phase together with this background phase are used to get rid of optical vortices and remove the continuous phase fluctuations in a strongly scintillated beam. Numerical simulations show that the number of optical vortices are reduced significantly after a few steps of DALS phase corrections. Several statistical results and curves are obtained and compared with least-squares phase correction, which indicate that the system's performance is improved significantly.

7.2 Assessment

In this thesis, traditional AO systems are successfully used to form a beam correction system for strong scintillations. It is found that a Shack-Hartmann wavefront sensor can detect optical vortices in the scintillated beams. The background phase function that exists after dipole annihilation is used to force a vortex dipole to annihilate. With this new beam correction system, most of the vortices can be removed and a better performance can be obtained compared with the least-squares phase correction.

It should be pointed out that the ability of vortex detection with a Shack-Hartmann wavefront sensor would deteriorate with the increment of phase fluctuations in the wave field. When the noise circulation is larger than 2.2, the vortex circulation will be dominated by noise circulation and therefore the Shack-Hartmann wavefront sensor cannot be used to detect the vortices. As a result, there is an upper limit for the Shack-Hartmann vortex detection in strongly scintillated beams.

In the Chapter 5, the wavefront is continuous after dipole annihilation. The smoothness of the wavefront after dipole annihilation is not investigated in this thesis. However, the wavefront in the vicinity of the dipole annihilation point may have a large gradient [108]. Therefore, errors may arise when a deformable mirror is used to approximate such a surface, which is used to force the vortex dipole to annihilate.

Due to the limitations of the numerical methods used to evaluate the beam correction system, some quantities, such as the propagation distance between two consecutive AO systems, are not practical for a physical system. However, these quantities would be more practical if larger arrays could be used to represent the wave fields.

In the beam correction system, in total four AO systems were used without considering

the cost of these AO systems. Although most optical vortices are removed with the beam correction system, the number of the remaining optical vortices increases when the turbulence strength becomes stronger. As a result, the Strehl ratio drops down with the increment of the turbulence strength in despite of it being higher than that obtained by the least-squares phase correction.

7.3 Future work

There are still some aspects which need to be investigated in future study.

1. Although some numerical simulations about noise circulation have been provided to show the deterioration, further investigation is still needed for the relationship between noise circulation and other parameters, such as wavelength, subaperture size, etc. In this thesis, area integration is used to calculate the phase slopes as an ideal case. In strongly scintillated beams, the increment of phase fluctuations may cause cross-talk [101] among the bright spots on the wavefront sensor focal plane. At the same time, due to the intensity measurement in a real Shack-Hartmann wavefront sensor, the low intensity in the vicinity of a vortex may cause large measuring errors. These aspects also need further investigation.

2. In the dipole annihilation procedure, it has been assumed that the required phase functions are smooth enough to be implemented by a deformable mirror. In practice, this may not always be the case. Therefore, the smoothness of the required phase functions should be investigated.

3. In the investigations of the correction of strongly scintillated beams, it is assumed that the Shack-Hartmann wavefront sensor and the deformable mirror have pointwise resolutions. Actually, this can be viewed as the upper limit of what can be physically implemented. Therefore, practical problems associated with the finite resolutions of the wavefront sensor and deformable mirror still need further investigation.

4. It is necessary to investigate how to use the least number of AO systems to remove as many of the optical vortices as possible and improve the Strehl ratio for the beam with numerous of vortices.

Reference

[1] F. Roddier, "The effects of atmospheric turbulence in optical astronomy," in *Progress in optics*, vol. 19. Amsterdam: North-Holland Publishing Co., 1981, pp. 281–376.

[2] M. C. Roggemann and B. Welsh, *Imaging through turbulence*. Boca Raton: CRC Press, 1996.

[3] H. W. Babcock, "The possibility of compensating astronomical seeing," *Publ. Astron. Soc. Pac.*, vol. 65, pp. 651–236, Oct. 1953.

[4] R. K. Tyson, *Principles of adaptive optics*. San Diego: Academic Press, 1991.

[5] K. M. Hampson, C. Paterson, C. Dainty, and E. A. H. Mallen, "Adaptive optics system for investigation of the effect of the aberration dynamics of the human eye on steady-state accommodation control," *J. Opt. Soc. Am. A*, vol. 23, no. 5, pp. 1082–1088, May 2006.

[6] L. D. S. Haro, "Wavefront sensing in the human eye with a Shack-Hartmann sensor," Ph.D. thesis, Imperial College of Science, Technology and Medicine, University of London, March 2000.

[7] L. C. Andrews and R. L. Phillips, *Laser beam propagation through random media*. Bellingham: SPIE Press, 1998.

[8] J. W. Goodman, *Statistical optics*. New York: John Wiley & Sons, 1985.

[9] B. M. Levine, E. A. Martinsen, A. Wirth, A. Jankevices, M. Toledo-Quinones, F. Landers, and T. L. Bruno, "Horizontal line-of-sight turbulence over near-ground paths and implications for adaptive optics corrections in laser communications," *Appl. Optics*, vol. 37, no. 21, pp. 4553–4560, July 1998.

[10] C. Thompson, S. Wilks, J. Brase, R. Young, G. Johnson, and A. Ruggiero, "Horizontal path laser communications employing MEMS adaptive optics correction,"

in *46th annual meeting international symposium on optical science and technology*, R. K. Tyson, D. Bonaccini, and M. C. Roggemann, Eds., vol. 4494. San Diego, CA: SPIE, July 2001, pp. 89–95.

[11] T. Weyrauch, M. A. Vorontsov, J. W. Gowens, and T. G. Bifano, "Fiber coupling with adaptive optics for free-space optical communication," in *Free-Space Laser Communication and Laser Imaging*, Proceedings of SPIE, D. G. Voelz and J. C. Ricklin, Eds., vol. 4489, 2002, pp. 177–184.

[12] X. Zhu and J. M. Kahn, "Free-space optical communication through atmospheric turbulence channels," *IEEE T. Commun.*, vol. 50, no. 8, pp. 1293–1300, Aug. 2002.

[13] M. Wright, M. Srinivasan, and K. Wilson, "Improved optical communications performance using adaptive optics with an avalanche photodiode detector," the Jet Propulsion Laboratory, California institute of Technology, Tech. Rep., May 2005.

[14] D. L. Fried and J. L. Vaughn, "Branch cuts in the phase function," *Appl. Optics*, vol. 31, no. 15, pp. 2865–2882, May 1992.

[15] N. Baranova, A. Mamaev, N. Pilipetsky, V. Shkunov, and B. Zel'dovich, "Wavefront dislocations: topological limitations for adaptive systems with phase conjugation," *J. Opt. Soc. Am.*, vol. 73, no. 5, pp. 525–528, May 1983.

[16] V. P. Lukin and B. V. Fortes, "The influence of wavefront dislocations on phase conjugation instablity with thermal blooming compensation," *J. Opt. A–Pure Appl. Op.*, vol. 6, pp. 103–116, 1997.

[17] K. D. Ridley, "Limits to phase-only correction of scintillated laser beams," *Opt. Commun.*, vol. 144, pp. 299–305, Dec. 1997.

[18] C. A. Primmerman, T. R. Price, R. A. Humphreys, B. G. Zollars, H. T. Barclay, and J. Herrman, "Atmospheric-compensation experiments in strong-scintillation conditions," *Appl. Optics*, vol. 34, no. 12, pp. 2081–2088, Apr. 1995.

[19] R. H. Hudgin, "Wave-front reconstruction for compensated imaging," *J. Opt. Soc. Am. A*, vol. 67, no. 3, pp. 375–378, Mar. 1977.

[20] D. L. Fried, "Least-square fitting a wave-front distortion estimate to an array of phase-difference measurements," *J. Opt. Soc. Am. A*, vol. 67, no. 3, pp. 370–375, Mar. 1977.

[21] W. Southwell, "Wave-front estimation from wave-front slope measurements," *J. Opt. Soc. Am. A*, vol. 70, no. 8, pp. 998–1006, Aug. 1980.

[22] J. Herrmann, "Least-squares wave front errors of minumum norm," *J. Opt. Soc. Am. A*, vol. 70, no. 1, pp. 28–35, Jan. 1980.

[23] M. A. van Dam and R. G. Lane, "Wave-front sensing from defocused images by use of wave-front slopes," *Appl. Optics*, vol. 41, no. 26, pp. 5497–5502, Sept. 2002.

[24] A. Talmi and E. N. Ribak, "Wavefront reconstruction from its gradients," *J. Opt. Soc. Am. A*, vol. 23, no. 2, pp. 1–10, 2006.

[25] J. D. Barchers, D. L. Fried, and D. J. Link, "Evaluation of the performance of Hartmann sensors in strong scintillation," *Appl. Optics*, vol. 41, no. 6, pp. 1012–1021, Feb. 2002.

[26] D. L. Fried, "Branch point problem in adaptive optics," *J. Opt. Soc. Am. A*, vol. 15, no. 10, pp. 2759–2768, Oct. 1998.

[27] W. W. Arrasmith, "Branch-point-tolerant least-squares phase reconstructor," *J. Opt. Soc. Am. A*, vol. 16, no. 7, pp. 1864–1872, July 1999.

[28] G. A. Tyler, "Reconstruction and assessment of the least-squares and slope discrepancy components of the phase," *J. Opt. Soc. Am. A*, vol. 17, no. 10, pp. 1828–1839, Oct. 2000.

[29] V. P. Aksenov and O. V. Tikhomirova, "Theory of sigular-phase reconstruction for an optical speckle field in the turbulent atmosphere," *J. Opt. Soc. Am. A*, vol. 19, no. 2, pp. 345–355, Feb. 2002.

[30] M. Hattori and S. Komatsu, "An exact formulation of a filter for rotation in phase gradients and its applications to wavefront reconstruction problems," *J. Mod. Optic.*, vol. 50, no. 11, pp. 1705–1723, 2003.

[31] J. Notaras and C. Paterson, "Demonstration of closed-loop adaptive optics with a point-diffraction interferometer in strong scintillation with optical vortices," *Opt. Express*, vol. 15, no. 21, pp. 13 745–13 756, Oct. 2007.

[32] D. L. Fried, "Adaptive optics wave function reconstruction and phase unwrapping when branch points are present," *Opt. Commun.*, vol. 200, no. 1-6, pp. 43–72, Dec. 2001.

[33] D. C. Ghiglia and M. D. Pritt, *Two-dimensional phase unwrapping: theory, algorithms, and software*. New York: Wiley, 1998.

[34] M. C. Roggemann and A. C. Koivunen, "Branch-point reconstruction in laser beam projection through turbulence with finite-degree-of-freedom phase-only wave-front conrrection," *J. Opt. Soc. Am. A*, vol. 17, no. 1, pp. 53–62, Jan. 2000.

[35] M. C. Roggemann and A. C. Koivunen, "Wave-front sensing and deformable-mirror control in strong scintillation," *J. Opt. Soc. Am. A*, vol. 17, no. 5, pp. 911–919, May 2000.

[36] V. P. Lukin, F. Y. Kanev, V. A. Sennikov, N. A. Makenova, V. A. Tartakovskii, and P. A. Konyaev, "Phase and amplitude-phase control of a laser beam propagating in the atmosphere," *Quantum Electron+*, vol. 34, no. 9, pp. 825–832, 2004.

[37] M. C. Roggemann and D. J. Lee, "Two-deformable-mirror concept for correcting scintillation effects in laser beam projection through the turbulent atmosphere," *Appl. Optics*, vol. 37, no. 21, pp. 4577–4585, July 1998.

[38] J. D. Barchers and B. L. Ellerbroek, "Improved compensation of turbulence-induced amplitude and phase distortions by means of multiple near-field phase adjustments," *J. Opt. Soc. Am. A*, vol. 18, no. 2, pp. 399–411, Feb. 2001.

[39] J. Nye and M. Berry, "Dislocations in wave trains," *Proc. R. Soc. Lond. A*, vol. 336, pp. 165–190, 1974.

[40] P. Coullet, L. Gil, and F. Rocca, "Optical vortices," *Opt. Commun.*, vol. 73, no. 5, pp. 403–408, Nov. 1989.

[41] N. Shvartsman and I. Freund, "Vortices in random wave fields: nearest neighbor anticorrelations," *Phys. Rev. Lett.*, vol. 72, no. 7, pp. 1008–1012, Feb. 1994.

[42] I. Freund and V. Freilikher, "Parameterization of anisotropic vortices," *J. Opt. Soc. Am. A*, vol. 14, no. 8, pp. 1902–1910, Aug. 1997.

[43] M. Berry, "Disruption of wavefronts: statistics of dislocations in incoherent Gaussian random waves," *J. Phys. A–Math. Gen.*, vol. 11, no. 1, pp. 27–37, 1978.

[44] N. Baranova, B. Zel'dovich, A. Mamaev, N. Pilipetsky, and V. Shkunov, "Dislocation of the wave-front of a specle-inhomogeneous field (theory and experiment)," *JETP Lett+*, vol. 33, no. 4, pp. 195–199, Feb. 1981.

[45] I. Freund, "Optical vortices in Gaussian random wave fields: statistical probability densities," *J. Opt. Soc. Am. A*, vol. 11, no. 5, pp. 1644–1652, May 1994.

[46] M. Berry and M. Dennis, "Phase singularities in isotropic random waves," *Proc. R. Soc. Lond. A*, vol. 456, pp. 2059–2079, 2000.

[47] W. Wang, S. G. Hanson, Y. Miyamoto, and M. Takeda, "Experimental investigation of local properties and statistics of optical vortices in random wave fields," *Phys. Rev. Lett.*, vol. 94, no. 10, pp. 103 902–1–4, Mar. 2005.

[48] V. V. Voitsekhovich, D. Kouznetsov, and D. K. Morozov, "Density of turbulence-introduced phase dislocations," *Appl. Optics*, vol. 37, no. 21, pp. 4525–4535, 1998.

[49] M. R. Dennis, "Phase critical points densities in planar isotropic random waves," *J. Phys. A–Math. Gen.*, vol. 34, pp. 297–303, Mar. 2001.

[50] F. S. Roux, "Optical vortex density limitation," *Opt. Commun.*, vol. 223, pp. 31–37, July 2003.

[51] I. Freund, "Saddles, sigularities, and extrema in random phase fields," *Phys. Rev. E*, vol. 52, no. 3, pp. 2348–2360, Sept. 1995.

[52] I. Freund and N. Shvartsman, "Wave-field phase singularities: The sign principle," *Phys. Rev. A*, vol. 50, no. 6, pp. 5164 – 5172, Dec. 1994.

[53] B. I. Zel'dovich, N. F. Pilipetskii, and V. V. Shkunov, *Principles of phase conjugation*. Berlin and New York: Springer-Verlag (Springer Series in Optical Sciences), B. I. Zel'dovich and N. F. Pilipetskii and V. V. Shkunov, Eds., 1985, vol. 42.

[54] I. Freund, "Critical point explosions in two-dimensional wavefields," *Opt. Commun.*, vol. 159, pp. 99–117, Jan. 1999.

[55] M. Berry, "Optical vortices evolving from helicoidal integer and fractional phase steps," *J. Opt. A–Pure Appl. Op.*, vol. 6, pp. 259–268, 2004.

[56] V. V. Kotlyar, A. A. Almazov, S. N. Khonina, and V. A. Soifer, "Generation of phase singularity through diffracting a plane or Gaussian beam by a spiral phase plate," *J. Opt. Soc. Am. A*, vol. 22, no. 5, pp. 849–861, May 2005.

[57] J. Masajada and B. Dubik, "Optical vortex generation by three plane wave interference," *Opt. Commun.*, vol. 198, pp. 21–27, Oct. 2000.

[58] N. R. Heckenberg, R. McDuff, C. P. Smith, and A. G. White, "Generation of optical phase singularities by computer-generated holograms," *Opt. Lett.*, vol. 17, no. 3, pp. 221–223, 1992.

[59] C. Shan Guo, X. Liu, X. Yun Ren, and H. Tian Wang, "Optimal annular computer-generated holograms for the generation of optical vortices," *J. Opt. Soc. Am. A*, vol. 22, no. 2, pp. 385–390, Feb. 2005.

[60] V. P. Lukin, V. A. Sennikov, and V. A. Tartakovskii, "Optical vortices: creation, annihilation and modeling," in *Laser Weapons Technology III*, Proceedings of SPIE, W. E. Thompson and P. H. Merritt, Eds., vol. 4724, 2002, pp. 85–93.

[61] N. R. Heckenberg, M. Vaupel, J. T. Malos, and C. O. Weiss, "Optical-vortex pair creation and annihilation and helical astigmatism of a nonplanar ring resonator," *Phys. Rev. A*, vol. 54, no. 3, pp. 2369–2378, Sept. 1996.

[62] M. Vasnetsov and K. Staliunas, *Optical vortices*, vol. 228 in Horizons in Wold Physics, New York: Nova Science Publishers, 1999.

[63] J. Herrmann, "Cross coupling and aliasing in modal wave-front estimation," *J. Opt. Soc. Am. A*, vol. 71, no. 8, pp. 989–992, Aug. 1981.

[64] E.-O. L. Bigot and W. J. Wild, "Theory of branch-point detection and its implementation," *J. Opt. Soc. Am. A*, vol. 16, no. 7, pp. 1724–1729, July 1999.

[65] G. Indebetouw, "Optical vortices and their propagation," *J. Mod. Optic.*, vol. 40, no. 1, pp. 73–87, 1993.

[66] I. Basistiy, V. Bazhenov, M. Soskin, and M. Vasnetsov, "Optics of light beams with screw dislocations," *Opt. Commun.*, vol. 103, pp. 422–428, 1993.

[67] D. Rozas, Z. S. Sacks, and G. A. Swartzlander, "Experimental observation of fluidlike motion of optical vortices," *Phys. Rev. Lett.*, vol. 79, no. 18, pp. 3399–3402, Nov. 1997.

[68] A. V. Mamaev, M. Saffman, and A. A. Zozulya, "Propagation of a mutulally incoherent optical vortex pair in anisotropic nonlinear media," *J. Opt. B–Quantum Semic. Opt.*, vol. 6, pp. S318–S322, 2004.

[69] F. S. Roux, "Canonical vortex dipole dynamics," *J. Opt. Soc. Am. B*, vol. 21, no. 3, pp. 655–663, Mar. 2004.

[70] J. T. Malos, K. Staliunas, M. Vaupel, and C. O. Weiss, "Three-dimensional representation of two-dimensional vortex dynamics in lasers," *Opt. Commun.*, vol. 128, pp. 123–135, July 2002.

[71] M. V. Berry and M. R. Dennis, "Topological events on wave dislocation lines: birth and death of loops, and reconnection," *J. Phys. A–Math. Theor.*, vol. 40, pp. 65–74, 2007.

[72] I. Freund, "Optical vortex trajectories," *Opt. Commun.*, vol. 181, pp. 19–33, July 2000.

[73] I. Freund and D. A. Kessler, "Critical point trajectory bundles in singular wave fields," *Opt. Commun.*, vol. 187, pp. 71–90, Jan. 2001.

[74] R. P. Singh and S. R. Chowdhury, "Noncanonical vortex transformation and propagation in a two-dimensional optical system," *J. Opt. Soc. Am. A*, vol. 20, no. 3, pp. 573–576, Mar. 2003.

[75] F. S. Roux, "Spatial evolution of the morphology of an optical vortex dipole," *Opt. Commun.*, vol. 236, pp. 433–440, Mar. 2004.

[76] A. Y. Bekshaev, M. V. Vasnetsov, and M. Soskin, "Description of the morphology of optical vortices using the orbital angular momentum and its components," *Opt. Spectrosc+*, vol. 100, no. 6, pp. 910–915, 2006.

[77] K. Staliunas, "Dynamics of optical vortices in a laser beam," *Opt. Commun.*, vol. 90, no. 1, pp. 123–127, June 1992.

[78] F. S. Roux, "Dynamical behavior of optical vortices," *J. Opt. Soc. Am. B*, vol. 12, no. 7, pp. 1215–1221, July 1995.

[79] D. Rozas, C. T. Law, and G. A. Swartzlander, "Propagation dynamics of optical vortices," *J. Opt. Soc. Am. A*, vol. 14, no. 11, pp. 3054–3065, Nov. 1997.

[80] D. Rozas, "Generation and propagation of optical vortices," Ph.D. dissertation, Worcester Polytechnic Institute, Aug. 1999.

[81] U. Schwarza, S. Sogomoniana, and M. Maier, "Propagation dynamics of phase dislocations embedded in a Bessel light beam," *Opt. Commun.*, vol. 208, p. 255–262, July 2002.

[82] F. Flossmann, U. T. Schwarz, and M. Maier, "Optical vortices in a Laguerre-Gaussian LG_1^0 beam," *J. Mod. Optic.*, vol. 52, no. 7, pp. 1009–1017, May 2005.

[83] F. Flossmann, U. T. Schwarz, and M. Maier, "Propagating dynamics of optical vortices in Laguerre-Gaussian beams," *Opt. Commun.*, vol. 250, pp. 218–230, Feb. 2005.

[84] G. Molina-Terriza, E. M. Wright, and L. Torner, "Propagation and control of noncanonical optical vortices," *Opt. Lett.*, vol. 26, no. 3, pp. 163–165, Feb. 2001.

[85] G.-H. Kim, H. J. Lee, J.-U. Kim, and H. Suk, "Propagation dynamics of optical vortices with anisotropic phase profiles," *J. Opt. Soc. Am. B*, vol. 20, no. 2, pp. 351–359, Feb. 2003.

[86] D. Neshev, A. Dreischuh, M. Assa, and S. Dinev, "Motion control of ensembles of ordered optical vortices generated on finite extent background," *Opt. Commun.*, vol. 151, pp. 413–421, June 1998.

[87] J. M. Martin and S. M. Flatté, "Intensity images and statistics from numerical simulation of wave propagation in 3-d random media," *Appl. Optics.*, vol. 27, no. 11, pp. 2111–2126, June 1988.

[88] W. A. Coles, J. P. Filice, R. G. Frehlich, and M. Yadlowsky, "Simulation of wave propagation in three-dimensional random media," *Appl. Optics*, vol. 34, no. 12, pp. 2098–2101, Apr. 1995.

[89] R. Frehlich, "Simulation of laser propagation in a turbulent atmospher," *Appl. Optics*, vol. 39, no. 3, pp. 393–397, Jan. 2000.

[90] D. L. Knepp, "Multiple phase-screen calculation of the temporal behavior of stochastic waves," *Proceedings of the IEEE*, vol. 71, no. 6, pp. 722–737, June 1983.

[91] R. N. Bracewell, *The Fourier transform and its applications*, 2nd ed., ser. McGraw-Hill electrical and electronic engineering series. New York: McGraw-Hill, 1978.

[92] V. I. Tatarskii, *The effects of the turbulent atmosphere on wave propagation.* Jerusalem: Israel Program for Scientific Translations, 1971.

[93] D. L. Fried, "Statistics of a geometric representation of wavefront distortion," *J. Opt. Soc. Am.*, vol. 55, no. 11, pp. 1427–1435, Nov. 1965.

[94] D. L. Fried, "Optical resolution through a randomly inhomogeneous medium for very long and very short exposures," *J. Opt. Soc. Am.*, vol. 56, no. 10, pp. 1372–1379, Oct. 1966.

[95] R. A. Fisher, *Optical phase conjugation.* New York: Academic Press, 1983.

[96] V. V. Voitsekhovich, L. J. Sánchez, and V. G. Orlov, "Effect of scintillation on adaptive optics systems," *Rev. Mex. Astron. Astr.*, vol. 38, pp. 193–198, Oct. 2002.

[97] Y. Y. Schechner and J. Shamir, "Parameterization and orbital angular momentum of anisotropic dislocations," *J. Opt. Soc. Am. A*, vol. 13, no. 5, pp. 967–973, May 1996.

[98] F. S. Roux, "Coupling of noncanonical optical vortices," *J. Opt. Soc. Am. B*, vol. 21, no. 3, pp. 664–670, Mar. 2004.

[99] F. S. Roux, "Distribution of angular momentum and vortex morphology in optical beams," *Opt. Commun.*, vol. 268, pp. 15–22, Aug. 2004.

[100] F. S. Roux, "Fluid dynamical enstrophy and the number of optical vortices in a paraxial beam," *Opt. Commun.*, vol. 242, pp. 45–55, July 2006.

[101] M. C. Roggemann and T. J. Schulz, "Algorithm to increase the largest aberration that can be reconstructed from Hartmann sensor measurements," *Appl. Optics*, vol. 37, no. 20, pp. 4321–4329, July 1998.

[102] M. Chen, F. S. Roux, and J. C. Olivier, "Detection of phase singularities with a Shack-Hartmann wavefront sensor," *J. Opt. Soc. Am. A*, vol. 24, no. 7, pp. 1994–2002, July 2007.

[103] I. Velchev, A. Dreischuh, D. Neshev, and S. Dinev, "Interactions of optical vortex solitons superimposed on different background beams," *Opt. Commun.*, vol. 130, pp. 385–392, Oct. 1996.

[104] Y. S. Kivshar, J. Christou, V. Tikhonenko, B. Luther-Davies, and L. M. Pismen, "Dynamics of optical vortex solitons," *Opt. Commun.*, vol. 152, pp. 198–206, June 1998.

[105] F. S. Roux, "Diffractive optical implementation of rotation transform performed by using phase singularities," *Appl. Optics*, vol. 32, no. 20, pp. 3715–3719, July 1993.

[106] A. J. Devaney and G. C. Sherman, "Plane-wave representations for scalar wave fields," *SIAM Rev.*, vol. 15, no. 4, pp. 765–786, Oct. 1973.

[107] I. Freund and M. Wilkinson, "Critical-point screening in random wave fields," *J. Opt. Soc. Am. A*, vol. 15, no. 11, pp. 2892–2902, Nov. 1998.

[108] V. P. Aksenov and A. V. Ustinov, "After-effect of optical vortices and efficiency of an adaptive optical system in the area of its manifestation," in *Free-Space Laser Communications IV*, Proceedings of SPIE, J. C. Ricklin, Ed., vol. 5550, 2004, pp. 374–382.

[109] F. S. Roux, "Branch-point diffractive optics," *J. Opt. Soc. Am. A*, vol. 11, no. 8, pp. 2236–2243, Aug. 1994.

[110] M. R. Dennis, "Topological singularities in wave fields," Ph.D. Thesis, H. H. Wills Physics Laboratory, University of Bristol, 2001.

[111] F. G. Stremler, *Introduction to Communication Systems*, 2nd ed. MA: Addison-Wesley publishing company, 1982.

Appendix A

Continuous and rotational phase slopes separation

In a strongly scintillated beam, there are generally numerous optical vortices in the wavefront. The phase slopes measured by a Shack-Hartmann wavefront sensor can be viewed as a vector field, $\mathbf{G} = G_x\hat{x} + G_y\hat{y}$. Since a Shack-Hartmann wavefront sensor measures the local phase slopes over its subapertures, its measured slopes may contain information about continuous phase parts and solenoidal phase parts. Here, this phase slope vector field can be separated into two vector fields, $\mathbf{C}$ and $\mathbf{S}$, which represent continuous phase slopes and rotational phase slopes respectively. Therefore, it has

$$\mathbf{G} = \mathbf{C} + \mathbf{S}, \tag{A.1}$$

with the curls $\nabla \times \mathbf{C} = 0$ and $\nabla \times \mathbf{S} \neq 0$.

One method to separate the rotational phase slopes and the continuous phase slopes is derived from the concept of branch-point diffractive optics [109]. In this concept, the vortex number density is expressed as

$$D_v = \frac{1}{2\pi}(\nabla \times \nabla\theta(x, y)) \cdot \hat{z}, \tag{A.2}$$

where $\nabla\theta(x, y)$ is the gradient of the phase function on the transverse beam plane and $\hat{z}$ is the propagation direction. This vortex number density will be zero when the phase function is a continuous one. However, it will be nonzero if there are phase singularities in the phase function.

The phase gradient $\boldsymbol{F} = \nabla\theta(x, y)$ created by optical vortices in phase function $\theta(x, y)$ can be calculated directly with a convolution of the vortex number density in Eq. (A.2)

and the basic vortex phase gradient, given by

$$\boldsymbol{F} = D_v \otimes \boldsymbol{F_0}, \tag{A.3}$$

where $\otimes$ denotes a convolution and $\boldsymbol{F_0}$ is the gradient of the phase function of a basic vortex, $x + iy$, located at the origin in Cartesian coordinates, and can be expressed as in Eq. (3.7).

From the outputs of a Shack-Hartmann wavefront sensor, a sampled phase slope vector field $\mathbf{G}$ can be obtained as phase gradient in the sampled filed. Similarly, a sampled map of circulation D can also be computed and viewed as the vortex number density in the sampled field. For a basic vortex located at the origin in Cartesian coordinates, the phase slope vector field $\mathbf{G_0}$ is fixed if the phase slopes are measured by a given Shack-Hartmann wavefront sensor. With Eq. (3.6), the circulations D_0 over all subapertures can be computed from $\mathbf{G_0}$ for such a basic vortex and therefore D_0 is also fixed. Then, the gradient of the phase function of a basic vortex in the sampled field, $\boldsymbol{F_b}$, can be computed by a deconvolution according to Eq. (A.3),

$$\boldsymbol{F_b} = \mathcal{F}^{-1}\left(\frac{\mathcal{F}(\mathbf{G_0})}{\mathcal{F}(D_0)}\right), \tag{A.4}$$

where $\mathcal{F}$ and $\mathcal{F}^{-1}$ are the Fourier transform and its inverse respectively. Here the deconvolution computation in Eq. (A.3) is complemented by Fourier transforms. Since $\mathbf{G_0}$ and D_0 are computed from a basic vortex measured by a given Shack-Hartmann wavefront sensor, $\boldsymbol{F_b}$ is then fixed and can be computed in advance for convenience.

Therefore, according to vortex phase gradient computation in Eq. (A.3), the rotational phase slopes created by vortices in an arbitrary wave field can be separated by a convolution between the Shack-Hartmann circulations D and the sampled basic phase gradient $\boldsymbol{F_b}$, given by

$$\mathbf{S} = D \otimes \boldsymbol{F_b}, \tag{A.5}$$

and the continuous phase slopes can be subtracted,

$$\mathbf{C} = \mathbf{G} - \mathbf{S}. \tag{A.6}$$

With the phase slopes separation method discussed above, the continuous phase slopes $\mathbf{C}$ can be easily separated from the output of a Shack-Hartmann wavefront sensor. Then the continuous phase can be reconstructed from the slopes $\mathbf{C}$. A sampled phase function is shown in Fig. A.1. The phase reconstruction is then implemented on this grid. If $\theta(1,1)$ is set as zero, all other phase values on the grid can be directly reconstructed from the neighboring known phase value and continuous phase slopes because the curl of $\mathbf{C}$ is zero.

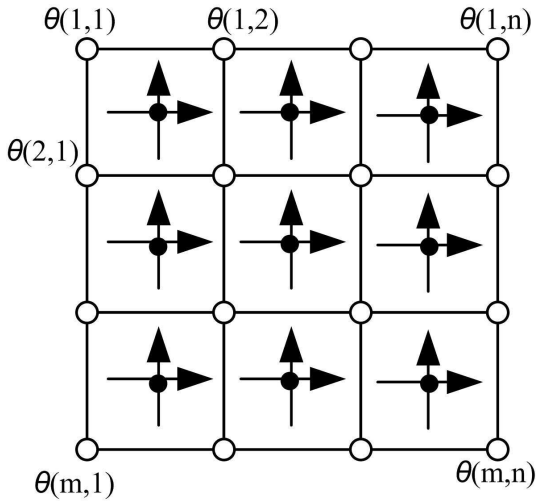

Figure A.1: A sampled phase function in an $m \times n$ array. White circles denote the grids where the phase values, $\theta(i, j)$, are reconstructed. Black dots denote the points where the continuous phase slopes are assigned. Arrows denote the directions of the phase slopes.

According to Eq. (2.21), this reconstructed sampled phase function θ can be sent as the control signals for corresponding actuators of a deformable mirror to form a continuous surface, which in turn corrects the continuous phase fluctuations in the incident wave field. Fig. A.2 shows an example of phase reconstruction from the continuous phase slopes which are separated from a distorted phase function by this method. Fig. A.2(a) shows a distorted phase function, θ, which contains two optical vortices. Fig. A.2(b) shows the independent continuous phase function, θ_c, without these two optical vortices for comparisons. It is difficult to identify the vortices in Fig. A.2(a) because of the phase fluctuations.

The distorted phase function θ is measured by a Shack-Hartmann wavefront sensor numerically. The measured phase slopes is then separated into two parts. One is the continuous phase slopes $\mathbf{C}$ and the other is the rotational phase slopes $\mathbf{S}$, with the separation method discussed above. Fig. A.2(c) shows the continuous phase function, $\theta_c^{'}$, which is formed by a deformable mirror from the sampled continuous phase function reconstructed from the continuous phase slopes $\mathbf{C}$. It can be seen the continuous phase function $\theta_c^{'}$ has a similar shape to the continuous phase function in Fig. A.2(b). After removing this $\theta_c^{'}$ from the original distorted phase function, the rotational phase distributions, which represent the contributions of those two optical vortices, can be obtained, as shown in Fig. A.2(d). It can be seen that two vortices are located at the ends of the branch cut, which is shown as the jump of black and white in Fig. A.2(d). Some phase fluctuations with high frequency still remain in these rotational phase parts. This is because the Shack-Hartmann

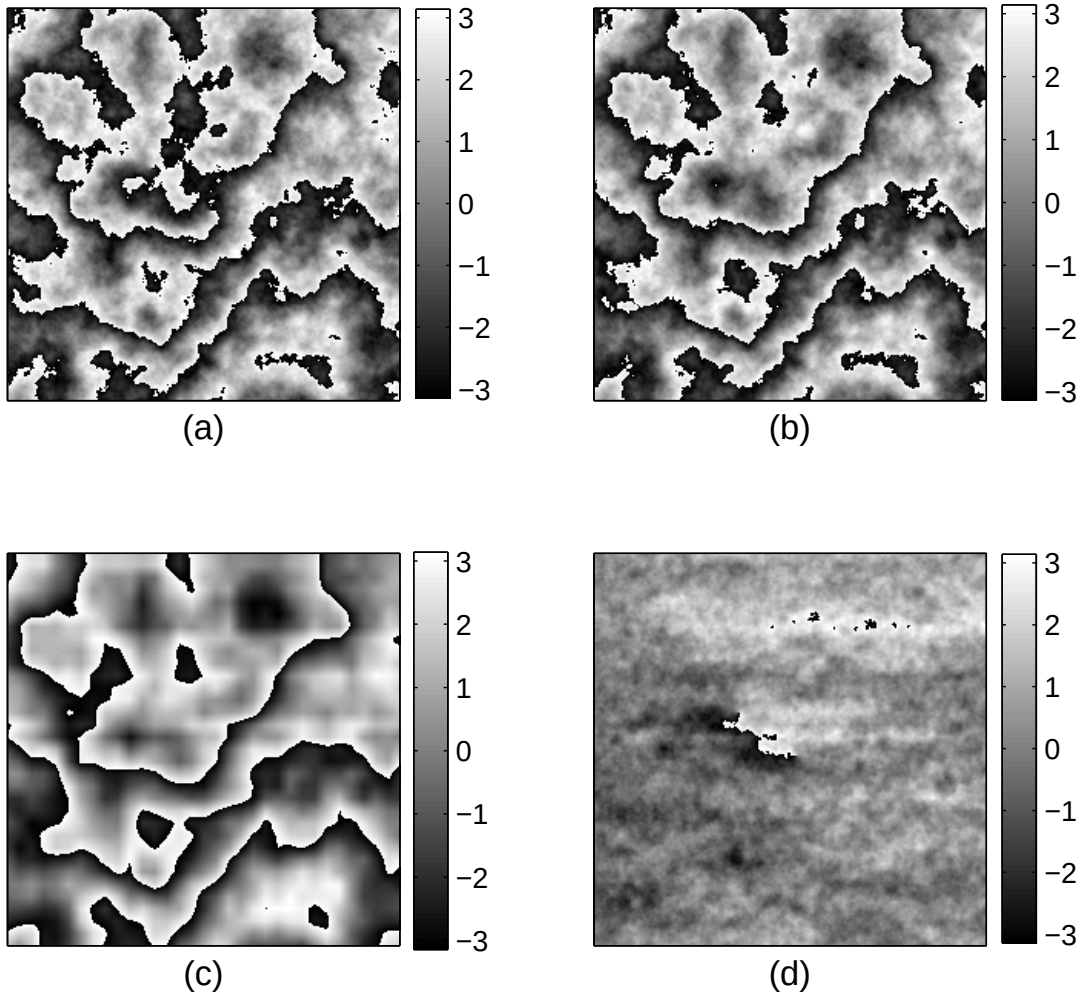

Figure A.2: Continuous phase and rotational phase separation. Figure (a) shows a distorted phase function with two optical vortices inside. Figure (b) shows the independent continuous phase function, θ_c. Figure (c) shows the continuous deformable mirror phase function, θ_c', reconstructed from the continuous phase slopes. Figure (d) shows the rotational phase function, computed as $(\theta - \theta_c')$.

wavefront sensor and the deformable mirror with finite resolutions cannot measure and represent these phase fluctuations with high frequency.

Appendix B

Statistical properties of vortex morphologies

In a random optical field, the anisotropy of an optical vortex can generally be described by the eccentricity of the anisotropy ellipse [42], that is ε ($0 \leq \varepsilon \leq 1$). Its probability density function in two dimensions can be expressed as [110]

$$P(\varepsilon) = \frac{8\varepsilon^3}{(2-\varepsilon^2)^3}. \tag{B.1}$$

This eccentricity parameter of an optical vortex can also be expressed in terms of the anisotropy angle α, given by [110]

$$\varepsilon^2 = \frac{4\tan(\alpha/2)}{(1+\tan\alpha/2)^2}. \tag{B.2}$$

If $0 \leq \alpha < \pi/2$, the polarization is left-handed and the vortex has a positive topological charge. If $\alpha = \pi/2$, the vortex is an edge dislocation. If $\pi/2 < \alpha \leq \pi$, reflection ($\alpha \rightarrow \pi - \alpha$) reverses the handedness and the vortex becomes a negative one, but does not change the form of the anisotropy ellipse. Therefore, the probability density function of α can be calculated with a transformation [111] from ε to α for the positive vortex,

$$\mathrm{P}(\alpha) = \left[\mathrm{P}(\varepsilon)\left|\frac{\mathrm{d}\varepsilon}{\mathrm{d}\alpha}\right|\right]_{\varepsilon=2\sqrt{\tan(\alpha/2)}/(1+\tan(\alpha/2))} = \sin(2\alpha), \qquad 0 \leq \alpha < \pi/2 \tag{B.3}$$

The probability density function for the negative vortex is the same while only changing the sign, written as $\mathrm{P}(\alpha) = -\sin(2\alpha),\ \pi/2 < \alpha \leq \pi$. Therefore, the expectation value of the anisotropy angle α for the positive vortex is

$$\mathrm{E}\{\alpha\} = \int_0^{\pi/2} \alpha P(\alpha)\mathrm{d}\alpha = \frac{\pi}{4}, \tag{B.4}$$

where $\mathrm{E}\{\cdot\}$ denotes the expectation value. Similarly, the expectation value of the anisotropy angle α for the negative vortex is $\mathrm{E}\{\alpha\} = 3\pi/4$.

The probability density function of the anisotropy parameter $b = \cos(\alpha)$ for the positive vortex can be deduced with the same method in Eq. (B.3), given by

$$\mathrm{P}(b) = 2b, \qquad 0 < b \leq 1 \tag{B.5}$$

For the negative vortex, the probability density function will be $\mathrm{P}(b) = -2b, -1 \leq b < 0$.

The expectation value of b for the positive vortex is given by

$$\mathrm{E}\{b\} = \int_0^1 b\mathrm{P}(b)\mathrm{d}b = \frac{2}{3}. \tag{B.6}$$

For the negative vortex, it will be $-2/3$.

In a random wave field, the orientation angle, β, of an optical vortex is uniformly distributed in a range of 0 to 2π [45].

Appendix C

Morphologies of vortex dipole

In this section, the relationship between vortex morphologies and the vortex separation distance prior to dipole annihilation in a Gaussian beam will be discussed. It is assumed that a canonically launched vortex dipole will annihilate after a distance of propagation, as shown in Fig. C.1. Two oppositely charged vortices are separated by a distance of d_0 on the launch plane, t_0, where both of the vortices are canonical ones.

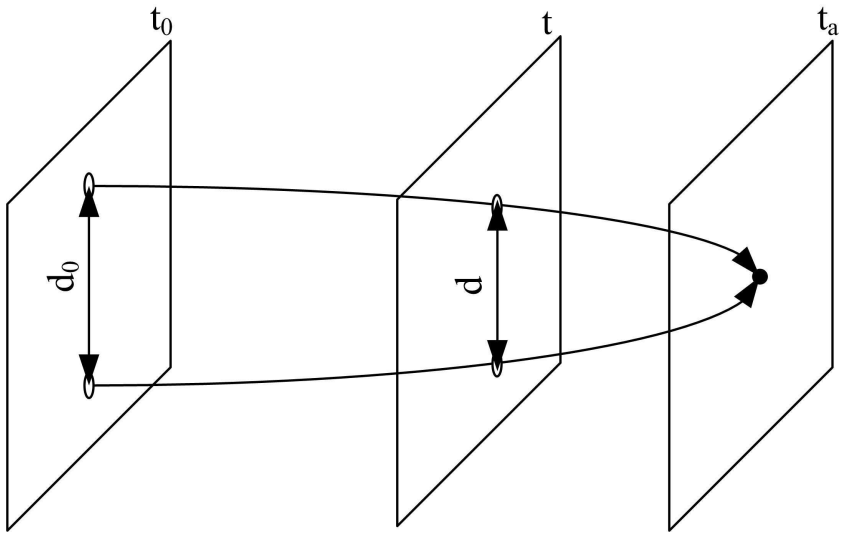

Figure C.1: Diagram of a canonically launched vortex dipole annihilation in a Gaussian beam. Two ellipses denote the two oppositely charged vortices. t_0 denotes the launch plane, on which the vortex separation distance is d_0. These two vortices will annihilate each other on the t_{an} plane.

During beam propagation, vortex separation distance reduces until it becomes zero on the annihilation plane. The morphologies of these two optical vortices also change until they become two edge dislocations and annihilate each other on the annihilation

plane. According to Eqs. (2.38) and (2.39), the vortex morphologies are functions of the propagation distance t. Similarly, vortex separation distance is also a function of the propagation distance t according to Eq. (4.1). This dipole will be created or annihilated at the point where the discriminant $\mathcal{D} = 0$ during beam propagation. To find the relationship between vortex morphologies and vortex separation distance, the propagation distance t needs to be eliminated in Eqs. (4.1), (2.38) and (2.39). According to Eq. (2.34), it cannot be solved for t from $\mathcal{D} = 0$ because it is 4^{th} orders about t. Hence, it is very difficult to express the propagation distance t as a function of the vortex separation distance d. However, the annihilation propagation distance t_a can be numerically calculated from $\mathcal{D} = 0$.

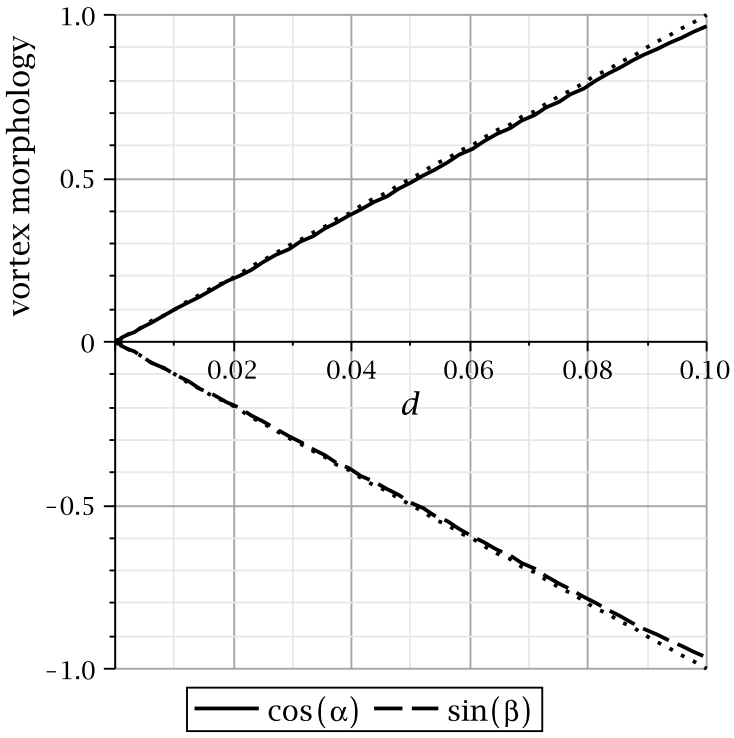

Figure C.2: Vortex morphologies as functions of the vortex separation distance of a dipole in a Gaussian beam with general initial parameters ($u_0 = 0.05, v_0 = 0.25, \Delta u = 0.25, t_0 = 0.5$). The solid and dashed lines respectively denote the anisotropy, $\cos(\alpha)$, and the sine of the relative orientation angle, $\sin(\beta)$, of the positive vortex of the dipole. The dotted lines denote the linear functions as $\pm d/d_0$.

Close to the annihilation plane, a very simple linear relation can be found between the vortex morphology and the vortex separation distance d with a numerical approximation

approach, given by

$$\cos(\alpha) = \pm\frac{d}{d_0}, \tag{C.1}$$

$$\sin(\beta) = \mp\frac{d}{d_0}, \tag{C.2}$$

Where d_0 represents the initial vortex separation distance of this canonically launched vortex dipole; α is the anisotropy angle and β is the relative orientation angle in a vortex dipole. Here, it is noted that this linear approximation is valid only for planes close to the dipole annihilation plane according to the analysis.

Fig. C.2 shows the vortex morphologies for a general case where two canonical vortices are located at $(0.3, 0.25)$ and $(0.2, 0.25)$ in the normalized transverse coordinates in the launch plane ($t_0 = 0.5$). In this figure, the vortex morphologies are approximately proportional to the separation distance d, as expected in Eqs. (C.1) and (C.2), especially when the two vortices are very close to each other. We note that other choices of vortex dipoles with different initial parameters $(u_0, v_0, \Delta u, t_0)$ yield results that are qualitatively similar to this case presented here, provided that the vortices can annihilate each other after some distance of propagation. From the above discussion, it can be understood that in a Gaussian beam the morphology of a canonically launched vortex dipole changes approximately linearly just before these two vortices annihilate each other.

From the morphology evolution of a canonically launched vortex dipole in a Gaussian beam discussed above, it can be assumed that the morphologies of a vortex dipole also change linearly to zero when two oppositely charged vortices approach each other in a random field, although the information about the initial vortex separation distance d_0 cannot be known.

Here, numerical simulations are used to investigate the morphology evolution of the vortex dipoles in scintillated beams. In numerical simulations, only vortex dipoles are taken into consideration. A vortex dipole in a scintillated beam is defined as two oppositely charged vortices with a vortex separation distance smaller than half the distance from any one of these two vortices to the nearest other vortex. Therefore, only these dipoles are taken into consideration while the influences from other vortices are mitigated as well as possible. The vortex morphologies $[\cos(\alpha), \sin(\beta)]$ and the separation distance d are numerically calculated from the distorted phase function for the positive vortex in each dipole. The statistical curves for the morphologies, $\cos(\alpha)$ and $\sin(\beta)$, as functions of d are shown in Fig. C.3.

In Fig. C.3(a), the expectation values of the vortex anisotropy $\cos(\alpha)$ in scintillated

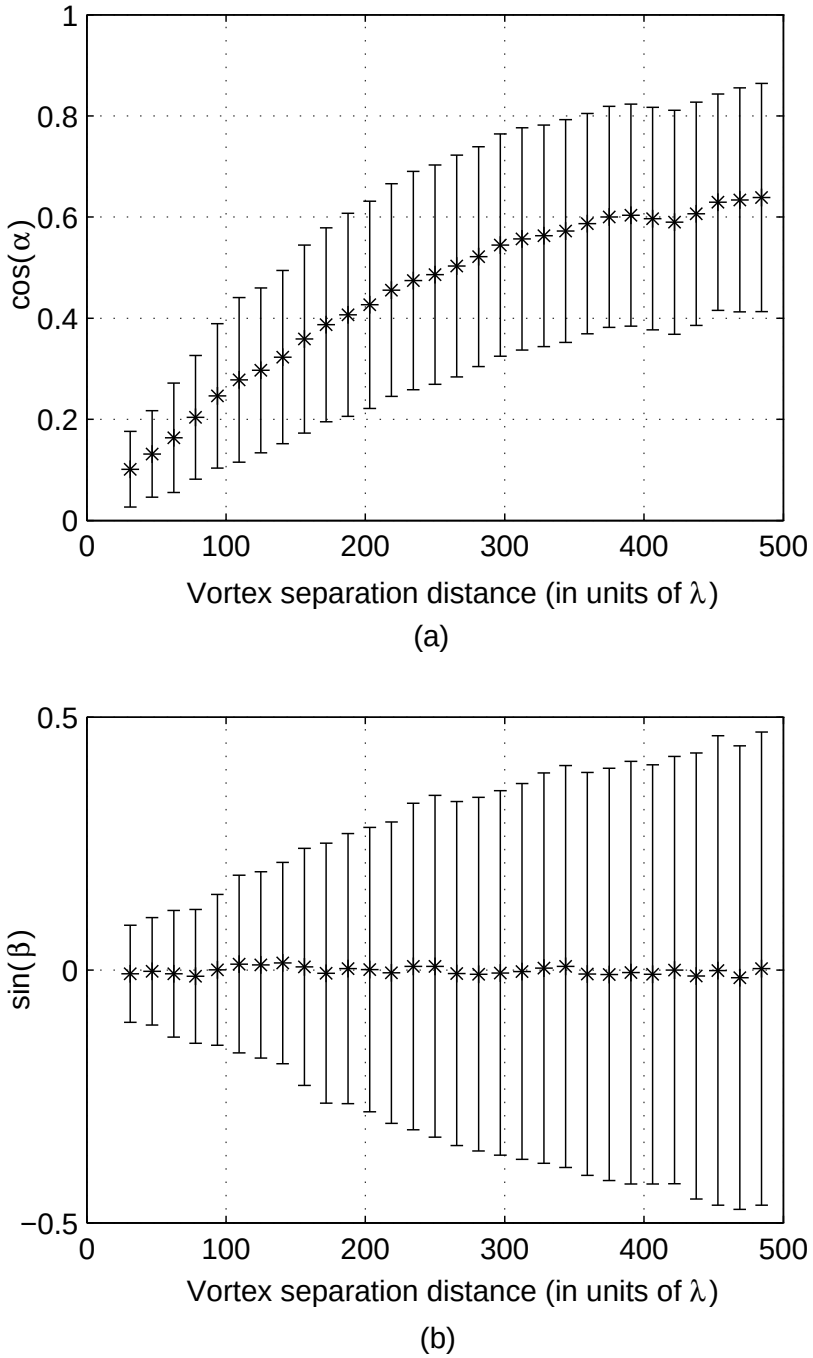

Figure C.3: Vortex morphologies, $\cos(\alpha)$ and $\sin(\beta)$, as functions of the separation distance d in the random wave fields. The stars show the expectation values of vortex morphology and the error bars show the standard deviations.

beams gradually drop to zero when the two vortices in a dipole approach each other. The expectation value of $\cos(\alpha)$ approaches the theoretical expectation value in Eq. (B.6) when the separation distance is larger than 400λ. When the vortex separation distance is relatively large, the vortex anisotropy has weak correlation with other vortices as if it is located in a random fields. Therefore, its anisotropy obeys the theoretical expectation value in random fields. However, the reduction of the separation distance between two oppositely charged vortices cause the anisotropy to have a large correlation in these two vortices before they become two edge dislocations and annihilate each other. As a result, the vortex anisotropy begins to change approximately linearly to zero when these two vortices approach each other, which is similar to the anisotropy of a canonically launched vortex dipole in a Gaussian beam.

As shown in Fig. C.3(b), the expectation value of $\sin(\beta)$ is zero, as the relative orientation angle β can be randomly located between 0 and 2π. Since the vortices in a dipole will become into two edge dislocations in alignment before they annihilate each other, the relative orientation angle β of a vortex will become zero when it is annihilated. In other words, the relative orientation angle of two oppositely charged vortices must be in alignment when they meet each other, which is similar to what happens in the canonical vortex dipole in a Gaussian beam. Hence, its associated standard deviation gradually drops when the vortex separation distance drops to zero.

List of Figures